GUIDED ION BEAM TANDEM MASS SPECTROMETER AND THEORETICAL STUDIES OF THIRD-ROW TRANSITION METAL IONS

Hf^+, Ta^+, W^+, AND Os^+

by

Christopher Hinton

A dissertation submitted to the faculty of
The University of Utah
in partial fulfillment of the requirements for the degree of

Doctor of Philosophy

Department of Chemistry

University of Utah

August 2013

The University of Utah Graduate School

STATEMENT OF DISSERTATION APPROVAL

The dissertation of **Christopher Hinton**

has been approved by the following supervisory committee members:

Peter B. Armentrout	, Chair	**3/1/2012** Date Approved
Scott L. Anderson	, Member	**3/1/2012** Date Approved
Michael D. Morse	, Member	**3/1/2012** Date Approved
Joel S. Miller	, Member	**3/1/2012** Date Approved
James Sutherland	, Member	**3/1/2012** Date Approved

and by **Henry S. White**, Chair of the Department of **Chemistry**

and by Donna M. White, Interim Dean of The Graduate School.

ABSTRACT

Guided ion beam mass spectrometry is used to study the kinetic energy dependence of the reactions of the third-row transition metal ions of hafnium, tantalum, tungsten, and osmium. For Hf^+ and Os^+, the reaction with H_2 and its isotopic analogue, D_2, are performed. The corresponding state-specific reaction cross sections are analyzed for endothermic formation of MH^+ and MD^+ to give 0 K bond dissociation energies (in eV) of $D_0(Hf^+\text{-}H) = 2.11 \pm 0.08$ and $D_0(Os^+\text{-}H) = 2.45 \pm 0.10$. Results from the reaction of the metal ions with HD provide insight into the reaction mechanism and indicate that Hf^+ reacts according to a statistical mechanism while Os^+ via a direct reaction. These results are also compared to their first-row and second-row congeners. Theoretical calculations are performed to compare calculated bond energies with experimental bond energies as well as provide electronic structures of species and potential energy surfaces for reaction.

For the ions Hf^+, Ta^+, and W^+, reactions with CO and O_2 are performed. Reactions with O_2 are exothermic and provide an upper bound for the M^+-O BDE, while the endothermic cross sections measured for CO provide 0 K bond energies (in eV) of $D_0(Hf^+\text{-}C) = 3.19 \pm 0.03$, $D_0(Ta^+\text{-}C) = 3.79 \pm 0.04$, $D_0(W^+\text{-}C) = 4.76 \pm 0.09$, $D_0(Hf^+\text{-}O) = 6.91 \pm 0.11$, $D_0(Ta^+\text{-}O) = 7.10 \pm 0.12$, and $D_0(W^+\text{-}O) = 6.77 \pm 0.07$. Additionally, collision-induced dissociation studies are done for the metal oxides and dioxides of Ta^+ and W^+ and provide 0 K threshold energies (in eV) of $E_0(Ta^+\text{-}O) = 7.01 \pm 0.12$, $E_0(W^+\text{-}O)$

= 6.72 ± 0.10, $E_0(OTa^+-O)$ = 6.08 ± 0.12, and $E_0(OW^+-O)$ = 5.49 ± 0.09, which in these cases can also be equated with the 0 K bond energies. Additionally, theoretical calculations are performed to discuss the nature of bonding in the MC^+, MO^+, and MO_2^+ species. Calculated BDEs are compared to experimental results and electronic structures of species as well as potential energy surfaces for reaction are provided.

TABLE OF CONTENTS

LIST OF TABLES

LIST OF FIGURES

ACKNOWLEDGEMENTS

First and foremost, I would like to thank my advisor, Dr. Peter B. Armentrout, for his guidance and assistance during the course of this work. The experiences in Peter's laboratory have been both challenging and rewarding.

Past and present members of the Armentrout group are thanked for fruitful discussions and for making the laboratory a fun and friendly working environment. I would like to especially thank Dr. Feng-Xia Li and Dr. Murat Citir for their help in taking the data presented here.

I would also like to thank the talented personnel in the department's electronic and machine shops. The machining skills of Dennis Romney and the electronics expertise of Dale Heisler are especially noted.

The National Science Foundation provided funding for this work.

CHAPTER 1

INTRODUCTION AND OVERVIEW

1.1 Introduction

There are numerous studies of the reactions of atomic first-row, second-row, and third-row transition metal ions with the small molecules such as H_2, CO, and O_2. Such studies provide insight into the activation of covalent bonds by single metal centers and the periodic trends in the reactivity of metals. The thermochemistry obtained from these studies is of obvious fundamental interest and has implications in understanding a variety of catalytic reactions involving transition metal systems.[1,2] In these processes, transition metal complexes are formed as intermediates in catalytic transformations. A better understanding of these intermediates could help to design more efficient catalysts. However, little information for these intermediates is available because the extreme reactivities of these intermediates makes it difficult to isolate these species.

The reactions of bare transition metal ions with small molecules in the gas phase are a good starting point for providing information on the intrinsic properties of metals in the absence of solvent and stabilizing ligands. These studies also form an ideal interface with theoretical calculations and provide benchmark information to guide theory of more complex systems. Studies in the gas phase are useful in providing information on the intrinsic properties of bare metal atoms in the absence of solvent and stabilizing ligands or metal support and surface effects. Numerous studies of the reactions of atomic or

metal support and surface effects. Numerous studies of the reactions of atomic transition metal ions with hydrogen and other small molecules in the gas phase have been described previously.[3,4]

In this work, we have chosen to study the chemistry of the third-row transition metal ions of Hf^+, Ta^+, W^+, and Os^+ with $H_2/D_2/HD$, CO, and O_2 as well as the collision induced dissociation (CID) reaction of TaO^+, WO^+, TaO_2^+, and WO_2^+ with Xe. The ground states of these third-row transition metal ions have valence electron configurations of $6s^25d$, $6s5d^3$, $6s5d^4$, and $6s5d^6$, respectively.[5] These studies will help to understand the difference of bond energies, reactivity of transition-metal complexes, and reaction mechanisms, thereby establishing periodic trends of the third-row transition metals. In addition, these heavy transition metal containing systems are good examples to study the influence of strong spin-orbit coupling on the reactivity. Theoretical calculations will provide electronic structures of products and reactants, explore potential energy surfaces and possible mechanisms along these reaction surfaces.

Part of an ongoing systematic study in our lab is the activation of covalent bonds by transition metal cations using guided ion beam mass spectrometry. Currently, there are numerous studies of first,[6-17] second,[11,16,18-20] and third-row transition metal ions[21-25] reacting with dihydrogen and its isotopic analogues. Here, these studies are extended to hafnium and osmium. σ-bond activation by atomic metal ions can be understood using a simple donor-acceptor model. When an H_2 molecule approaches a transition metal ion, M^+, in a perpendicular direction (C_{2v} symmetry), the most efficient reaction occurs when M^+ accepts electrons from the σ (H_2) bonding orbital into an empty ns or (n-1)dσ orbital and donates a pair of (n-1)dπ electrons into the $\sigma^*(H_2)$ antibonding orbital. These

interactions effectively weaken and lengthen the H_2 bond while simultaneously building electron density between the metal and H atoms. If the valence ns or (n-1)dσ orbitals are occupied, then there is a more repulsive interaction between M^+ and H_2 that can be reduced if the H_2 approaches M^+ in a collinear geometry ($C_{\infty v}$ symmetry).

There are two main factors that influence the reactivity of the metal ion-dihydrogen reaction system. One is the reaction thermochemistry, and the other is the electron configuration of M^+ and its spin state. For the reaction thermochemistry, it has been found that the third-row metals generally have stronger BDEs with hydrogen than their first-row and second-row congeners, which has been described by Ohanessian *et al.* as largely a consequence of the lanthanide contraction and relativistic effects that allow efficient 6s-5dσ hybridization.[26] To understand the differences that the electron configuration of M^+ and its spin state can impose, we need to consider the reaction mechanisms revealed by studies with HD. Previous work on the first-row and second-row transition metal cations indicates that the product branching ratio in the reaction of M^+ with HD is very sensitive to the reaction mechanism.[19,20,27-29] and is governed by three "rules". (1) If M^+ has an electron configuration with empty valence *s* and *dσ* orbitals, such as for a d^n configuration where $n < 5$, the reaction is efficient and may proceed by an insertion mechanism. These processes are characterized by product branching ratios in the HD system, ($\sigma_{MH}+ / \sigma_{Total}$) values that are near 0.5, consistent with statistical behavior of a long-lived intermediate. (2) If either the valence s or dσ orbital is occupied and the M^+ state is low-spin, such as for d^n ($n > 5$) or low-spin coupled $d^{n-1}s^1$ configurations, the reaction occurs efficiently via a direct mechanism. These processes are characterized by a product branching ratio in the HD system that favors MH^+ by a

factor of 2 – 4, ($\sigma_{MH}^+ / \sigma_{Total}$) ratios between 0.66 and 0.8, consistent with arguments concerning the conservation of angular momentum.[30-34] (3) If either the valence s or dσ orbital is occupied and the M^+ state is high-spin (the highest spin it can possibly have), such as a high-spin coupled $d^{n-1}s^1$ configuration, the reaction is inefficient and tends to react impulsively. These processes are characterized by a product branching ratio in the HD system that favors $MD^+ + H$ by a large factor, small values of the ($\sigma_{MH}^+ / \sigma_{Total}$) ratio, and exhibit shifts in the thresholds for the H_2 and D_2 systems versus the HD system.

For HfH^+, the BDE has been measured in our lab in the reaction of Hf^+ with CH_4 as 1.97 ± 0.11 eV.[35] The other two group 4 metal ions, Ti^+ and Zr^+, have MH^+ BDEs of 2.31 ± 0.11 and 2.26 ± 0.08, slightly above that of HfH^+.[19,20] This lower MH^+ BDE for Hf^+ can be rationalized by its unusual ground state configuration, $^2D(6s^25d^1)$, that should lead to repulsive reaction with H_2 (see above). Therefore, Hf^+ needs to promote to an excited state in order to effectively react with H_2 because of its full 6s shell (see Chapter 3). For Os^+, there are no previous experimental values of its BDE, but it has been calculated to be 2.45 eV by Ohanessian *et al.* using GVB methods. This value when compared to the other two group 8 metal ions, Fe^+ and Ru^+, having MH^+ BDEs that are 2.12 ± 0.06 and 1.62 ± 0.05 eV,[19,36] respectively, would put Os^+ more in line with other third-row metal having stronger bonds than their first-row and second-row congeners by using sd hybridized orbitals (see Chapter 4).

Previous experiments in our laboratory have also included the reactions of first,[37,38] second,[39-41] and third-row[42,43] transition metals with oxygen. We extend these studies to the third-row transition metals hafnium, tantalum, and tungsten. Previously, Bohme has

looked at the reaction of these three metal ions with O_2 and found that they react exothermically to form the MO^+ species. These results imply that $D_0(M^+\text{-}O) > D_0(O_2) =$ 5.115 eV.**Error! Bookmark not defined.**

We also looked at the reaction of these metal ion with carbon monoxide in order to give more accurate thermochemistry of the metal oxides as well as the metal carbides, for which information in the literature is scarce. Schröder *et al.*[44] have previously reported the BDEs (in eV) for the metal oxide as $D_0(Hf^+\text{-}O) = 7.30 \pm 0.22$, $D_0(Ta^+\text{-}O) = 8.15 \pm 0.65$, and $D_0(W^+\text{-}O) = 5.46 \pm 0.43$ citing the GIANT (Gas-phase Ion and Neutral Thermochemistry) compilation (see Chapter 5).[45] The bonding in these metal oxides systems are interesting as the metal ions in these systems each have an empty d orbital that can accept the lone pair of electrons from the ^3P state of O to form a triple bond. This type of bonding can explain the stronger bonds of early group MO^+ species compared to latter group MO^+ species.

For the metal carbides, information is more scarce. No previous literature values exist for the BDE of HfC^+. TaC^+ has been studied theoretically by Majumdar and Balasubramanian with a BDE calculated to be 4.50 eV.[46] Cassady and McElvany measured the TaC^+ BDE in the reaction of TaC^+ with CH_4 with an estimated BDE of 3.38 – 6.11 eV.[47,48] In our lab, the reaction of W^+ with CH_4 has produced a WC^+ BDE of 4.96 ± 0.22 eV.[49] The weaker BDEs of the carbides in comparison to the oxides can be attributed to the carbon atom (also having a ^3P state) not having a lone pair of p electrons to donate to the metal ion, while oxygen does.

For the study of gas phase ion molecule reactions, guided ion beam tandem mass spectrometry (GIBMS) is a powerful tool to study both exothermic and endothermic

reactions under single collision conditions. This instrument is described in detail in Chapter 2. This technique provides the kinetic energy dependence of gas phase ion-molecule reactions. The energy of these reactions can be varied from thermal energies up to 1000 eV. Other techniques, such as ion cyclotron resonance (ICR) mass spectrometry,[50] have limited abilities to access high energy regimes and are restricted primarily to the study of exothermic processes and the measurement of ion-molecule equilibria at thermal energies. The ability of GIBMS to access a wide range of interaction energies allows for highly endothermic processes to be studied.

Typically, the kinetic-energy dependence of a chemical reaction is presented as a product cross section, which is a measure of the reaction probability as a function of the reaction energy. The minimum energy required to form a product is referred to as the product threshold. The threshold is the most important thermodynamic quantity from a GIBMS product cross section and is used to calculate bond energies of the products. Previous studies in our laboratory have established the thermochemistry of a vast array of ion-molecule systems using this technique.[51]

1.2 Overview

Chapter 2 gives a detailed description of the guided ion beam tandem mass spectrometer as well as the ion source. The endothermic cross sections are modeled by an empirical model that is discussed in detail. A detailed description of the theoretical calculations is given, which includes the level of theory, basis set, and effective core potentials (ECPs) used.

Chapters 3 and 4 discuss the reactions of Hf^+ and Os^+ with H_2, D_2, and HD. These experiments provide bond dissociation energies (BDE) for the metal hydride systems and

provide insight into the reaction mechanism. Theoretical calculations are also performed to assign electronic structures of the reactants and products and to explore potential energy surfaces and possible mechanisms of the reaction surface.

Chapter 5 discusses the reaction of Hf^+, Ta^+, and W^+ with CO and O_2. The reactions with O_2 are exothermic and provide a lower limit for the metal oxide BDE's. The reactions with CO provide BDEs for the metal oxide and metal carbide ions. Theoretical calculations are also performed to assign electronic structures of reactants and products and to explore potential energy surfaces and possible mechanisms of the reaction surface.

Chapter 6 discusses the collision-induced dissociation (CID) of TaO^+, WO^+, TaO_2^+, and WO_2^+ with Xe. Also, the reaction of TaO^+ and WO^+ with O_2 is discussed. These studies provide BDEs of the metal oxide and dioxides. Theoretical calculations are also performed to assign electronic structures of the reactants and products and to explore potential energy surfaces and possible mechanisms of the reaction surface.

1.3 Future Work

An area of future work to extend the work in this thesis is the study of the reactivity of the different electronic states of the transition-metal ions. Ionization of transition-metals can produce a relatively large amount of low-lying electronic states. The work in this thesis was limited to the study of the ground state as any excited states were quenched with a cooling gas in order to simplify analysis of product cross sections. The study of these different excited state configurations can be done using ion mobility. Pioneering work by Kemper and Bowers on first-row transition-metal atomic ions showed that different configurations of atomic ions drift through a cell containing He at different rates.[52] They coined the term "electronic-state chromatography" to describe a

time-dependent spectrum in which the various peaks correspond to different electronic configurations.

The results of the different mobilities for the metal ions arises from whether the electron configuration is d^n or sd^{n-1}. These configurations have different potential-energy surfaces arising from their reaction with He such that states with d^n configuration migrate more slowly through He than sd^{n-1} states, a result of the repulsive interaction between ions with occupied s orbitals and the closed shell He gas. The sd^{n-1} configuration will have weaker interactions with the He gas and will be impeded less as they migrate through the drift cell. In earlier state-specific studies in the Armentrout group, ground state $Fe^+(^6D, 4s3d^6)$ was found to be less reactive towards H_2, CH_4, and C_2H_6 than excited state $Fe^+(^4F, 3d^7)$.[53,54] For studies on the four metal ions presented in this thesis, $Hf^+(^2D,6s5d^2)$, $Ta^+(^5F, 6s5d^3)$, $W^+(^6D, 6s5d^4)$, $Os^+(^6D, 6s5d^6)$, the results for ion mobility studies could be more complex. Recently, in the Armentrout group, an ion mobility source has been developed to study state-specific reactions for different electronic states of atomic metal ions, with results for the group 6 transition metals showing efficient configuration separation. For the group 6 ions, Cr^+, Mo^+, and W^+, Iceman *et al.*[55] measured mobilities for the d^5 and s^1d^4 configuration with the d^5 configuration mobility lower in all cases. For W^+, the d^5 configuration mobility is higher than for either Cr^+ and Mo^+ along with the difference in mobilities for the d^5 and s^1d^4 configuration of W^+ being smaller than its first and second row congeners. This result implies that the larger d^n configuration for third-row cations may not interact as strongly with He as is the case for first and second-row transition metals with a d^5 configuration. Additionally, Hf^+ with a $6s^25d^1$ configuration was found to have the lowest mobility among the third-row

transition metals even though having a full 6s shell suggests it should be less attractive than s^1d^{n-1} or d^5 configurations.[56] These results imply that mobility measurements for third-row transition metal may be more ambiguous with the mobilities for different electronic configurations being not as clearly defined as they are for the first and second-row.

Additionally, there are other systems for which reactions of these metal ions would be of interest. For Os^+, reaction with CO could be done (data for reaction with O_2 has been taken but is yet unpublished) in order to get BDE data for OsO^+ and OsC^+. The BDE for OsO^+ could then be directly compared between the reactions with O_2 and CO. For all metals studied here, reaction with CH_4 has been done[57-59] and so extension to longer chain hydrocarbons such as ethane or propane would be of interest in order to probe how these transition metal ions insert and cleave C-C bonds. Also to compliment the CID reactions of the metal oxides and dioxides of tantalum and tungsten done here, CID reactions for the metal oxides and dioxides for hafnium and osmium would be of interest to see how their CID thresholds compare to the bond energies measured in the reactions with O_2 and CO.

1.4 References

[1] R. H. Crabtree, *The Organometallic Chemistry of the Transition Metals*, 2nd ed. (Wiley, New York, 1994).

[2] G. A. Somarjai, *Introduction to Surface Chemistry and Catalysis* (Wiley, New York, 1994).

[3] J. Allison, Prog. Inorg. Chem. **34**, 627 (1986). R.R. Squires, Chem. Rev. **87**, 623 (1987). *Gas- Phase Inorganic Chemistry*, edited by D.H. Russell (Plenum, New York, 1989). K. Eller and H. Schwarz, Chem. Rev. **91**, 1121 (1991).

[4] For reviews, see: (a) P. B. Armentrout and B. L. Kickel, *In Organometallic Ion Chemistry*, edited by B. S. Freiser (Kluwer, Dordrecht, 1996), p. 1. (b) P. B. Armentrout, In *Organometallic Bonding and Reactivity*, edited by J. M. Brown and P. Hofmann, *Topics in Organometallic Chemistry*; Vol 4-I (Springer-Verlag, Berlin, 1999) p. 1.

[5] C. E. Moore, *Atomic Energy Levels,* NSRDS-NBS, 1971, 35/Vol. III.

[6] P. B. Armentrout and J. L. Beauchamp, Chem. Phys. **50**, 37 (1980).

[7] P. B. Armentrout and J. L. Beauchamp, J. Am. Chem. Soc. **103**, 784 (1981).

[8] P. B. Armentrout, L. F. Halle, and J. L. Beauchamp, J. Am. Chem. Soc. **103**, 962 (1981).

[9] P. B. Armentrout, L. F. Halle, and J. L. Beauchamp, J. Am. Chem. Soc. **103**, 6501 (1981).

[10] L. F. Halle, F. S. Klein, and J. L. Beauchamp, J. Am. Chem. Soc. **106**, 2543 (1984).

[11] M. L. Mandich, L. F. Halle, and J. L. Beauchamp, J. Am. Chem. Soc. **106**, 4403 (1984).

[12] M. A. Tolbert and J. L. Beauchamp, J. Am. Chem. Soc. **106**, 8117 (1984).

[13] J. L. Elkind and P. B. Armentrout, J. Chem. Phys. **84**, 4862 (1986).

[14] J. L. Elkind and P. B. Armentrout, J. Phys. Chem. **90**, 6576 (1986).

[15] J. L. Elkind and P. B. Armentrout, Inorg. Chem. **25**, 1078 (1986).

[16] J. L. Elkind and P. B. Armentrout, J. Phys. Chem. **91**, 2037 (1987).

[17] J. L. Elkind and P.B. Armentrout, Int. J. Mass Spectrom. Ion Processes, **83**, 259 (1988).

[18] J. L. Elkind, L. S. Sunderlin, and P. B. Armentrout, J. Phys. Chem. **93**, 3151 (1989).

[19] Y.-M. Chen, J. L. Elkind, and P. B. Armentrout, J. Phys. Chem. **99**, 10438 (1995).

[20] M. R. Sievers, Y.-M. Chen, J. L. Elkind, and P. B. Armentrout, J. Phys. Chem. **100**, 54 (1996).

[21] X.-G. Zhang, C. Rue, S.-Y. Shin, and P. B. Armentrout, J. Chem. Phys. **116**, 5574, (2002).

[22] X.-G. Zhang and P. B. Armentrout, J. Chem. Phys. **116**, 5565 (2002).

[23] P. B. Armentrout and F.–X. Li, J. Chem. Phys. **121**, 248 (2004).

[24] F.–X. Li, X.–G. Zhang, and P. B. Armentrout, J. Phys. Chem. B **109**, 8350 (2005).

[25] F.–X. Li, C. S. Hinton, M. Citir, F. Lui, and P. B. Armentrout, J. Chem. Phys. **109**, 024310 (2011).

[26] G. Ohanessian, M. J. Brusich, and W. A. Goddard III, J. Am. Chem. Soc. **112**, 7179 (1990).

[27] P. B. Armentrout , ACS Symp. Ser. **428**, 18 (1990).

[28] P. B. Armentrout Int. Rev. Phys. Chem. **9**, 115 (1990).

[29] P. B. Armentrout, in *Advances in Gas Phase Metal Ion Chemistry*, edited by N. G. Adams and L. M. Babcock (JAI, Greenwich, 1992), Vol. 1, p. 83.

[30] N. Aristov and P. B. Armentrout, J. Am. Chem. Soc. **108**, 1806 (1986).

[31] J. L. Elkind and P. B. Armentrout, J. Phys. Chem. **89**, 5626 (1985).

[32] L. S. Sunderlin, N. Aristov, and P. B. Armentrout, J. Am. Chem. Soc. **109**, 78 (1987).

[33] J. D. Burley, K. M. Ervin, and P. B. Armentrout, Int J. Mass Spectrom. Ion Processes **80**, 153 (1987).

[34] P. B. Armentrout, ACS Symp. Ser. **502**, 194 (1992).

[35] L. G. Parke, C. S. Hinton, and P. B. Armentrout, Int. J. Mass Spectrom. **254**, 168 (2006).

[36] Y. –M. Chen, J. L. Elkind, and P. B. Armentrout, *J. Phys. Chem.* **99**, 10438 (1995).

[37] S. K. Loh, E. R. Fisher, L. Lian, R. H. Schultz, and P. B. Armentrout, J. Phys. Chem. **93**, 3159 (1989).

[38] E. R. Fisher, J. L. Elkind, D. E. Clemmer, R. Georgiadis, S. K. Loh, N. Aristov, L. S. Sunderlin, and P. B. Armentrout, J. Chem. Phys. **93**, 2676 (1990).

[39] S. K. Loh, L. Lian, and P. B. Armentrout, J. Chem. Phys. **91**, 6148 (1989).

[40] Y.–M. Chen and P. B. Armentrout, J. Chem. Phys. **103**, 618 (1995).

[41] M. R. Sievers, Y.–M. Chen, and P. B. Armentrout, J. Chem. Phys. **105**, 6322 (1996).

[42] X.–G. Zhang and P. B. Armentrout, J. Phys. Chem. A. **107**, 8904 (2003).

[43] F.–X. Li, K. Gorham, and P. B. Armentrout, J. Phys. Chem. A **114**, 11043 (2010).

[44] M.W. Chase, C.A. Davies, J. R. Downey, D.J. Frurip, R.A. McDonald, A.N. Syverud, JANAF Thermodynamic Tables. J. Phys. Chem. Ref. Data **14** (Suppl. 1) (1985) 1.

[45] D. Schröder, H. Schwarz, and S. Shaik, Structure and Bonding **97**, 91 (2000).

[46] S.G. Lias, J.E. Bartmess, J.F. Liebman, J.L. Holmes, R.D. Levin, and W.G. Mallard, J. Phys. Chem. Ref. Data Suppl. 1 **17**, 1 (1988).

[47] D. Majumdar and K. Balasubramanian, Chem. Phys. Lett. **294**, 273 (1998).

[48] C. J. Cassady and S. W. McElvany, J. Phys. Chem. **94**, 2057 (1990).

[49] C. J. Cassady and S. W. McElvany, J. Am. Chem. Soc. **112**, 4188 (1990).

[50] P. B. Armentrout, S. Shin, and R. Liyanage, J. Phys. Chem A **110**, 1242 (2006).

[51] D. H. Russel, J. V. B. Oriedo, and T. Solouki, *In Organometallic Ion Chemistry*, edited by B.S. Freiser (Kluwer, Dordrecht, 1996), p. 197.

[52] See reference 4a.

[53] P. R. Kemper and M. T. Bowers, J. Phys. Chem **95**, 5134 (1991).

[54] J. L. Elkind, and P. B. Armentrout, J. Am. Chem. Soc. **108**, 2765 (1986).

[55] R. H. Schultz, J. L. Elkind, and P. B. Armentrout, J. Am. Chem. Soc. **110**, 411 (1988).

[56] C. Iceman, C. Rue, R. M. Moision, B. K. Chatterjee, and P. B. Armentrout, J. Am. Soc. Mass Spectrom. **18**, 1196 (2007).

[57] W. S. Taylor, E. M. Spicer, and D. M. Barnas, J. Phys. Chem. A **103**, 643 (1999).

[58] L. G. Parke, C. S. Hinton, and P. B. Armentrout, Int. J. Mass Spectrom. **254**, 168 (2006).

[59] L. G. Parke, C. S. Hinton, and P. B. Armentrout, J. Phys. Chem. C **111**, 17773 (2007).

[60] P. B. Armentrout, S. Shin, and R. Liyanage, J. Phys. Chem. A **110**, 1242 (2006).

CHAPTER 2

EXPERIMENTAL METHODS, DATA ANALYSIS, AND THEORETICAL METHODS

2.1 GIBMS

The guided ion beam tandem mass spectrometer on which these experiments were performed has been described in detail previously.[1,2] Figure 2.1 gives a schematic of the instrument with a flow-tube ion source. Briefly, reactant ions are generated in a direct current discharge flow tube source described below. The ions are extracted from the source, accelerated, and focused into a magnetic sector momentum analyzer for mass selection of the primary reactant ions. Mass-selected ions are decelerated to a desired kinetic energy and focused into an octopole ion beam guide, which uses radio-frequency electric fields to trap the ions in the radial direction and ensure complete collection of reactant and product ions.[3,4] The octopole passes through a static gas cell that contains the reaction partner at a low pressure (usually ≤ 0.4 mTorr) so that multiple ion-molecule collisions are improbable. All products reported here result from single bimolecular encounters, as verified by pressure dependence studies. Product and unreacted primary ions drift to the end of the octopole where they are extracted, focused, and passed through a quadrupole mass filter for mass analysis, and subsequently detected with a secondary electron scintillation ion detector using standard pulse counting techniques.

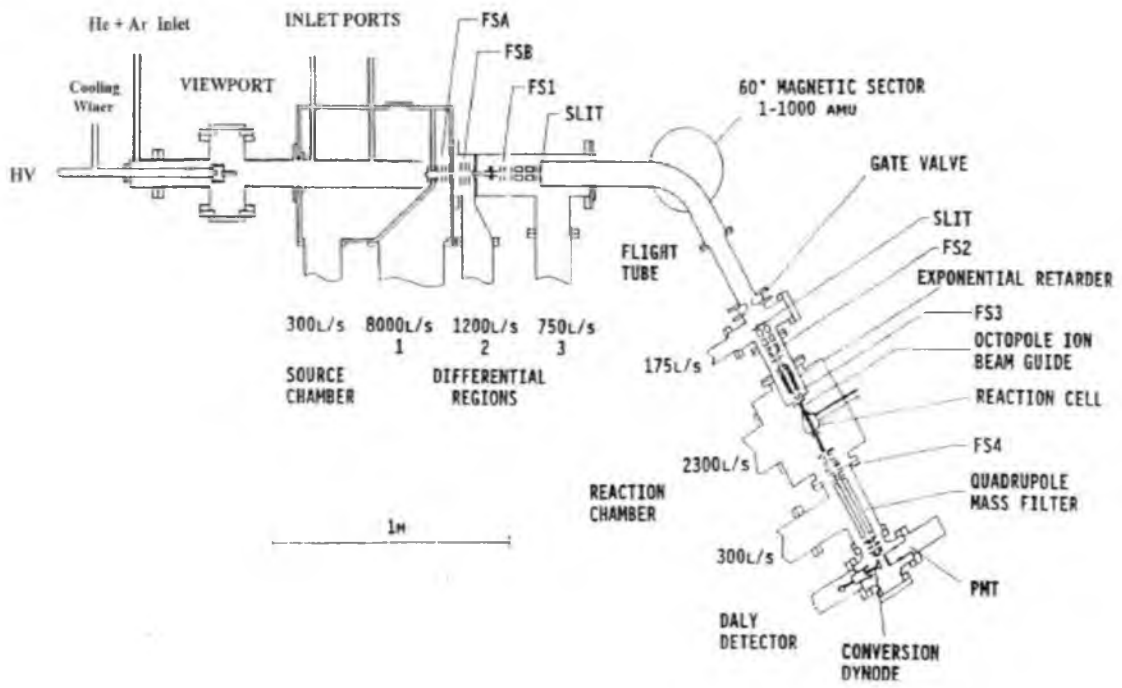

Figure 2.1 Schematic of the guided-ion-beam mass spectrometer designed to measure the energy dependences of reactions of thermalized, continuous beams of metal ions. The pumping speeds are given for the individual diffusion pumps, except for the source chamber, which is pumped by a roots blower.

The distribution of the ion kinetic energy and the absolute zero of energy are determined using the octopole beam guide as a retarding potential analyzer.[5] By taking the derivative of the transmission curve, the distribution of ion kinetic energies is shown to be nearly Gaussian with a typical full-width at half maximum (FWHM) between 0.5 – 1.7 eV (lab) in these studies. The uncertainties in the absolute energy scale are ± 0.05 eV (lab). The kinetic-energy dependence of the ions is varied during an experiment by scanning the dc bias on the octopole with respect to the potential of the ion source region. The quadrupole is also scanned over all the products and unreacted parent ions and the intensities are recorded at each energy. Both the octopole bias and quadrupole are computer controlled. This process is repeated multiple times to allow signal averaging, thus making it possible to study relatively inefficient chemical reactions. Two effects broaden the cross section data: the thermal motion of the neutral reactant gas (Doppler broadening)[6] and the kinetic energy distribution of the reactant ion.

2.2 Ion Source

The metal ions in these experiments are formed in a direct current discharge flow tube (DC/FT) source.[2] This source consists of a cathode held at a high negative voltage (0.7 – 1.5 kV) over which a flow of approximately 90% He and 10% Ar passes at a total pressure of 0.3 – 0.5 Torr and ambient temperature. Ar^+ ions created in the discharge are accelerated towards the metal cathode, thereby sputtering M^+ ions. These ions are then swept down a 1 m long flow tube. The flow conditions used in this ion source provide about 10^5 thermalizing collisions between an ion and He (~10^4 collisions with Ar) before the ions enter the guided ion beam apparatus. However, because there may still exist some excited states of M^+ in the flow tube, a cooling gas can be added to the flow tube to

quench those excited states. The ideal cooling gas can react efficiently with all of the excited states of M^+ but not with the ground state of M^+, such that a nearly pure ground state M^+ beam is left to react with the reactant gas.

MO^+ ions are produced by the introduction of N_2O into the flow tube about 15 cm downstream of the discharge zone. Three-body collisions with the He/Ar flow gas stabilize and thermalize the ions both rotationally and vibrationally. These ions are presumed to be in the ground electronic state and the internal energy of these complexes should be well described by a Maxwell-Boltzman distribution of rotational and vibrational states corresponding to 300 ± 100 K. These assumptions of efficient thermalization are usually valid for molecular species, as shown by previous work.[7-9]

2.3 Trapping Efficiency of the Octopole

The effective trapping potential of multipole rf devices is described by equation 2.1,

$$U_{\text{eff}} = [n^2q^2V_0^2 / 4m\omega^2r_0^2][r / r_0]^{2n-2} \qquad (2.1)$$

where U_{eff} is the effective trapping potential, $2n$ is the number of poles (rods), q is the ion charge, m is the ion mass, r is the radial position with respect to the axis of the device, r_0 is the inscribed radius of the multipole, and $\pm V_0\cos\omega t$ describes the rf potential applied to the rods. The final term in brackets in equation 2.1 indicates that the trapping potential of an octopole ($n = 4$) is proportional to r^6, while that of a quadrupole ($n = 2$) is proportional to r^2. The differences in the potential profiles are shown in Figure 2.2. The curves shown in Figure 2.2 are normalized to have the same potential at the edges ($|r| = r_0$) of the multipole device. It should be pointed out that the absolute voltage applied to

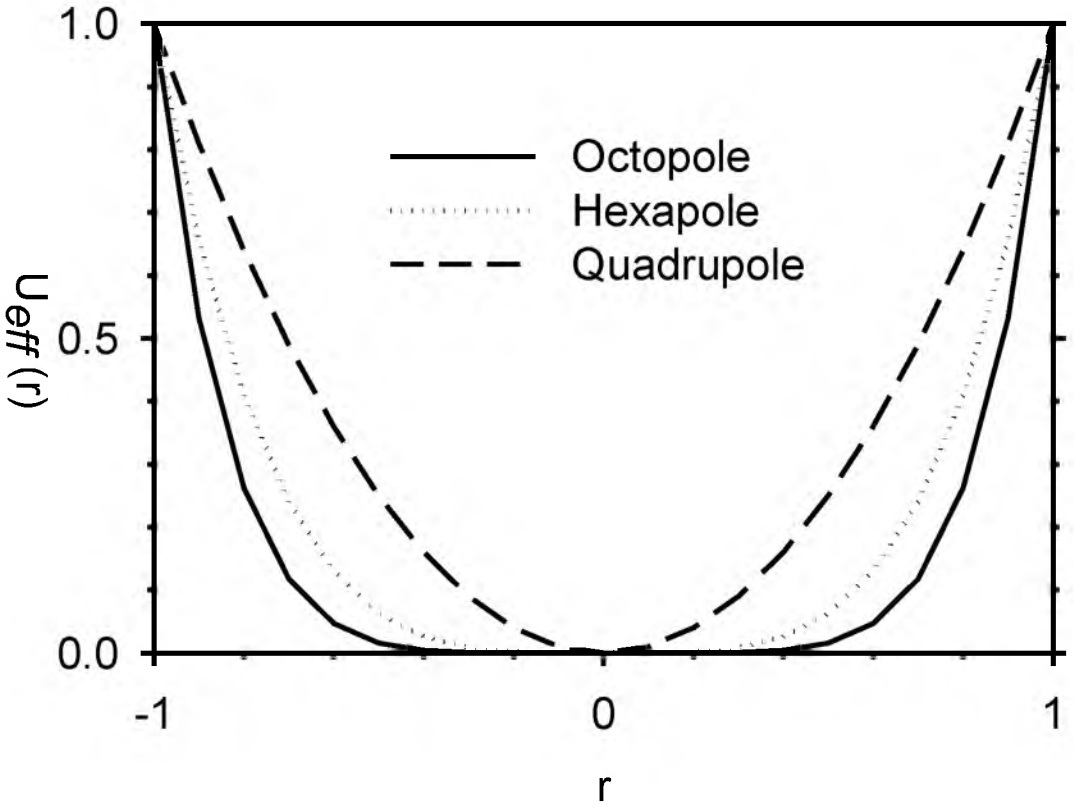

Figure 2.2 Comparison of the r^6 effective potential of the octopole to those (r^4 and r^2) of the hexapole and quadrupole.

quadrupole must be four times larger than that applied to the octopole to equalize the trapping potentials at the edges of the devices (n^2 term in equation 2.1). Thus, ions with transverse kinetic energy are less likely to be ejected from an octopole than from a quadrupole operating at the same rf potential. Our experience with this guided ion beam mass spectrometer indicates that forward scattered ions (in the laboratory frame) are routinely collected with near unit efficiency at low to moderate kinetic energies (0 to 10 eV or so). Ion loss is more probable at higher kinetic energies. Nevertheless, the experiments discussed in this thesis show no obvious signs of ion loss at any energy.

Another critical aspect deals with the relative flatness of the r^6 curve compared to the r^2 curve near the center of the trap. The kinetic energy of ions near the axis ($r = 0$) of an octopole is relatively unaffected by the trapping field. The energy of ions trapped by a quadrupole, however, is continuously being converted from kinetic to potential, and back again. Thus, the kinetic energy of ions in an octopole is more well-defined compared to ions in a quadrupole. Ultimately, this leads to more reliable thermochemical data.

2.4 Thermochemical Analysis

Ion kinetic energies in the laboratory frame, E_{lab}, are converted to energies in the center-of-mass frame, E_{CM}, using equation 2.2,

$$E_{CM} = E_{Lab} \cdot m / (m + M) \qquad (2.2)$$

where m and M are the neutral and ionic reactant masses, respectively. This conversion is necessary because the momentum of the center-of-mass for the collision pair through

the laboratory is conserved and is therefore unavailable to reactions. All energies reported below are in the CM frame unless otherwise noted.

Raw ion-intensities are converted to reaction cross sections using an analog to Beer's law, equations 2.3 and 2.4.

$$\ln(I_0 / I) = \sigma_{tot} n l \tag{2.3}$$

$$\sigma_P = \sigma_{tot}(I_P / \Sigma I_P) \tag{2.4}$$

I_0 is the incident reactant ion intensity, I is the transmitted ion intensity, σ_{tot} is the total reaction cross section, n is the neutral gas number density, l is the effective gas-cell path length (8.26 cm), and σ_P is a product cross section whose transmitted intensity is I_P. It is assumed that $I_0 = I + \Sigma I_P$. Given the radial trapping efficiency of the octopole ion beam guide, this is generally a reasonable assumption.

Cross sections for exothermic reactions are usually described by the Langevin-Gioumousis-Stevenson (LGS) model,[10] equation 2.5

$$\sigma_{LGS} = \pi e (\alpha / 2 \pi \varepsilon_0 E)^{1/2} \tag{2.5}$$

where e is the electron charge, α is the polarizability of the neutral reactant molecule, and E is the relative kinetic energy of the reactants. Many cross sections for the exothermic reactions follow this type of energy dependence, although deviations from this behavior are commonly observed.[11] The reaction efficiencies for exothermic reactions are assessed by comparing the cross sections measured using the GIBMS to σ_{LGS}.

Most of the cross sections determined in this work are for endothermic reactions, i.e., the cross section is zero until the kinetic energies reach the threshold and then

increases as the kinetic energy of the ion increases. The kinetic-energy dependence of product cross sections is analyzed to determine E_0, the energy threshold for product formation at 0 K. The apparent threshold observed under laboratory conditions can lie below E_0 because of the kinetic and internal energy distributions of the reactants. To determine E_0, endothermic reaction cross sections are modeled using equation 2.6,[12-14]

$$\sigma(E) = \sigma_0 \sum_i g_i (E + E_i + E_{rot} - E_0)^n / E \qquad (2.6)$$

where σ_0 is an energy-independent scaling factor, E is the relative kinetic energy of the reactants, n is an adjustable parameter, E_{rot} is the rotational energy of the diatomic reactant (= $k_B T$ at 300 K = 0.026 eV), and E_0 is the 0 K threshold for reaction of electronic, vibrational, and rotational state reactants. There is an explicit sum of contributions from rovibrational states of reactants at 300 K, denoted by i, having energies E_i and populations g_i, where $\Sigma g_i = 1$. For the reaction of transition metal ion M^+ with bimolecular compounds such as H_2/D_2, endothermic reaction cross sections are also modeled using equation 2.7 which includes a model for dissociation above the neutral reactant's BDE,[15]

$$\sigma(E) = \sigma_0[\Sigma g_i(E + E_i - E_0)^n/E^m][1 - P_D(E - E_0)] \qquad (2.7)$$

where P_D is the dissociation probability, which relies in a complicated way detailed elsewhere[15] on two parameters: E_D, the onset for product dissociation, and p, a parameter similar to n.

Before comparison with experimental data, equation 2.6 is convoluted with the kinetic energy distributions of the ions and neutral reactants at 300 K. The σ_0, n, and E_0

parameters are then optimized using a nonlinear least-squares analysis to give the best reproduction of the data.[13,14] Error limits for E_0 are calculated from the range of threshold values for different data sets over a range of acceptable n values combined with the absolute uncertainty in the kinetic energy scale.

Bond energies are one of the primary thermodynamic quantities extracted from our threshold measurements of ion-molecule reactions. They are calculated by summing the reaction enthalpies of appropriate individual chemical processes, utilizing the fact that enthalpy is a thermodynamic state-function that is not path-dependent (Hess's law). From the experimentally-measured threshold, E_0, for an ion-molecule reaction of the type

$$A^+ + BC \rightarrow AB^+ + C \qquad (2.8)$$

the bond energy of species AB^+ at zero Kelvin, $D_0(A^+–B)$, may be calculated according to equation 2.9,

$$D_0(A^+–B) = D_0(B–C) - E_0 \qquad (2.9)$$

provided $D_0(B–C)$ is known. This is easily seen by noting that reactions $BC \rightarrow B + C$ and $AB^+ + C \rightarrow A^+ + BC$ have enthalpies of $D_0(B–C)$ and $-E_0$, respectively. The sum of these equations yields the overall reaction $AB^+ \rightarrow A^+ + B$ (after cancellation of like terms), whose overall reaction enthalpy is $D_0(A^+–B)$ by definition. Heats of formation at zero Kelvin, $\Delta_fH°$, may also be calculated using the relation $\Delta_fH°_{rxn} = \Sigma\Delta_fH°_{products} - \Sigma\Delta_fH°_{reactants}$.

2.5 Theoretical Calculations

Most quantum chemistry calculations here are computed with the B3LYP hybrid density functional method[16,17] and performed with the GAUSSIAN 03[18] and 09[19] suites of programs. The B3LYP method is used because it provides reasonable results for analogous metal hydride and metal oxide systems. The B3LYP method is a density functional hybrid method that uses Becke's 3 parameter exchange functional (B3) and the Lee-Yang-Parr (LYP) correlation functional. Another density functional hybrid method, Becke-half-and-half-LYP (BHLYP),[20] uses Becke's half-and-half functional (BH) exchange functional, which includes 50% HF exchange and 50% Slater exchange, along with the LYP correlation functional. Two post Hartree-Fock (HF) methods were also used in these studies, QCISD(T) and CCSD(T). The QCISD(T) method[21] is a quadratic configuration interaction (CI) method method that uses single, double, and perturbative triple mixing of excited states to account for electron correlation. The CCSD(T) method[22-25] is a coupled cluster (CC) method that uses a single and double excitations along with a balanced perturbative correction term for connected triple excitations. For the various metals studied here, three basis sets were considered, HW+, Def2TZVPP, and Stuttgart-Dresden (SDD), all using effective core potentials (ECPs) that are small core (60 electrons) in which the 5s, 5p, 5d, and 6s orbitals are retained in the valence space. Both the Def2TZVPP and Stuttgart-Dresden (SDD) approaches use ECPs developed by Andrae *et al.*[26] The Def2TZVPP basis set includes f and g type polarization functions on the metal,[27] whereas neither the HW+ nor the SDD basis sets do. The HW+ basis set has been developed by Ohanessian *et al.*[28] and uses the ECP of Hay-Wadt (HW), with the valence electrons described by the Los Alamos double-ζ basis set (LANL2DZ). The HW

basis set is optimized for neutral atoms, whereas the HW+ basis set accounts for the differential contraction of the s orbitals compared to the d orbitals resulting from the positive charge. We also examined results calculated using the SDD basis set of Dolg *et al.*[29] For the nonmetals studied here, the basis sets 6-311G++(3df,3p) and Def2TZVPP were used. These basis set give good results for the thermochemistry of H_2, with calculated bond energies of 4.505 and 4.507 eV, respectively, versus the experimental bond energy of 4.478 eV.[30] Similarly, good agreement was found for CO and O_2. Calculated BDEs for CO were 11.059 and 10.933 eV for 6-311G++(3df,3p) and Def2TZVPP compared to the experimental bond energy of 11.108 eV.[30] For O_2, the calculated BDEs were 5.279 and 5.265 eV, respectively, compared to an experimental bond energy of 5.115 eV.[30] In all cases, the thermochemistry calculated and cited here is corrected for zero point energy effects, after scaling the frequencies by 0.9804.[31]

Holthausen *et al.*[32] carefully considered the most appropriate choice for a level of theory for the first and third row transition metal methyl cations. These authors used B3LYP, Becke-half-and-half-LYP (BHLYP), and QCISD(T) methods with a basis set consisting of a polarized double-ζ on C and H and the Hay/Wadt relativistic ECP with valence electrons added. The symmetries of the metal methyl species were constrained to C_{3v}. Upon comparison with experimental results for the first row MCH_3^+ species (M = Sc - Cu),[33,34] these authors conclude that the B3LYP functional overbinds, with a mean average deviation (MAD) from experiment of 0.41 eV, whereas the BHLYP functional and the QCISD(T) methods perform more accurately, with MADs of 0.18 and 0.20 eV, respectively. For the third-row elements, the bond energies calculated using B3LYP functional were again higher than those for BHLYP and QCISD(T) functional.

Additionally, several excited states for the reaction products are calculated along with relaxed potential energy surfaces (PES) to describe the reaction mechanism of the insertion of the metal ion into the neutral reaction partner as the bond angle is increased. For the excited states, these are found by taking the optimized ground state and moving one (or a few) electrons from an occupied orbital to an unoccupied orbital. The PESs for the activation of small molecules by M^+ are determined by taking the optimized structure of the L-M^+-L species (where L is the ligand H, C, or O) and varying the bond length over the global surface from reactant to intermediates to products.

2.6 References

[1] S. K. Loh, D. A. Hales, L. Lian, and P. B. Armentrout, J. Chem. Phys. **90**, 5466 (1989).

[2] R. H. Schultz and P. B. Armentrout, Int. J. Mass Spectrom. Ion Processes **107**, 29 (1991).

[3] E. Teloy and D. Gerlich, Chem. Phys. **4**, 417 (1974).

[4] D. Gerlich, Adv. Chem. Phys. **82**, 1 (1992).

[5] K. M. Ervin and P. B. Armentrout, J. Chem. Phys. **83**, 166 (1985).

[6] P. J. Chantry, J. Chem. Phys. **55**, 2746 (1971).

[7] R. H. Schultz and P. B. Armentrout, J. Chem. Phys. **96**, 1046 (1992).

[8] R. H. Schultz, K. C. Crellin, and P. B. Armentrout, J. Am. Chem. Soc. **113**, 8590 (1991).

[9] F. A. Khan, D. C. Clemmer, R. H. Schultz, and P. B. Armentrout, J. Phys. Chem. **97**, 7978 (1993).

[10] G. Gioumousis and D. P. Stevenson, J. Chem. Phys. **29**, 294 (1958).

[11] P. B. Armentrout, in *Structure/Reactivity and Thermochemistry of Ions*; P. Ausloos, S. G. Lias, Eds., D. Reidel: Dordrecht, 1987.

[12] W. J. Chesnavich and M. T. Bowers, J. Phys. Chem. **83**, 900 (1979).

[13] N. Aristov and P. B. Armentrout, J. Am. Chem. Soc. **108**, 1806 (1986).

[14] P. B. Armentrout, *In Advances in Gas-Phase Ion Chemistry*, edited by N. G. Adams and L. M. Babcock (JAI: Greenwich, 1992) 83.

[15] M. E. Weber, J. L. Elkind, and P. B. Armentrout, J. Chem. Phys. **84**, 1521 (1986).

[16] A. D. Becke, J. Chem. Phys. **98**, 5648 (1993).

[17] C. Lee, W. Yang, and R. G. Parr, Phys. Rev. B **37**, 785 (1998).

[18] M. J. Frisch, G. W. Trucks, H. B. Schlegel, G. E. Scuseria, M. A. Robb, J. R. Cheeseman, J. A. Montgomery, Jr., T. Vreven, K. N. Kudin, J. C. Burant, J. M. Millam, S. S. Iyengar, J. Tomasi, V. Barone, B. Mennucci, M. Cossi, G. Scalmani, N. Rega, G. A. Petersson, H. Nakatsuji, M. Hada, M. Ehara, K. Toyota, R. Fukuda, J. Hasegawa, M. Ishida, T. Nakajima, Y. Honda, O. Kitao, H. Nakai, M. Klene, X. Li, J.

E. Knox, H. P. Hratchian, J. B. Cross, V. Bakken, C. Adamo, J. Jaramillo, R. Gomperts, R. E. Stratmann, O. Yazyev, A. J. Austin, R. Cammi, C. Pomelli, J. W. Ochterski, P. Y. Ayala, K. Morokuma, G. A. Voth, P. Salvador, J. J. Dannenberg, V. G. Zakrzewski, S. Dapprich, A. D. Daniels, M. C. Strain, O. Farkas, D. K. Malick, A. D. Rabuck, K. Raghavachari, J. B. Foresman, J. V. Ortiz, Q. Cui, A. G. Baboul, S. Clifford, J. Cioslowski, B. B. Stefanov, G. Liu, A. Liashenko, P. Piskorz, I. Komaromi, R. L. Martin, D. J. Fox, T. Keith, M. A. Al-Laham, C. Y. Peng, A. Nanayakkara, M. Challacombe, P. M. W. Gill, B. Johnson, W. Chen, M. W. Wong, C. Gonzalez, and J. A. Pople Gaussian 03, Revision B.02, Gaussian Inc., Wallingford CT (2004).

[19] M. J. Frisch, G. W. Trucks, H. B. Schlegel, G. E. Scuseria, M. A. Robb, J. R. Cheeseman, G. Scalmani, V. Barone, B. Mennucci, G. A. Petersson, H. Nakatsuji, M. Caricato, X. Li, H. P. Hratchian, A. F. Izmaylov, J. Bloino, G. Zheng, J. L. Sonnenberg, M. Hada, M. Ehara, K. Toyota, R. Fukuda, J. Hasegawa, M. Ishida, T. Nakajima, Y. Honda, O. Kitao, H. Nakai, T. Vreven, J. A. Montgomery, Jr., J. E. Peralta, F. Ogliaro, M. Bearpark, J. J. Heyd, E. Brothers, K. N. Kudin, V. N. Staroverov, R. Kobayashi, J. Normand, K. Raghavachari, A. Rendell, J. C. Burant, S. S. Iyengar, J. Tomasi, M. Cossi, N. Rega, J. M. Millam, M. Klene, J. E. Knox, J. B. Cross, V. Bakken, C. Adamo, J. Jaramillo, R. Gomperts, R. E. Stratmann, O. Yazyev, A. J. Austin, R. Cammi, C. Pomelli, J. W. Ochterski, R. L. Martin, K. Morokuma, V. G. Zakrzewski, G. A. Voth, P. Salvador, J. J. Dannenberg, S. Dapprich, A. D. Daniels, Ö. Farkas, J. B. Foresman, J. V. Ortiz, J. Cioslowski, and D. J. Fox Gaussian 09, Revision A.02, Gaussian, Inc., Wallingford CT (2009).

[20] A. D. Becke, J. Chem. Phys. **98**, 1372 (1993).

[21] J. A. Pople, M. Head-Gordon, and K. Raghavachari, J. Chem. Phys. **87**, 5968 (1987).

[22] K. Raghavachari, G. W. Trucks, J. A. Pople, and M. Head-Gordon, Chem. Phys. Lett. **157**, 479 (1989).

[23] R. J. Bartlett, J. D. Watts, S. A. Kucharski, and J. Noga, Chem. Phys. Lett. **165**, 513 (1990).

[24] G. E. Scuseria and T. J. Lee, J. Chem. Phys. **93**, 5851 (1990).

[25] T. D. Crawford and J. F. Stanton, Int. J. Quantum Chem. **70**, 601 (1998).

[26] D. Andrae,U. Haeussermann, M. Dolg, H. Stoll, and H. Preuss, Theor. Chim. Acta, **77**, 123 (1990).

[27] F. Weigend and R. Ahlrichs, Phys. Chem. Chem. Phys., 7, 3297 (2005).

[28] G. Ohanessian, M. J. Brusich, and W. A. Goddard III, J. Am. Chem. Soc. **112**, 7179 (1990).

[29] M. Dolg, H. Stoll, H. Preuss, and R. M. Pitzer, J. Phys. Chem. **97**, 5852 (1993).

[30] K. P. Huber and G. Herzberg, *Molecular Spectra and Molecular Structure IV. Constants of Diatomic Molecules*, Van Nostrand Reinhold (New York, 1979).

[31] J. B. Foresman and Æ. Frisch, *Exploring Chemistry with Electronic Structure Methods*, 2nd Ed. (Gaussian, Pittsburgh, PA, 1996).

[32] M. C. Holthausen, C. Heinemann, H. H. Cornehl, W. Koch, and H. Schwarz, J. Chem. Phys. **102**, 4931 (1995).

[33] P. B. Armentrout and B. L. Kickel, in *Organometallic Ion Chemistry*, edited by B. S. Freiser (Kluwer, Dordrecht, 1996), p. 1.

[34] P. B. Armentrout, in *Topics in Organometallic Chemistry*, edited by J. M. Brown and P. Hofmann (Springer, Berlin, 1999), Vol. 4-I, p. 1.

CHAPTER 3

GUIDED ION BEAM AND THEORETICAL STUDY OF THE REACTIONS OF Hf^+ WITH H_2, D_2, AND HD

Christopher S. Hinton, P. B. Armentrout

Reprinted from ***The Journal of Chemical Physics, Volume 133***, *Issue 12*
Christopher S. Hinton, P. B. Armentrout, Guided Ion Beam and Theoretical Study of the Reactions of Hf^+ with H_2, D_2, and HD, Pages 124307-124316, with permission from American Institute of Physics

Guided ion beam and theoretical study of the reactions of Hf^+ with H_2, D_2, and HD

Christopher S. Hinton and P. B. Armentrout[a)]
Department of Chemistry, University of Utah, 315 South 1400 East, Room 2020, Salt Lake City, Utah 84112, USA

(Received 3 June 2010; accepted 4 August 2010; published online 24 September 2010)

The kinetic energy dependences of reactions of the third-row transition metal cation Hf^+ with H_2, D_2, and HD were determined using a guided ion beam tandem mass spectrometer. A flow tube ion source produces Hf^+ in its ^2D ($6s^25d^1$) electronic ground state level. Corresponding state-specific reaction cross sections are obtained. The kinetic energy dependences of the cross sections for the endothermic formation of HfH^+ and HfD^+ are analyzed to give a 0 K bond dissociation energy of $D_0(Hf^+-H)=2.11\pm0.08$ eV. Quantum chemical calculations at several levels of theory performed here generally overestimate the experimental bond energy but results obtained using the Becke-half-and-half-LYP functional show good agreement. Theory also provides the electronic structures of these species and the reactive potential energy surfaces. Results from the reactions with HD provide insight into the reaction mechanisms and indicates that Hf^+ reacts via a statistical mechanism. We also compare this third-row transition metal system with the first-row and second-row congeners, Ti^+ and Zr^+, and find that Hf^+ has a weaker M^+-H bond. As most third-row transition metal hydride cation bonds exceed their lighter congeners, this trend is unusual but can be understood using promotion energy arguments. © *2010 American Institute of Physics.* [doi:10.1063/1.3482663]

I. INTRODUCTION

Insight into the activation of covalent bonds, important processes in many homogeneous and heterogeneous catalytic processes,[1,2] can be obtained in many ways. Among the simplest, and therefore potentially among the most valuable because it can be studied in detail both experimentally and theoretically, is the activation of dihydrogen at single metal centers. The periodic trends in this chemistry are particularly interesting[3,4] and there are now numerous experimental studies of the reactions of the ions of atomic first-row transition metals,[5–16] second-row transition metals,[10,15,17–19] third-row transition metals,[17,20–23] and other metals[24–28] with dihydrogen, reaction (1), and its isotopic analogues.

$$M^+ + H_2 \rightarrow MH^+ + H. \quad (1)$$

In addition to the kinetics and dynamics of this reaction, the guided ion beam methods used in our laboratory can also measure the bond dissociation energy (BDE) of M^+-H by analysis of the kinetic energy dependence of reaction (1).[29–31] Such thermochemistry is of obvious fundamental interest and has implications for understanding a variety of catalytic reactions involving transition metal systems.[1,2]

In an ongoing systematic study of reaction (1) for the third-row transition metal cations, we have previously studied La^+,[17] Ta^+,[20] W^+,[20] Re^+,[22] Ir^+,[23] Pt^+,[21] and Lu^+ (Ref. 17) using guided ion beam tandem mass spectrometry. Previous theoretical studies include all of the third-row transition metal hydride cations.[32–39] We continue these studies here by reporting absolute cross sections as a function of kinetic energy for reactions of H_2, HD, and D_2 with Hf^+ and analyze them to acquire $D_0(Hf^+-H)$. Detailed theoretical calculations on the HfH^+ and HfH_2^+ species were performed to assign electronic structures and explore possible mechanisms for these reactions. Experimental branching ratios for reaction with HD also provide mechanistic insight, which is compared with results for the lighter group IV congeners, Ti^+ and Zr^+.[16,19] Little information exists in the literature on hafnium hydride. Previous work has detected HfH^+ formation by fluorescence spectroscopy,[40] and this species is found to be the dominant product formed in the reaction of Hf^+ with methane at elevated collision energies.[41] In that study, it was found that Hf^+ was relatively unreactive compared to most third-row transition metal cations, a result attributed to the doubly occupied 6s orbital of its ^2D ground state.

II. EXPERIMENTAL SECTION

A. General

The guided ion beam tandem mass spectrometer on which these experiments were performed has been described in detail previously.[42] Briefly, atomic metal ions are generated in a direct current discharge flow tube (DC/FT) source described below,[43] extracted from the source, accelerated, and focused into a magnetic sector momentum analyzer for mass selection of primary ions. The mass-selected ions are decelerated to a desired kinetic energy and focused into an octopole ion beam guide that uses radio-frequency electric fields to trap the ions in the radial direction and ensure complete collection of reactant and product ions.[44,45] The octopole passes through a static gas cell with an effective length

a)Electronic mail: armentrout@chem.utah.edu.

TABLE I. Electronic states and populations of Hf cations.

State	Configuration	Energy (eV)[a]
^2D	$6s^25d^1$	0.227
^4F	$6s^15d^2$	0.790
^4P	$6s^15d^2$	1.617
^2F	$6s^15d^2$	1.710
^2D	$6s^15d^2$	2.004
^2P	$6s^15d^2$	2.104
^2G	$6s^15d^2$	2.173
^4F	$5d^3$	2.661
^2G	$5d^3$	3.454

[a]Energies are the average of all spin-orbit levels taken from Ref. 54 relative to the $^2D_{3/2}$ ground state level.

of 8.26 cm that contains the reaction partner (here, H_2, HD, or D_2) at a low pressure (usually less than ~0.3 mTorr) so that multiple ion-molecule collisions are improbable. All products reported here result from single bimolecular encounters, as verified by pressure dependence studies. The unreacted parent and product ions are confined radially in the guide until they drift to the end of the octopole where they are extracted, focused, and passed through a quadrupole mass filter for mass analysis of products. Ions are subsequently detected with a secondary electron scintillation ion detector[46] using standard pulse counting techniques. Reaction cross sections are calculated from product ion intensities relative to reactant ion intensities after correcting for background signals.[47] Uncertainties in absolute cross sections are estimated to be ±20%.

The kinetic energy of the ions is varied in the laboratory frame by scanning the dc bias on the octopole rods with respect to the potential of the ion source region. Laboratory (lab) ion energies are converted to energies in the center-of-mass frame (CM) by using the formula $E_{CM}=E_{lab}m/(m+M)$, where m and M are the neutral and ionic reactant masses, respectively. Two effects broaden the cross section data: the kinetic energy distribution of the reactant ion and the thermal motion of the neutral reactant gas (Doppler broadening).[48] The absolute zero and the full width at half maximum (FWHM) of the kinetic energy distribution of the reactant ions are determined using the octopole beam guide as a retarding potential analyzer, as described previously.[47] The distributions of ion energies, which are independent of energy, are nearly Gaussian and have a typical FWHM of 0.4–0.9 eV (lab) in these studies. These values are somewhat larger than is usual for this instrument in part because of the extremely wide energy range needed in these studies (lab energies from 0 to 800 eV). This requires different focusing of the ion beam than is optimal for determining the zero of energy and energy distributions. Uncertainties in the absolute zero of the energy scale are ±0.1 eV (lab).

B. Ion source

Hf^+ ions are produced in a DC/FT source, consisting of a cathode held at a high negative voltage (1.1–1.5 kV) over which a flow of approximately 90% He and 10% Ar passes at a total pressure of 0.3–0.5 Torr. The dc-discharge ionizes Ar and then accelerates these ions into the cathode made of either tantalum or iron with a cavity containing hafnium metal. As the ions are swept down the 1 m flow tube, they undergo ~10^5 thermalizing collisions with He and Ar. No evidence for low-lying excited states of the metal ions (such as cross section features having lower energy thresholds) within about 1% sensitivity is observed under these flow conditions either in this work or in previous studies of Hf^+.[41,49] When compared to a surface ionization source, the DC/FT source has been found to generate Sc^+,[50] Fe^+,[51] Co^+,[52] Ni^+,[53] Ru^+,[18] Rh^+,[18] and Pd^+ (Ref. 18) ions with an average electronic temperature of 700 ± 400 K, and Y^+, Zr^+, Nb^+, and Mo^+ ions with an average electronic temperature of 300 ± 100 K.[19] The various low-lying states of Hf^+ are listed in Table I.[54] Even at the maximum electronic temperature of 1100 K, only the lowest energy spin-orbit level ($^2D_{3/2}$) of Hf^+ is populated to any appreciable degree (96.3%) with the $^2D_{5/2}$ level at 0.378 eV having 2.6% of the population. Conservatively, the average electronic energy, E_{el}, at a temperature of 700 ± 400 K for Hf^+ is 0.006+0.010/−0.006 eV.

C. Data analysis

The cross sections of endothermic reactions are modeled using Eq. (2).[29–31,55–58]

$$\sigma(E)=\sigma_0\sum_i g_i(E+E_i+E_{rot}-E_0)^n/E, \quad (2)$$

where σ_0 is an energy-independent scaling factor, E is the relative kinetic energy of the reactants, n is an adjustable parameter that characterizes the energy dependence of the process, E_{rot} is the rotational energy of the diatomic reactant ($=k_BT$ at 300 K = 0.026 eV), and E_0 is the 0 K threshold for reaction of electronic, vibrational, and rotational ground state reactants. The model involves an explicit sum of the contributions of individual electronic states of the Hf^+ reactant, denoted by i, having energies E_i and populations g_i. Before comparison with the experimental data, Eq. (2) is convoluted with the kinetic energy distributions of the reactant ions and neutral reactants at 300 K. The σ_0, n, and E_0 parameters are then optimized using a nonlinear least-squares analysis to give the best reproduction of the data. Error limits for E_0 are calculated from the range of threshold values for different data sets over a range of acceptable n values combined with the absolute errors in the kinetic energy scale and internal energies of reactant ions.

At energies above $D_0(H_2)$ and $D_0(D_2)$, the analyses include a model for this subsequent dissociation, as outlined in detail elsewhere.[59] This high energy model requires two parameters: E_D fixes the onset for HfH^+ (HfD^+) dissociation and the exponent p determines the energy dependence, similar to n in Eq. (2). For the results shown below, E_D is fixed near the H_2 (D_2) bond energy and the optimum value of p was found to be 2.0.

III. EXPERIMENTAL RESULTS

A. Reactions with H_2 and D_2

Figures 1 and 2 show cross sections as a function of kinetic energy for the bimolecular reaction of H_2 and D_2 with

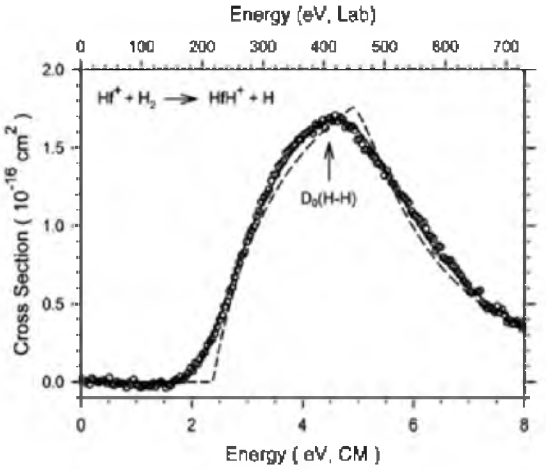

FIG. 1. Cross sections for the reaction of Hf^+ (^2D) with H_2 as a function of kinetic energy in the center-of-mass frame (lower axis) and laboratory frame (upper axis). The best fit to the data using Eq. (2) with parameters of Table II is shown as a dashed line. The solid line shows this model convoluted over the kinetic and internal energy distributions of the reactant neutral and ion. The arrow indicates $D_0(H-H)$ at 4.478 eV.

Hf^+ produced in the DC/FT source. Reaction (1) and its deuterated analogue are the only processes observed. Results for the reaction $Hf^+ + D_2$ are somewhat easier to acquire because the heavier isotope reduces mass overlap between the product ion and the much more intense primary ion, thereby allowing intensities of the product ion to be measured more accurately over a larger dynamic range. However, the same mass resolution conditions were used to collect data for the H_2, D_2, and HD systems here. The absolute magnitudes of the $Hf^+ + H_2$ and $Hf^+ + D_2$ reaction cross sections differ by about 25%, comparable to the estimated 20% experimental

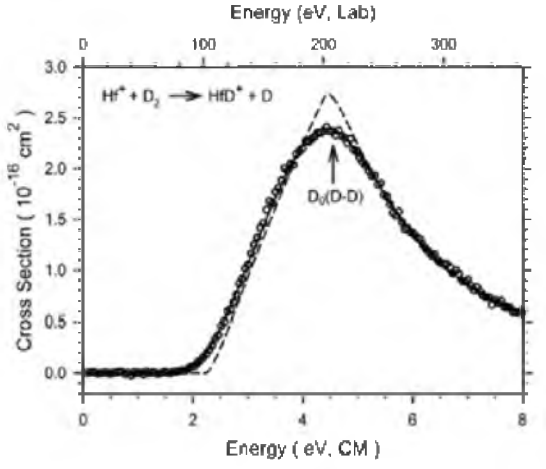

FIG. 2. Cross sections for the reaction of Hf^+ (^2D) with D_2 as a function of kinetic energy in the center-of-mass frame (lower axis) and laboratory frame (upper axis). The best fit to the data using Eq. (2) with parameters of Table II is shown as a dashed line. The solid line shows this model convoluted over the kinetic and internal energy distributions of the reactant neutral and ion. The arrow indicates $D_0(D-D)$ at 4.556 eV.

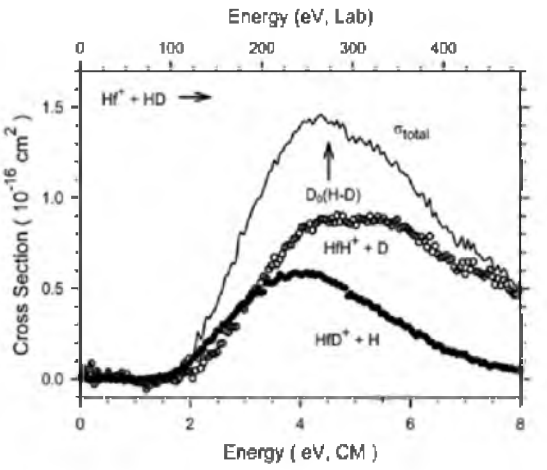

FIG. 3. Cross sections for the reaction of Hf^+ (^2D) with HD as a function of kinetic energy in the center-of-mass frame (lower axis) and laboratory frame (upper axis). The arrow indicates $D_0(H-D)$ at 4.514 eV.

uncertainty. The energy dependences of the cross sections for the two systems are quite similar when plotted on the center-of-mass energy scale.

The cross sections rise from apparent thresholds near 1.7 eV and reach maxima near the dissociation energy of H_2, $D_0(H_2)=4.478$ eV, or D_2, $D_0(D_2)=4.556$ eV.[60] At higher energies, the HfH^+ (HfD^+) products can be formed with internal energies in excess of the BDE, such that these products begin to dissociate in the overall reaction (3)

$$Hf^+ + H_2(D_2) \rightarrow HfH^+(HfD^+) + H(D) \rightarrow Hf^+ + 2H(D). \quad (3)$$

The observation that the experimental cross sections reach maxima very close to the H_2 (D_2) bond energies illustrates that these processes begin promptly at their thermodynamic threshold.

B. Reactions with HD

Hf^+ reacts with HD to yield both HfH^+ and HfD^+ in reactions (4) and (5) as shown in Fig. 3.

$$Hf^+ + HD \rightarrow HfH^+ + D, \quad (4)$$

$$\rightarrow HfD^+ + H. \quad (5)$$

Because of the close proximity of the product masses, there can easily be some overlap between these signals depending on the mass resolution used in the quadrupole mass filter. In the present system, it was carefully checked that high resolution leading to separation of these products could be used without sacrificing efficient collection of the product ions. The accuracy of the final results is confirmed by reasonable agreement between the magnitudes of the total cross sections for the HD system and those of the H_2 and D_2 systems (Figs. 1 and 2).

The total cross section in the HD system exhibits endothermic behavior and rises from an apparent threshold that is similar to those of the H_2 and D_2 systems. The total cross

TABLE II. Parameters of Eq. (2) used in modeling reaction (1) and its deuterated analogue and the resultant bond energies.

Reactants	Products	σ_0	n	E_0 (eV)	$D_0(Hf^+-H)$
$Hf^+ + H_2$	$HfH^+ + H$	3.5 (0.3)	0.9 (0.1)	2.42 (0.05)	2.06 (0.05)
$Hf^+ + D_2$	$HfD^+ + D$	4.0 (0.3)	1.1 (0.3)	2.34 (0.06)	2.18 (0.06)[a]

[a]Value corrected for the zero point energy difference of 0.034 eV. See text.

section reaches a maximum near the BDE of HD: 4.514 eV.[60] The individual HfH^+ and HfD^+ cross sections behave somewhat differently such that the HfD^+ cross section rises from a slightly earlier apparent onset and then peaks at a somewhat lower energy than that of HfH^+. This behavior can be rationalized because the $HfD^+ + H$ product channel has a lower energy threshold by the zero point energy difference of 0.036 eV (given the 1979 cm^{-1} vibrational frequency for HfH^+ calculated by Ohanessian *et al.*[32]). At higher energies, the HfD^+ cross section declines at an energy somewhat before the onset of dissociation in the analogue of reaction (3). The relative high-energy behavior shows that the more massive D atom carries away more energy from HfH^+ than the lighter H atom carries away from HfD^+. This effect is typical of atomic ion reactions with H_2, HD, and D_2,[4,15,18,19] and has been discussed in more detail elsewhere.[4,61–63]

C. Thermochemical results

The endothermic cross sections in the H_2 and D_2 reaction systems are analyzed in detail using Eq. (2). Typical models are shown in Figs. 1 and 2 and can be seen to reproduce the experimental results very well throughout the energy range examined. The optimum values of the parameters in Eq. (2) for these systems are listed in Table II. As can be seen in Figs. 1 and 2, the optimum values of E_0 differ appreciably from the apparent thresholds, which are largely a result of the appreciable velocity distribution of the light H_2 (D_2) reactants. Because the convoluted form of Eq. (2) includes all sources of energy (rotational, vibrational, translational, and electronic energy distributions of reactants are explicitly included in the modeling), the E_0 threshold energies determined correspond to 0 K values. From the thresholds measured, the BDEs for the metal-ligand cations observed in reaction (1) can be calculated using Eq. (6).

$$D_0(Hf^+ - H) = D_0(H_2) - E_0. \quad (6)$$

An analogous equation is used to analyze results for the deuterated system. This equation assumes that there is no activation barrier in excess of the endothermicity of the reaction, an assumption that is often true for ion-molecule reactions because of the long-range attractive forces[57] and one that can be tested using theory (see below). A summary of the Hf^+-H bond energies derived from the present experiments with both H_2 and D_2 is given in Table II. This includes adjusting the value for $D_0(Hf^+-D)$ for the zero point energy difference between HfD^+ and HfH^+. This correction uses a vibrational frequency of 1895 cm^{-1} for HfH^+ and 1344 cm^{-1} for HfD^+, as calculated here for the $^1\Sigma^+$ state (see below), a value that agrees well with a 1979 cm^{-1} value calculated by Ohanessian *et al.*[32] for HfH^+. Thus the zero point energy differences in the HfH^+ and HfD^+ bond energies are 0.034 ± 0.003 eV, assuming a 10% uncertainty in the frequencies. The Hf^+-H bond energies obtained from the H_2 and D_2 systems are in excellent agreement with one another (Table II). Our best value for this bond energy is the weighted average of these two values, 2.11 ± 0.08 eV, where the uncertainty is two standard deviations. This value is in good agreement with the value of 1.97 ± 0.11 eV for $D_0(HfH^+)$ that was previously measured in the reaction of Hf^+ with CH_4.[41] The present value is considered more reliable as there are no competing channels that might shift the threshold to higher energies.

IV. THEORETICAL CALCULATIONS

A. General

Most quantum chemistry calculations reported here are computed using the B3LYP hybrid density functional method (Becke's three-parameter exchange functional with the Lee, Yang, and Parr correlation functional)[64,65] and performed with the GAUSSIAN 03 suite of programs.[66] A large basis set is used for hydrogen, triple zeta with diffuse and polarization functions, 6-311+G(3*p*). This basis set gives good results for the thermochemistry of dihydrogen, with deviations from experiment of less than 0.03 eV for the bond energy of H–H (4.505 eV calculated versus 4.478 eV experimental).[67] The 60 core electrons of hafnium are described by the relativistic effective core potentials (ECPs) of Hay–Wadt (HW),[68] with valence electrons described by the Los Alamos double zeta basis set (LANL2DZ). This basis set is optimized for neutral atoms, whereas the positive charge differentially contracts the *s* orbitals compared to the *d* orbitals. Hence, all calculations were performed with an altered HW-ECP basis for Hf^+ as described by Ohanessian *et al.* (HW+).[32] In all cases, the thermochemistry calculated and cited here is corrected for zero point energy effects, after scaling the frequencies by 0.9804.[69] We also examined results (geometries and single point energies) calculated using Def2TZVPP, a balanced basis set of triple zeta valence quality for both elements,[70] as well as the Stuttgart–Dresden (SDD) basis set[71] for Hf [retaining the 6-311+G(3*p*) basis on hydrogen]. The Def2TZVPP basis set includes *f* and *g* type polarization functions on Hf, whereas neither the HW+ nor the SDD basis sets do. Both the Def2TZVPP and SDD basis sets use ECPs developed by Andrae *et al.*[71] for Hf.

Holthausen *et al.*[72] carefully considered the most appropriate choice for a level of theory for the first and third-row transition metal methyl cations, species analogous to the metal hydride cations considered here, because both have single covalent metal-ligand bonds. These authors used

TABLE III. Theoretical geometries and energies for HfH^+. (Results of B3LYP/HW+/6-311+G(3*p*) and B3LYP/Def2TZVPP (in italics) calculations. Energies for H at these levels of theory are −0.502 257 (*−0.498 545*) E_h).

				This work				Literature[a]		
Species	State	$s(s+1)$[b]	Configuration	Energy (E_h)	r ($M-X$) (Å)	ν (cm^{-1})[c]	E_{rel} (eV)[d]	r ($M-X$) (Å)	ν (cm^{-1})	E_{rel} (eV)
HfH^+	$^3\Delta$	2.00	$\sigma_b^2\sigma^1\delta^1$	−49.103 328	1.786	1806	0.000	1.786	1979	0.000
				−48.233 427	*1.798*	*1822*	*0.000*			
	$^1\Sigma^+$	0.00	$\sigma_b^2\sigma^2$	−49.098 748	1.747	1895	0.130			
				−48.227 966	*1.758*	*1908*	*0.154*			
	$^3\Pi$	2.00	$\sigma_b^2\sigma^1\pi^1$	−49.087 363	1.777	1784	0.433	1.779	1898	0.494
				−48.217 994	*1.789*	*1795*	*0.418*			
	$^1\Pi$	1.01	$\sigma_b^2\sigma^1\pi^1$	−49.083 655	1.781	1763	0.533			
	$^1\Delta$	1.00	$\sigma_b^2\sigma^1\delta^1$	−49.081 523	1.787	1797	0.593			
	$^3\Phi$	2.00	$\sigma_b^2\pi^1\delta^1$	−49.062 292	1.826	1674	1.108	1.829	2220	1.006
	$^3\Sigma^-$	2.00	$\sigma_b^2\delta^2$	−49.051 891	1.824	1668	1.389	1.831	1775	1.101
	$^1\Phi$	1.00	$\sigma_b^2\pi^1\delta^1$	−49.050 365	1.822	1689	1.434			
	$^1\Gamma$	0.00	$\sigma_b^2\delta^2$	−49.032 709	1.825	1721	1.916			
	$^1\Delta$	0.00	$\sigma_b^2\pi^2$	−49.009 065	1.815	1376	2.556			

[a]GVB values from Ohanessian *et al.* (Ref. 31).
[b]s is the spin quantum number, 0 for a singlet state, and 1 for a triplet state. Spin contamination is evident for the $^1\Pi$, $^1\Delta$, and $^1\Phi$ states.
[c]Vibrational frequencies scaled by 0.9804.
[d]Energies relative to the ground state including zero point energies.

B3LYP, Becke-half-and-half-LYP (BHLYP), and QCISD(T) (quadratic configuration interaction with single and double excitations added perturbatively) methods with a basis set consisting of a polarized double-ζ on C and H and the Hay/Wadt relativistic ECP with valence electrons added. The symmetries of the metal methyl species were constrained to C_{3v}. Upon comparison with experimental results for the first-row MCH_3^+ species (M=Sc–Cu),[29,30] these authors conclude that the B3LYP functional overbinds, whereas the BHLYP functional and the QCISD(T) methods perform more accurately. Mean absolute deviations from experiment were 0.41, 0.18, and 0.20 eV, respectively. Likewise, the bond energies calculated using B3LYP were higher than those for BHLYP and QCISD(T) for the third-row metal methyl cations. Given these results, we also performed calculations for the HfH^+ species using QCISD(T), the BHLYP functional, and CCSD(T) (coupled cluster with single and double excitations and triple excitations added perturbatively) levels of theory with the HW+, Def2TZVPP, and SDD (Ref. 71) ECPs for Hf^+. Such calculations will be explicitly noted and unless otherwise designated, our results will refer to a B3LYP/HW+/6-311+G(3*p*) level of theory. For HfH_2^+ species where multiple bonds to Hf^+ are formed, only the B3LYP functional is used. This choice is rationalized on the basis of the results of Holthausen *et al.*[73] for metal-methylene cations and our own studies of $HfCH_x^+$ (x =0–2) species.[41]

One means of evaluating the level of theory and basis set used in the calculations is to compare electronic excitation energies with those from experiment. Experimental values for the excitation energies (average over all spin-orbit states) from the ^2D ($6s^25d^1$) ground state to quartet states having $6s^15d^2$ and $6s^05d^3$ electron configurations are 0.563 and 2.434 eV, respectively (Table I).[54] Detailed results from various calculations are provided in supplementary material (table SI).[74] At the B3LYP and BHLYP levels of theory, similar values are obtained with excitation energies of 0.243–0.324 and 1.954–2.132 eV, slightly lower than experiment. Likewise, the values calculated at the QCISD(T) and CCSD(T) levels are nearly identical with values of 0.774–0.877 and 3.015–3.153 eV with the HW+ and SDD basis sets, somewhat higher than experiment. QCISD(T) and CCSD(T) calculations using the Def2TZVPP basis set provide the best reproduction of the experimental values: 0.508 and 2.490 eV. Thus, all levels of theory considered here reproduce the atomic excitation energies reasonably well although the QCISD(T) and CCSD(T) results are in the best agreement with experiment and the Def2TZVPP basis set performs better than the HW+/6-311+G(3*p*) combination, which is better than SDD/6-311+G(3*p*).

The experimental BDEs refer to the ground spin-orbit state at 0.0 eV, $^2D_{3/2}$ for Hf^+. In contrast, our calculations are referenced to the statistically weighted mean of all spin-orbit levels in the ground term, 0.227 eV for Hf^+ (^2D).[54] Because our calculations do not explicitly include spin-orbit interactions, it is possible that all calculated bond energies may need to be corrected by this different asymptotic energy before comparison with experimental values. In the generalized valence bond (GVB) calculations of Ohanessian *et al.*[32] it is suggested that spin-orbit energies may need to be taken into account in order to properly compare with experimental results. Explicit spin-orbit calculations for HfH^+ are beyond the scope of the present study.

B. HfH^+ states

The ground state of HfH^+ has been previously calculated by Ohanessian *et al.*[32] to be a $^3\Delta$ state where the character of the bonding orbital on Hf is 35% 6*s* and 64% 5*d*. The resultant bonding can be thought of as originating from a covalent sigma bond (σ_b^2) between the 1*s* orbital on H and a 6*s*5*d* hybrid orbital on Hf^+, which is formed by a combination of

TABLE IV. Bond energies (eV) calculated for the two lowest lying states of HfH$^+$ at several levels of theory including zero point energies.

State	Basis set	B3LYP	BHLYP	QCISD(T)	CCSD(T)
$^3\Delta^1$	HW+[b]	**2.71, 2.59**[a] (2.09)	**2.59, 2.48**[a] (1.97)	2.34, 2.08[a] (2.06)	2.28, 2.02[a] (2.00)
	Def2[d]	**2.62, 2.62**[a] (2.17)	**2.54, 2.54**[a] (2.02)	2.39, 2.34[a] (2.05)	2.39, 2.34[a] (2.05)
	SDD[e]	**2.63, 2.63**[a] (2.11)	**2.54, 2. 54**[a] (1.99)	2.27, 2.16[a] (2.24)	2.13, 2.01[a] (2.09)
$^1\Sigma^{+1}$	HW+[b]	2.58, 2.43[a] (2.20)	2.42, 2.28[a] (2.05)	**2.74, 2.40**[a] (2.17)	**2.71, 2.37**[a] (2.14)
	Def2[d]	2.47, 2.47[a] (2.24)	2.31, 2.31[a] (2.08)	**2.61, 2.55**[a] (2.32)	**2.61, 2.55**[a] (2.32)
	SDD[e]	2.45, 2.44[a] (2.21)	2.30, 2.28[a] (2.05)	**2.79, 2.58**[a] (2.35)	**2.79, 2.58**[a] (2.35)

[a]Values in parentheses include counterpoise corrections and correspond to the adiabatic bond energy after referencing the calculation to the Hf$^+$(^{4}F) asymptote and adjusting by the experimental excitation energy for this state, 0.790 eV. See text and Table I.
[b]Calculated using HW+/6-311+G(3*p*) basis set. Ground state in bold.
[c]Bond energy including counterpoise correction for basis set superposition error.
[d]Calculated using Def2TZVPP basis set for all atoms. Ground state in bold.
[e]Calculated using SDD/6-311+G(3*p*) basis set. Ground state in bold.
[f]Values in parentheses include counterpoise corrections and have been corrected by the 0.227 eV excitation for the average spin-orbit levels of the ^{2}D state. See text and Table I.

the ^{2}D ($6s^25d^1$) and ^{4}F ($6s^15d^2$) states of Hf$^+$. This type of hybridization is quite efficient in the third-row transition metals because relativistic effects make the 6*s* orbital comparable in size to the 5*d* orbitals. This 6*s*5*d* hybrid bonding orbital overlaps better with the 1*s* orbital on H(^{2}S) than pure 6*s* or 5*d* orbitals, even though binding to the hybrid orbital of Hf$^+$ requires both promotion and the loss of exchange energy because the ^{4}F state configuration is mixed in. The occupied nonbonding orbitals in the $^3\Delta$ state are $\sigma^1\delta^1$, where the σ orbital is the other 6*s*5*d* hybrid, the δ orbital is pure 5*d*, and for other states, there is a π orbital that is also pure 5*d*. The bond length calculated by Ohanessian *et al.*[32] is 1.786 Å, which is the same as the bond length calculated here at the B3LYP/HW+/6-311+G(3*p*) level.

A low-lying excited state of HfH$^+$ is the $^1\Sigma^+$ ($\sigma_b^2\sigma^2$) state, which lies 0.13–0.18 eV above the $^3\Delta$ ground state at the B3LYP level of theory (where the range comes from using all three basis sets noted above). The $^1\Sigma^+$ state is sufficiently close in energy to the $^3\Delta$ state that there is the possibility that this is the true ground state. The $^1\Sigma^+$ state is relatively low in energy because it can be formed directly from the Hf$^+$ (^{2}D, $6s^25d^1$) state (thereby avoiding promotion and exchange energy costs) by coupling the H(1*s*) electron with the 5*d*σ electron on Hf$^+$. The BHLYP level of theory agrees that the $^3\Delta$ state is the ground state, with excitation energies for the $^1\Sigma^+$ state of 0.17–0.24 eV. However, at the QCISD(T) and CCSD(T) levels of theory, the $^1\Sigma^+$ is calculated to be the ground state with the $^3\Delta$ state lying 0.22–0.52 and 0.22–0.66 eV higher, respectively (Table IV). Complicating the assignment of the true ground state is the fact that whereas the $^1\Sigma^+$ state can be derived from pure Hf$^+$ (^{2}D), the $^3\Delta$ state mixes in Hf$^+$ (^{4}F) character such that errors in the excitation energy of this state (see above and table SI) may propagate to the relative energies of the $^3\Delta$ and $^1\Sigma^+$ states. Indeed if the errors in the ^{4}F excitation energies noted above are included in full (yielding the BDEs listed in parentheses in Table IV), the $^1\Sigma^+$ state becomes the ground state at all levels of theory, with $^3\Delta$ excitation energies of 0.07–0.11, 0.06–0.08, 0.11–0.27, and 0.14–0.27 eV for the B3LYP, BHLYP, QCISD(T), and CCSD(T) calculations, respectively (Table IV). Another complication in determining the true ground state is that spin-orbit interactions will split the $^3\Delta$ state (but not the $^1\Sigma^+$), lowering the energy of one of its components, although by less than the atomic spin-orbit splitting of 0.227 eV.

We also calculated results for other stable excited states at the B3LYP/HW+/6-311+G(3*p*) level with relative energies listed in Table III. Ohanessian *et al.*[32] examined triplet excited states (but no singlet states) finding the $^3\Pi$ ($\sigma_b^2\sigma^1\pi^1$) at 0.49 eV, a $^3\Phi(\sigma_b^2\pi^1\delta^1)$ at 1.01 eV, and the $^3\Sigma^-(\sigma_b^2\delta^2)$ at 1.10 eV, all with bond lengths and excitation energies comparable to the present calculations (Table III). We located several additional singlet states, $^1\Pi$, $^1\Delta$, $^1\Phi$, $^1\Gamma$, and $^1\Delta$ with excitation energies between 0.5 and 2.6 eV (Table III).

Ohanessian *et al.* calculated a BDE for the $^3\Delta$ state of HfH$^+$ of 2.38 eV using GVB theory, a value somewhat above our experimental BDE. Meyer *et al.*[75] also calculated the $^3\Delta$ state of HfH$^+$ using multireference configuration interaction and obtained a BDE of 2.38 eV. Theoretical BDEs for this state calculated here at all levels of theory also exceed the experimental BDE if the values are referenced to the Hf$^+$ (^{2}D) state. If the theoretical BDEs are instead referenced to the ^{4}F state of Hf$^+$ and then corrected by the experimental excitation energy of the ^{4}F state for the reasons noted above, the $^3\Delta$ is no longer the ground state (Table IV). Now, the BDEs calculated for the $^1\Sigma^+$ state should be compared to the experimental value, which is still lower for all levels of theory. One reason for the discrepancy is to realize that the calculations are referenced to the average of the spin-orbit levels of Hf$^+$ (^{2}D), which experimentally lies 0.227 eV above the $^2D_{3/2}$ level, the experimental ground level. Therefore, the BDEs for the $^1\Sigma^+$ state in Table IV need to be reduced by this amount, as indicated by the values in parentheses. Now, the BHLYP values agree with experiment within the uncertainties, 2.05 (HW+), 2.08 (Def2TZVPP), and 2.05 (SDD) eV compared to 2.11 ± 0.08 eV. The B3LYP values remain slightly higher than experiment even with this correction, 2.20–2.24 eV, consistent with the observations of Holthausen *et al.* for metal-ligand single bonds. QCISD(T) and CCSD(T) values, which are similar to one another, also re-

TABLE V. Theoretical geometries and energies for HfH_2^+ calculated at the B3LYP/HW+/6-311+G(3*p*) level of theory.

State (configuration)	*r* (Hf–H) (Å)	*r* (H–H) (Å)	∠HHfH (deg)	Energy (E_h)	E_{rel} (eV)	ν (cm^{-1})[a]
$^2A_1(1a_1^2 1b_2^2 2a_1^1)$	1.779	2.740	100.7	−49.716 953 9	0.000	568, 1826, 1839
$^2B_1(1a_1^2 1b_2^2 1b_1^1)$	1.795	2.859	105.6	−49.698 069 6	0.513	634, 1776, 1803
$^2A_2(1a_1^2 1b_2^2 1a_2^1)$	1.788	2.640	95.2	−49.692 780 2	0.657	638, 1772, 1805
$^2B_2(1a_1^2 1b_2^1 2a_1^2)$	2.187	0.778	20.5	−49.685 250 2	0.863	455, 876, 3742
$^2B_1(1a_1^2 1b_1^1 2a_1^2)$	2.806	0.750	15.4	−49.681 595 8	0.962	18, 38, 148
$^2A_2(1a_1^2 1a_2^1 2a_1^2)$	3.487	0.745	12.3	−49.679 797 0	1.011	7, 15, 65
$^2A_1(1a_1^2 2a_1^2 3a_1^1)$	3.479	0.746	12.3	−49.679 776 8	1.012	7, 15, 67
$^4A_2(1a_1^2 1b_1^1 1b_2^1 2a_1^1)$	2.080	0.787	21.8	−49.677 154 5	1.083	697, 1075, 3295
$^4B_2(1a_1^2 1b_2^1 2a_1^1 3a_1^1)$	2.286	0.784	17.4	−49.676 974 1	1.088	520, 930, 3630
$^4B_1(1a_1^2 1b_2^1 1a_2^1 2a_1^1)$	2.114	0.794	21.7	−49.676 151 1	1.110	656, 1077, 3476
$^4A_2(1a_1^2 1a_2^1 2a_1^1 3a_1^1)$	3.448	0.746	12.4	−49.668 539 1	1.317	160, 171, 4279
$^4B_2(1a_1^2 1b_2^1 1a_2^1 2a_1^1)$	2.171	0.784	20.8	−49.668 038 8	1.331	346, 476, 4187
$^4A_1(1a_1^2 1b_2^1 1b_1^1 1a_2^1)$	1.999	0.822	23.7	−49.635 468 5	2.217	951, 1325, 3078
$^2\Sigma(1\sigma_g^2 1\sigma_u^1 2\sigma_g^2)$	1.930	3.860	180.0	−49.626 139 7	2.471	245, 296, 1065, 1419
$^4\Delta(1\sigma_g^2 1\sigma_u^1 1\delta^1 2\sigma_g^1)$	1.947	3.895	180.0	−49.622 490 5	2.570	184, 963, 1387
$^4\Pi(1\sigma_g^2 1\sigma_u^1 1\pi^1 2\sigma_g^1)$	1.912	3.825	180.0	−49.610 443 2	2.898	108, 695, 1086, 1410
$^4\Phi(1\sigma_g^2 1\sigma_u^1 1\pi^1 1\delta^1)$	1.949	3.898	180.0	−49.586 808 4	3.541	−213, 588, 1066, 1351

[a]Vibrational frequencies scaled by 0.9804. The energy of H_2 at this level of theory is −1.180 029 6 E_h with a vibrational frequency of 4418 cm^{-1} and bond length of 0.743 Å.

main slightly high, 0.03–0.24 eV above experiment, although HW+ values are within experimental uncertainty.

C. HfH_2^+ states

The properties of stable HfH_2^+ complexes found computationally are reported in Table V. For HfH_2^+, our B3LYP/HW+/6-311+G(3*p*) calculations find an inserted $^2A_1$ ground state with a BDE of 1.08 eV relative to the $Hf^+(^2D)+H_2$ asymptote. This state has a valence electron configuration of $(1a_1)^2(1b_2)^2(2a_1)^1$, where the $1a_1$ and $1b_2$ orbitals are Hf–H bonding orbitals, and the $2a_1$ is a nonbonding orbital that is mostly d_{x^2} (where the symmetry axis defines the *z* coordinate and the molecule lies in the *x*-*z* plane). Furthermore, we find $^2B_1$ and $^2A_2$ excited states lying 0.51 and 0.66 eV higher in energy, respectively. The $^2B_1$ has a $(1a_1)^2(1b_2)^2(1b_1)^1$ configuration where the $1b_1$ orbital is pure Hf($5d_{yz}$), and the $^2A_2$ state has a $(1a_1)^2(1b_2)^2(1a_2)^1$ configuration where the $1a_2$ orbital is pure Hf($5d_{xy}$). An excited $^2B_2$ state was found to lie 0.86 eV above the ground state but has long Hf–H bonds and a small ∠HHfH bond angle, indicating that it is an electrostatically bound $Hf^+(H_2)$ complex. This geometry is consistent with the $(1a_1)^2(1b_2)^1(2a_1)^2$ configuration of the $^2B_2$ state, which has only three electrons in the bonding orbitals. Likewise all bent quartet states located have similar geometries because they have at most three electrons in the bonding $1a_1$ and $1b_2$ orbitals (Table V). Additionally, one doublet and several quartet states of linear HfH_2^+ were found. All of these states can be characterized as having three electrons in the σ_g and σ_u bonding orbitals, with the remaining two electrons either in the slightly antibonding σ_g, or nonbonding π or δ orbitals. These linear species have Hf^+–H bond lengths of 1.91–1.95 Å and energies of 2.47–3.54 eV relative to the $^2A_1$ state.

The complete surfaces for the various HfH_2^+ states in C_{2v} symmetry as a function of bond angle are shown in Fig. 4. These were obtained from relaxed potential energy surface (PES) scan calculations starting at the optimized geometry of each state. Because of the C_{2v} symmetry restriction, the PESs in Fig. 4 cannot examine the HfH^++H dissociation asymptote. It seems likely that these products can be formed from the HfH_2^+ intermediates with no barriers in excess of the endothermicity for the following reasons. Both the $^1\Sigma^+$ and $^3\Delta$ states of HfH^+ can interact with H(^{2}S) to form low-spin doublet states of HfH_2^+. Covalent coupling of a nonbonding HfH^+ ($^3\Delta$) electron with H can occur along a doublet surface, such that the surface should be attractive. For the $^1\Sigma^+$ state of HfH^+, interaction with the 1*s* orbital of H gives rise to the $^2A_1(1a_1^2 1b_2^2 2a_1^1)$ state of HfH_2^+ (recogniz-

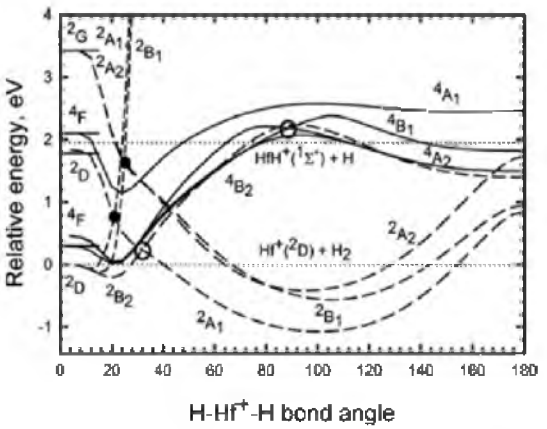

FIG. 4. B3LYP/HW+/6-311+G(3*p*) calculations of the PESs for the interaction of Hf^+ with H_2 in C_{2v} symmetry as a function of the H–Hf^+–H bond angle in degrees. Dotted lines indicate the experimental energy zero, corresponding to the $Hf^+(^2D)+H_2$ reactants at 0.0 eV, and the experimental energy of the $HfH^+(^1\Sigma^+)$+H products, 1.95 eV above the reactants. Circles indicate avoided surface crossings in C_{2v} (closed) and C_s (open) symmetry.

ing that all of these orbitals have a' symmetry as the HHf$^+$–H bond is broken). The $^3\Delta$ state of HfH$^+$ can also form high-spin quartet states of the intermediate, but these would be largely repulsive as no covalent bond formation is involved.

In Fig. 4, none of the low-lying doublet states of HfH_2^+ ($^2A_1$,$^2B_1$,$^2A_2$) leads diabatically to the $Hf^+(^2D,6s^25d^1)$ + H_2 reactant asymptote, but rather to $Hf^+(^2D,6s^15d^2)$ lying 1.78 eV (2.00 eV experimental) above the ground state or $Hf^+(^2G,5d^3)$ lying 3.43 eV (2.45 eV experimental) above the ground state. Instead, $Hf^+(^2D,6s^25d^1)$ interacts with H_2 in C_{2v} symmetry to form four surfaces having $^2A_1$, $^2A_2$, $^2B_1$, and $^2B_2$ symmetries (another $^2A_1$ surface cannot be separately characterized). The most favorable interaction between Hf^+ and H_2 occurs when there is an acceptor orbital on the metal ion that interacts with the doubly occupied σ-bonding orbital of H_2 (having a_1 symmetry) and a donor orbital on the metal ion (the in-plane π-like orbital) that interacts with the empty σ^*-antibonding orbital of H_2 (having b_2 symmetry). Thus, the $^2B_2(1a_1^22a_1^21b_2^1)$ surface is the most attractive and leads to a well that is 0.21 eV deep with respect to the Hf^+ and H_2 reactants (at $\angle$HHfH=20.5°). When the 5d electron of $Hf^+(^2D)$ lies in the orbitals having b_1 (the out-of-plane π-like orbital) or a_2 (δ-like, which should also be similar to the other δ-like orbital having a_1 symmetry), much more repulsive surfaces are formed, but still lead to an $Hf^+(H_2)$ adduct with wells lying 0.12 and 0.07 eV below the reactants for $^2B_1$ and $^2A_2$, respectively. If the 5d electron occupies the σ-like a_1 orbital, the surface that evolves is even more repulsive. Note that this $^2A_1$ surface should have an avoided crossing with the $^2A_1$ surface evolving from the upper ^2D state of Hf^+ near 20° (as indicated by the solid circle near 0.8 eV). As the bond lengths of these two species may differ (even though the bond angles are the same), this crossing point is only suggestive, but the true crossing point is likely to be nearby. Likewise along the $^2B_1$ and $^2A_2$ surfaces, there are avoided crossings near 1.7 eV above the reactants, still below the product asymptote. Figure 4 also includes several quartet surfaces but none of these forms a particularly stable H–Hf$^+$–H intermediate and are therefore unlikely to be important in the reactions of $Hf^+(^2D)$ with H_2.

It should be realized that C_{2v} symmetry will not occur in most reactive collisions, such that experimentally relevant surfaces will be reduced to C_s symmetry. Thus crossings between A_1 and B_2 surfaces (both A′) and between B_1 and A_2 surfaces (both A″) will be avoided, as indicated by the open circles in Fig. 4. (Again these crossing points are only suggestive because the true crossing points require equal bond lengths as well.) Thus, the attractive $^2B_2(1a_1^21b_2^12a_1^2)$ surface evolving from ground state $Hf^+(^2D)+H_2$ leads to a crossing at low energies (~0.3 eV) with the $^2A_1(1a_1^21b_2^22a_1^1)$ surface leading to ground state HfH_2^+.

We also considered a collinear interaction between Hf^+ and H_2. Initial approach of $Hf^+(^2D,6s^25d^1)$ to H_2 is attractive when the electron occupying the d orbital is in the $d\pi_{xz}$, $d\pi_{yz}$, $d\delta_{xy}$, or $d\delta_{x2-y2}$ orbital, as those orbitals do not mix with the σ orbitals of H_2. On the $^2\Pi$ surface, an Hf$^+$–H–H adduct is formed having a Hf–H bond length of 2.83 Å and an H–H bond length of 0.747 Å. On the $^2\Delta$ surface, the Hf$^+$–H–H adduct has a Hf–H bond length of 3.13 Å and a H–H bond length of 0.747 Å. Both of these surfaces have H–H bond lengths that are only slightly extended from that calculated for free H_2 of 0.743 Å. The $^2\Pi$ and $^2\Delta$ intermediates have minima lying 0.105 and 0.086 eV, respectively, below the reactant asymptote. When the d electron of $Hf^+(^2D,6s^25d^1)$ occupies the $d\sigma_{z2}$ orbital, there is a repulsive interaction with the doubly occupied σ_g orbital of H_2. From the $^2\Pi$ and $^2\Delta$ adducts, lengthening the H–H bond leads cleanly to $^3\Pi$ and $^3\Delta$ states of HfH$^+$ along with H(^{2}S), respectively.

V. DISCUSSION

A. Thermochemistry

The three group IV metal ions, Ti^+, Zr^+, and Hf^+, have MH^+ BDEs that are similar to one another: 2.31 ± 0.11, 2.26 ± 0.08, and 2.11 ± 0.08 eV, respectively.[16,19] This is unusual as third-row transition metals to the right of Hf have M^+–H BDEs that are 0.10–1.96 eV higher than their first or second-row congener. (In group III, YH$^+$ has a slightly higher bond energy than LaH$^+$.) Both Ti^+ and Zr^+ have ^4F ground states with s^1d^2 configurations and MH^+ ground states of $^3\Phi(\sigma_b^2\pi^1\delta^1)$. In the case of Hf^+, the ground state is ^2D with a s^2d^1 configuration that leads to a $^1\Sigma^+(\sigma_b^2\sigma^2)$, or possibly $^3\Delta(\sigma_b^2\sigma^1\delta^1)$, ground state for HfH$^+$. Thus, in contrast to the lighter congeners, the stability of the s orbital relative to the d orbitals leads to preferential occupation of the nonbonding σ orbital in HfH$^+$. Formation of the triplet states of MH^+ involves coupling the ^4F states of M^+ with H(^{1}S). Thus, Hf^+ needs to promote one electron in an s orbital into a d orbital to form the $^4F(6s^15d^2)$ excited state. To also include the effects of decoupling the 6s electron from the 5d electrons, we define the promotion energy as the average of the $^4F(6s^15d^2)$ and $^2F(6s^15d^2)$ excitation energies for Hf^+, yielding 1.250 eV. The ground states of Ti^+ and Zr^+ are already $^4F(s^1d^2)$ configurations, and the average of their ^4F and ^2F excitations are 0.310 and 0.429 eV, respectively. When we add these promotion energies to the BDEs of TiH$^+$, ZrH$^+$, and HfH$^+$, the resulting intrinsic M^+–H BDEs become 2.62, 2.69, and 3.36 eV, respectively. This comparison makes the relative MH^+ BDEs of the group IV metals comparable to the trends observed for other transition metal groups.

The $^1\Sigma^+$ state of HfH$^+$ is low in energy because it can be formed directly from the $^2D(6s^25d^1)$ state of Hf^+, thus avoiding promotion and exchange energy costs. However, this means that the covalent bond is formed by coupling the 1s electron of H with a 5d electron of Hf^+. As discussed previously by Ohanessian *et al.*,[32] third-row transition metal cations ordinarily form covalent bonds with H using sd hybrid orbitals because of the similar size of the 6s and 5d orbitals, with most species having bonding orbitals with 56%–75% d contributions (64% for the $^3\Delta$ state of Hf^+). Such hybridization is not possible for the $^1\Sigma^+$ state of HfH$^+$ because the 6s orbital on Hf^+ is already doubly occupied, such that the $^1\Sigma^+$ state has a relatively weak bond because of the poorer overlap of the 5$d\sigma$ orbital of Hf^+ and the 1s orbital of H.

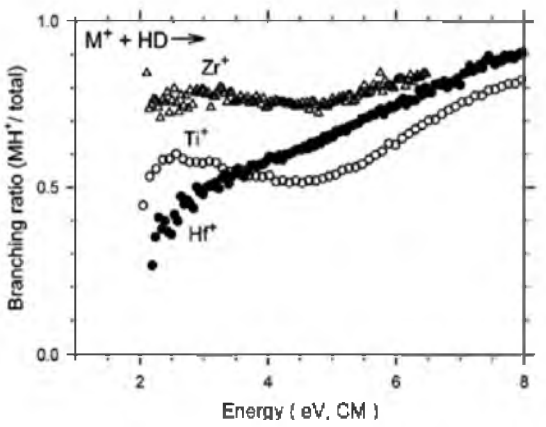

FIG. 5. Product branching fractions ($\sigma_{MH^+}/\sigma_{tot}$) for reactions of $Ti^+(^4F)$, Zr^+ (^4F), and Hf^+ (^2D) with HD as a function of kinetic energy.

B. Reaction mechanism

Further comparison of the group IV metal ions is facilitated by examining the reaction mechanisms as revealed by the reaction with HD. Previous work on the first-row and second-row transition metal cations indicates that the product branching ratio in the reaction of M^+ with HD is very sensitive to the reaction mechanism,[3,4,18,19,57] and is governed by three "rules." (1) If M^+ has an electron configuration with empty valence s and $d\sigma$ orbitals, such as for a d^n configuration where $n<5$, the reaction is efficient and may proceed by an insertion mechanism. These processes are characterized by product branching ratios in the HD system, ($\sigma_{MH^+}/\sigma_{tot}$) values that are near 0.5, consistent with statistical behavior of a long-lived intermediate. (2) If either the valence s or $d\sigma$ orbital is occupied and the M^+ state is low-spin, such as for d^n ($n>5$) or low-spin coupled $d^{n-1}s^1$ configurations, the reaction occurs efficiently via a direct mechanism. These processes are characterized by a product branching ratio in the HD system that favors MH^+ by a factor of 2–4, ($\sigma_{MH^+}/\sigma_{tot}$) ratios between 0.66 and 0.8, consistent with arguments concerning the conservation of angular momentum.[56,61,76–78] (3) If either the valence s or $d\sigma$ orbital is occupied and the M^+ state is high-spin (the highest spin it can possibly have), such as a high-spin coupled $d^{n-1}s^1$ configuration, the reaction is inefficient and tends to react impulsively. These processes are characterized by a product branching ratio in the HD system that favors MD^++H by a large factor, small values of the ($\sigma_{MH^+}/\sigma_{tot}$) ratio, and exhibit shifts in the thresholds for the H_2 and D_2 systems versus the HD system. Note that these rules are only appropriate for the diabatic reaction behavior, i.e., cases where the electron configuration of the metal ions remains essentially static throughout the course of the reaction.

Results for the reactions of Hf^+ are compared to those for the lighter congeners in Fig. 5 in terms of the fraction of metal hydride ion product formed. For the $^4F(s^1d^3)$ ground state configurations of both Ti^+ and Zr^+, one would expect reactions with dihydrogen according to category 3, an impulsive mechanism. For Ti^+, the data in Fig. 5 clearly indicate a statistical reaction (category 1), which was explained by the presence of a low-lying $^4F(d^3)$ state that is only 0.107 eV higher in energy.[16] This d^3 state is expected to react via a statistical mechanism and either mixes with or obscures the less reactive $Ti^+(^4F,4s^13d^2)$ ground state. For Zr^+, the data in Fig. 5 suggest reactivity between statistical and direct (category 2). This was explained by the coupling of the high-spin surfaces evolving from the ground state Zr^++H_2 reactants to those leading to the low-spin ZrH_2^+ intermediates, which would have a branching ratio that is consistent with a statistical mechanism.[19]

For $Hf^+(^2D,6s^25d^1)$, the branching ratio evolves more as a function of energy than those for Ti^+ and Zr^+. The data of Fig. 5 suggest largely statistical behavior in the region below the HD bond energy of 4.512 eV. This is consistent with the calculated PESs, which show that $Hf^+(^2D,6s^25d^1)$+H_2 reactants preferentially start off on the $^2B_2$ curve, which couples with the $^2A_1$ curve leading to a long-lived $^2A_1$ intermediate that is 1.08 eV below the reactant asymptote. This $^2A_1$ intermediate leads cleanly to the $HfH^+(^1\Sigma^+)$+H products. Other pathways couple to the $^2B_1$ and $^2A_2$ intermediates, which should also be long-lived and can form the $^3\Delta$ low-lying (or possibly ground) state.

For all three metal cations, the branching ratio above the dissociation energy of 4.5 eV increases, indicating that formation of MH^++D is favored increasingly over MD^++H. This trend is a consequence of the ability of the heavier D atom product to carry away more energy than the lighter H atom.[4,61–63]

ACKNOWLEDGMENTS

This work is supported by the National Science Foundation (Grant No. CHE-0748790).

[1] R. H. Crabtree, *The Organometallic Chemistry of the Transition Metals*, 2nd ed. (Wiley, New York, 1994).
[2] G. A. Somorjai, *Introduction to Surface Chemistry and Catalysis* (Wiley, New York, 1994).
[3] P. B. Armentrout, ACS Symp. Ser. **428**, 18 (1990).
[4] P. B. Armentrout, Int. Rev. Phys. Chem. **9**, 115 (1990).
[5] P. B. Armentrout and J. L. Beauchamp, Chem. Phys. **50**, 37 (1980).
[6] P. B. Armentrout and J. L. Beauchamp, J. Am. Chem. Soc. **103**, 784 (1981).
[7] P. B. Armentrout, L. F. Halle, and J. L. Beauchamp, J. Am. Chem. Soc. **103**, 962 (1981).
[8] P. B. Armentrout, L. F. Halle, and J. L. Beauchamp, J. Am. Chem. Soc. **103**, 6501 (1981).
[9] L. F. Halle, F. S. Klein, and J. Beauchamp, J. Am. Chem. Soc. **106**, 2543 (1984).
[10] M. L. Mandich, L. F. Halle, and J. L. Beauchamp, J. Am. Chem. Soc. **106**, 4403 (1984).
[11] M. A. Tolbert and J. L. Beauchamp, J. Am. Chem. Soc. **106**, 8117 (1984).
[12] J. L. Elkind and P. B. Armentrout, J. Chem. Phys. **84**, 4862 (1986).
[13] J. L. Elkind and P. B. Armentrout, J. Phys. Chem. **90**, 6576 (1986).
[14] J. L. Elkind and P. B. Armentrout, Inorg. Chem. **25**, 1078 (1986).
[15] J. L. Elkind and P. B. Armentrout, J. Phys. Chem. **91**, 2037 (1987).
[16] J. L. Elkind and P. B. Armentrout, Int. J. Mass Spectrom. Ion Process. **83**, 259 (1988).
[17] J. L. Elkind, L. S. Sunderlin, and P. B. Armentrout, J. Phys. Chem. **93**, 3151 (1989).
[18] Y.-M. Chen, J. L. Elkind, and P. B. Armentrout, J. Phys. Chem. **99**, 10438 (1995).
[19] M. R. Sievers, Y.-M. Chen, J. L. Elkind, and P. B. Armentrout, J. Phys. Chem. **100**, 54 (1996).
[20] X.-G. Zhang, C. Rue, S.-Y. Shin, and P. B. Armentrout, J. Chem. Phys.

116, 5574 (2002).
[21] X.-G. Zhang and P. B. Armentrout, J. Chem. Phys. **116**, 5565 (2002).
[22] F.-X. Li and P. B. Armentrout, J. Chem. Phys. **121**, 248 (2004).
[23] F.-X. Li, X.-G. Zhang, and P. B. Armentrout, J. Phys. Chem. B **109**, 8350 (2005).
[24] P. B. Armentrout, R. V. Hodges, and J. L. Beauchamp, J. Chem. Phys. **66**, 4683 (1977).
[25] P. B. Armentrout, R. V. Hodges, and J. L. Beauchamp, J. Am. Chem. Soc. **99**, 3162 (1977).
[26] P. B. Armentrout and J. L. Beauchamp, Chem. Phys. **48**, 315 (1980).
[27] R. Georgiadis and P. B. Armentrout, J. Phys. Chem. **92**, 7060 (1988).
[28] N. F. Dalleska, K. C. Crellin, and P. B. Armentrout, J. Phys. Chem. **97**, 3123 (1993).
[29] P. B. Armentrout and B. L. Kickel, in *Organometallic Ion Chemistry*, edited by B. S. Freiser (Kluwer, Dordrecht, 1996), p. 1.
[30] P. B. Armentrout, in *Topics in Organometallic Chemistry*, edited by J. M. Brown and P. Hofmann (Springer, Berlin, 1999), Vol. 4-I, p. 1.
[31] P. B. Armentrout, Int. J. Mass. Spectrom. **200**, 219 (2000).
[32] G. Ohanessian, M. J. Brusich, and W. A. Goddard III, J. Am. Chem. Soc. **112**, 7179 (1990).
[33] K. Balasubramanian and D. Dai, J. Chem. Phys. **93**, 7243 (1990).
[34] K. K. Das and K. Balasubramanian, J. Chem. Phys. **94**, 3722 (1991).
[35] D. Dai and K. Balasubramanian, J. Chem. Phys. **95**, 4284 (1991).
[36] D. Dai and K. Balasubramanian, Chem. Phys. Lett. **185**, 165 (1991).
[37] D. G. Dai, W. Cheng, and K. Balasubramanian, J. Chem. Phys. **95**, 9094 (1991).
[38] K. Balasubramanian and Z. Ma, J. Phys. Chem. **95**, 9794 (1991).
[39] H. Zhang and K. Balasubramanian, J. Phys. Chem. **96**, 6981 (1992).
[40] W. Z. Zhao, F. Buchinger, J. E. Crawford, S. Gulick, J. K. P. Lee, O. Constantinescu, M. Hussonnois, and J. Pinard, Spectrochim. Acta, Part B **51**, 707 (1996).
[41] L. G. Parke, C. S. Hinton, and P. B. Armentrout, Int. J. Mass. Spectrom. **254**, 168 (2006).
[42] S. K. Loh, D. A. Hales, L. Lian, and P. B. Armentrout, J. Chem. Phys. **90**, 5466 (1989).
[43] R. H. Schultz and P. B. Armentrout, Int. J. Mass Spectrom. Ion Process. **107**, 29 (1991).
[44] E. Teloy and D. Gerlich, Chem. Phys. **4**, 417 (1974).
[45] D. Gerlich, Adv. Chem. Phys. **82**, 1 (1992).
[46] N. R. Daly, Rev. Sci. Instrum. **31**, 264 (1960).
[47] K. M. Ervin and P. B. Armentrout, J. Chem. Phys. **83**, 166 (1985).
[48] P. J. Chantry, J. Chem. Phys. **55**, 2746 (1971).
[49] C. S. Hinton, F.-X. Li, and P. B. Armentrout, Int. J. Mass. Spectrom. **280**, 226 (2009).
[50] B. L. Kickel and P. B. Armentrout, J. Am. Chem. Soc. **117**, 4057 (1995).
[51] D. E. Clemmer, Y.-M. Chen, F. A. Khan, and P. B. Armentrout, J. Phys. Chem. **98**, 6522 (1994).
[52] C. L. Haynes and P. B. Armentrout, Organometallics **13**, 3480 (1994).
[53] B. L. Kickel and P. B. Armentrout, J. Am. Chem. Soc. **117**, 764 (1995).
[54] C. E. Moore, *Atomic Energy Levels as Derived from the Analyses of Optical Spectra*, Vol. III. NSRDS-NBS 35 (US Government Printing Office, Washington, DC, 1971).
[55] W. J. Chesnavich and M. T. Bowers, J. Phys. Chem. **83**, 900 (1979).
[56] N. Aristov and P. B. Armentrout, J. Am. Chem. Soc. **108**, 1806 (1986).
[57] P. B. Armentrout, in *Advances in Gas Phase Metal Ion Chemistry*, edited by N. G. Adams and L. M. Babcock (JAI, Greenwich, 1992), Vol. 1, p. 83.
[58] F. Muntean and P. B. Armentrout, J. Chem. Phys. **115**, 1213 (2001).
[59] M. E. Weber, J. L. Elkind, and P. B. Armentrout, J. Chem. Phys. **84**, 1521 (1986).
[60] K. P. Huber and G. Herzberg, *Molecular Spectra and Molecular Structure* (Van Nostrand Reinhold, New York, 1974), Vol. IV.
[61] J. L. Elkind and P. B. Armentrout, J. Phys. Chem. **89**, 5626 (1985).
[62] P. B. Armentrout, in *Gas Phase Inorganic Chemistry*, edited by D. H. Russell (Plenum, New York, 1989), p. 1.
[63] P. B. Armentrout, in *Selective Hydrocarbon Activation: Principles and Progress*, edited by J. A. Davies, P. L. Watson, A. Greenberg, and J. F. Liebman (VCH, New York, 1990), p. 467.
[64] A. D. Becke, J. Chem. Phys. **98**, 5648 (1993).
[65] C. Lee, W. Yang, and R. G. Parr, Phys. Rev. B **37**, 785 (1988).
[66] M. J. Frisch, G. W. Trucks, H. B. Schlegel *et al.*, GAUSSIAN 03, Revision B.02, Gaussian, Inc., Pittsburgh, PA, 2003.
[67] K. P. Huber and G. Herzberg, *Molecular Spectra and Molecular Structure* (Van Nostrand Reinhold, New York, 1979), Vol. IV.
[68] P. J. Hay and W. R. Wadt, J. Chem. Phys. **82**, 299 (1985).
[69] J. B. Foresman and Æ. Frisch, *Exploring Chemistry with Electronic Structure Methods*, 2nd ed. (Gaussian, Pittsburgh, 1996).
[70] F. Weigend and R. Ahlrichs, Phys. Chem. Chem. Phys. **7**, 3297 (2005).
[71] D. Andrae, U. Haeussermann, M. Dolg, H. Stoll, and H. Preuss, Theor. Chim. Acta **77**, 123 (1990).
[72] M. C. Holthausen, C. Heinemann, H. H. Cornehl, W. Koch, and H. Schwarz, J. Chem. Phys. **102**, 4931 (1995).
[73] M. C. Holthausen, M. Mohr, and W. Koch, Chem. Phys. Lett. **240**, 245 (1995).
[74] See supplementary material at http://dx.doi.org/10.1063/1.3482663 for one table of energies of various states of Hf^+ calculated at several levels of theory.
[75] E. R. Meyer, J. L. Bohn, and M. P. Deskevich, Phys. Rev. A **73**, 062108 (2006).
[76] L. S. Sunderlin, N. Aristov, and P. B. Armentrout, J. Am. Chem. Soc. **109**, 78 (1987).
[77] J. D. Burley, K. M. Ervin, and P. B. Armentrout, Int. J. Mass Spectrom. Ion Process. **80**, 153 (1987).
[78] P. B. Armentrout, ACS Symp. Ser. **502**, 194 (1992).

CHAPTER 4

GUIDED ION BEAM AND THEORETICAL STUDY OF THE REACTIONS OF Os^+ WITH H_2, D_2, AND HD

Christopher S. Hinton, Murat Citir, P. B. Armentrout

Reprinted from ***The Journal of Chemical Physics, Volume 135***, *Issue 23*
Christopher S. Hinton, Murat Citir, P. B. Armentrout, Guided Ion Beam and Theoretical Study of the Reactions of Os^+ with H_2, D_2, and HD, Pages 234302-234312, with permission from American Institute of Physics

Guided ion beam and theoretical study of the reactions of Os^+ with H_2, D_2, and HD

Christopher S. Hinton, Murat Citir, and P. B. Armentrout[a)]
Department of Chemistry, University of Utah, 315 South 1400 East, Room 2020, Salt Lake City, Utah 84112, USA

(Received 7 October 2011; accepted 22 November 2011; published online 16 December 2011)

Reactions of the third-row transition metal cation Os^+ with H_2, D_2, and HD to form OsH^+ (OsD^+) were studied using a guided ion beam tandem mass spectrometer. A flow tube ion source produces Os^+ in its ^6D ($6s^15d^6$) electronic ground state level. Corresponding state-specific reaction cross sections are obtained. The kinetic energy dependences of the cross sections for the endothermic formation of OsH^+ and OsD^+ are analyzed to give a 0 K bond dissociation energy of $D_0(Os^+–H) = 2.45 \pm 0.10$ eV. Quantum chemical calculations are performed here at several levels of theory, with B3LYP approaches generally overestimating the experimental bond energy whereas results obtained using BHLYP and CCSD(T), coupled-cluster with single, double, and perturbative triple excitations, levels show good agreement. Theory also provides the electronic structures of these species and the potential energy surfaces for reaction. Results from the reactions with HD provide insight into the reaction mechanism and indicate that Os^+ reacts via a direct reaction. We also compare this third-row transition metal system with the first-row and second-row congeners, Fe^+ and Ru^+, and find that Os^+ reacts more efficiently with dihydrogen, forming a stronger $M^+–H$ bond. These differences can be attributed to the lanthanide contraction and relativistic effects.
 [doi:10.1063/1.3669425]

I. INTRODUCTION

As one of the most reactive third-row transition metals, osmium complexes have been shown to be good catalysts for the activation of C–H and C–C bonds in solution, for the dehydrogenation of organic compounds,[1] and in the production of ammonia.[2] In order to gain an understanding into the properties of osmium in bond activation processes, it is useful to study the activation of dihydrogen in the gas-phase at a single metal center. This is one of the simplest reactions and therefore potentially among the most useful because it can be studied in detail both experimentally and theoretically. The periodic trends in such bond activation chemistry are particularly interesting,[3–5] and there are now numerous experimental studies of the reactions of the ions of atomic first-row transition metals,[6–11] second-row transition metals,[6,7,11–13] third-row transition metals,[11,14–19] and other metals[20–24] with dihydrogen, reaction (1), and its isotopic analogues.

$$M^+ + H_2 \rightarrow MH^+ + H. \qquad (1)$$

In addition to the kinetics and dynamics of this reaction, the guided ion beam tandem mass spectrometer (GIBMS) methods used in our laboratory can also measure the bond dissociation energy (BDE) of $M^+–H$ by analysis of the kinetic energy dependence of reaction (1).[25–27] Such thermochemistry is of obvious fundamental interest and has implications for understanding a variety of catalytic reactions involving transition metal systems.[28,29]

In an ongoing systematic study of reaction (1) for the third row transition-metal cations, we have previously studied La^+,[11] Hf^+,[18] Ta^+,[14] W^+,[14] Re^+,[16] Ir^+,[17] Pt^+,[15] Au^+,[19] and Lu^+ (Ref. 11) using GIBMS. Previous theoretical studies include all of the third-row transition-metal hydride cations.[30–38] We continue these studies here by reporting absolute cross sections as a function of kinetic energy for reactions of H_2, D_2, and HD with Os^+ and analyze them to acquire $D_0(Os^+–H)$. Detailed theoretical calculations on the OsH^+ and OsH_2^+ species were performed to assign electronic structures and explore possible mechanisms for these reactions. Experimental branching ratios for reaction with HD also provide mechanistic insight, which is compared with results for the lighter group 8 congeners, Fe^+ and Ru^+. There are currently no experimental results in the literature for OsH^+, although theoretical studies for both OsH^+ and OsH_2^+ have been published.[30,34,37]

II. EXPERIMENTAL

A. General

The guided ion beam tandem mass spectrometer on which these experiments were performed has been described in detail previously.[39] Briefly, atomic metal ions are generated in a direct current discharge flow tube (DC/FT) source described below,[40] extracted from the source, accelerated, and focused into a magnetic sector momentum analyzer for mass selection of primary ions. The mass-selected ions are decelerated to a desired kinetic energy and focused into an octopole ion beam guide that uses radio-frequency electric fields to trap the ions in the radial direction and ensure complete collec-

a)Author to whom correspondence should be addressed. Electronic mail: armentrout@chem.utah.edu.

tion of reactant and product ions.[41,42] The octopole passes through a static gas cell with an effective length of 8.26 cm that contains the reaction partner (here, H_2, D_2, or HD) at a low pressure (usually less than ~0.3 mTorr) so that multiple ion–molecule collisions are improbable. All products reported here result from single bimolecular encounters, as verified by pressure dependence studies. The unreacted parent and product ions are confined radially in the guide until they drift to the end of the octopole where they are extracted, focused, and passed through a quadrupole mass filter for mass analysis of products. Ions are subsequently detected with a secondary electron scintillation ion detector[43] using standard pulse counting techniques. Reaction cross sections are calculated from product ion intensities relative to reactant ion intensities after correcting for background signals.[44] Uncertainties in absolute cross sections are estimated to be ±20%.

The kinetic energy of the ions is varied in the laboratory frame by scanning the dc bias on the octopole rods with respect to the potential of the ion source region. Laboratory (lab) ion energies are converted to energies in the center-of-mass frame (CM) by using the formula $E_{CM} = E_{lab}\, m/(m + M)$, where m and M are the neutral and ionic reactant masses, respectively. Two effects broaden the cross section data: the kinetic energy distribution of the reactant ion and the thermal motion of the neutral reactant gas (Doppler broadening).[45] The absolute zero and the full width at half maximum (FWHM) of the kinetic energy distribution of the reactant ions are determined using the octopole beam guide as a retarding potential analyzer, as described previously.[44] The distributions of ion energies, which are independent of energy, are nearly Gaussian and have a typical FWHM of 0.4–0.9 eV (lab) in these studies. These values are somewhat larger than is usual for this instrument in part because of the extremely wide energy range needed in these studies (lab energies from 0 to 800 eV). This requires different focusing of the ion beam than is optimal for determining the zero of energy and energy distributions. Uncertainties in the absolute zero of the energy scale are ±0.1 eV (lab).

B. Ion source

Os^+ ions are produced in a DC/FT source,[40] consisting of a cathode held at a high negative voltage (1.2–1.6 kV) over which a flow of ~90% He and 10% Ar passes at a total pressure of 0.3–0.5 Torr. The dc-discharge ionizes Ar and then accelerates these ions into the cathode made of iron with a osmium/vanadium alloy disk attached to the cathode. As the ions are swept down the meter-long flow tube, they undergo ~10^5 thermalizing collisions with He and Ar. No evidence for low-lying excited states of the metal ions (such as cross section features having lower energy thresholds) within about 1% sensitivity is observed under these flow conditions in this work. When compared to a surface ionization source, the DC/FT source has been found to generate Sc^+,[46] Fe^+,[47] Co^+,[48] Ni^+,[49] Ru^+,[12] Rh^+,[12] and Pd^+ (Ref. 12) ions with an average electronic temperature of 700 ± 400 K, and Y^+, Zr^+, Nb^+, and Mo^+ ions with an average electronic temperature of 300 ± 100 K.[13] Therefore, M^+ ions created under such conditions are believed to be in the ground state electronic term, ^6D ($6s^15d^6$) for Os^+,[50,51] and largely in the lowest spin-orbit level (Table I). These estimated populations are consistent with the failure to observe any evidence for electronically excited Os^+ species in the present study and lead to a negligible uncertainty (<0.01 eV) in the electronic energy of the Os^+ reactant.

TABLE I. Electronic states of atomic osmium cations.

State	Configuration	J	Energy[a] (eV)	Population (%) 300 K	700 K	1100 K
^6D	$6s^15d^6$	9/2	0.000	100.0	99.931	98.901
		7/2	0.445	0.0	0.050	0.720
		5/2	0.487	0.0	0.019	0.348
		3/2	0.693	0.0	0.000	0.026
		1/2	0.823	0.0	0.000	0.003
^6S	$6s^25d^5$	5/2	0.978	0.0	0.000	0.002
^4D	$6s^15d^6$	average	1.475[b,c]	0.0	0.000	0.000
^4F	$5d^7$	average	1.648[b,d]	0.0	0.000	0.000

[a]From Ref. 50, except as noted.
[b]State assignments from Ref. 51.
[c]Average of spin-orbit levels, 7/2, 5/2, and 3/2 (1/2 missing).
[d]Average of spin-orbit levels, 7/2 and 5/2 (9/2 and 3/2 missing). If the next 9/2 (assigned to ^2G) and 3/2 (assigned to ^2P) levels are included, the value shifts to 1.824 eV.

C. Data analysis

The cross sections of endothermic reactions are modeled using Eq. (2),[25–27,52–55]

$$\sigma(E) = \sigma_0 \sum_i g_i (E + E_i + E_{rot} - E_0)^n / E. \qquad (2)$$

where σ_0 is an energy-independent scaling factor, E is the relative kinetic energy of the reactants, n is an adjustable parameter that characterizes the energy dependence of the process, E_{rot} is the rotational energy of the diatomic reactant ($= k_B T$ at 300 K = 0.026 eV), and E_0 is the 0 K threshold for reaction of electronic, vibrational, and rotational state reactants. The model involves an explicit sum of the contributions of individual electronic states of the Os^+ reactant, denoted by i, having energies E_i and populations g_i. Before comparison with the experimental data, Eq. (2) is convoluted with the kinetic energy distributions of the reactant ions and neutrals at 300 K.[44] The σ_0, n, and E_0 parameters are then optimized using a nonlinear least-squares analysis to give the best reproduction of the data. Error limits for E_0 are calculated from the range of threshold values for different data sets over a range of acceptable n values combined with the absolute uncertainty in the kinetic energy scale.

At energies above $D_0(H_2)$ and $D_0(D_2)$, OsH^+ and OsD^+ product ions can dissociate (see below). Our analyses include a model for this subsequent dissociation, as outlined in detail in Ref. 56. This high-energy model requires two parameters: E_D fixes the onset for OsH^+ (OsD^+) dissociation, and the exponent p determines the energy dependence, similar to n in Eq. (2). For the results shown below, E_D is fixed near the H_2 (D_2) bond energy and the optimum value of p was found to be 2.0.

III. EXPERIMENTAL RESULTS

A. Reactions with H_2 and D_2

Figure 1 shows cross sections as a function of kinetic energy for the bimolecular reactions of H_2 and D_2 with Os^+ produced in the DC/FT source. Reaction (1) and its deuterated analogue is the only processes observed. Results for the reaction $Os^+ + D_2$ are somewhat easier to acquire because the heavier isotope reduces mass overlap between the product ion and the much more intense primary ion, thereby allowing intensities of the product ion to be measured more accurately over a larger dynamic range. However, the same mass resolution conditions were used to collect data for the H_2, D_2, and HD systems here. The absolute magnitudes of the $Os^+ + H_2$ and $Os^+ + D_2$ reaction cross sections are well within the 20% experimental uncertainty of these absolute cross section measurements with energy dependences that are quite similar when plotted on the center-of-mass energy scale.

The cross sections for both the H_2 and D_2 reactions rise from apparent thresholds near 1.5 eV. (Features observed in Fig. 1(a) below this energy are artifacts of the corrections necessitated by the overlap between the intense primary ion and weak product ion signals.) Both cross sections reach maxima near the neutral reactant dissociation energies, $D_0(H_2) = 4.478$ eV and $D_0(D_2) = 4.556$ eV.[57] At higher energies, the OsH^+ (OsD^+) products can be formed with internal energies in excess of their bond dissociation energy, such that these products begin to dissociate in the overall reaction (3):

$$Os^+ + H_2(D_2) \rightarrow OsH^+(OsD^+) + H(D) \rightarrow Os^+ + 2H(D). \quad (3)$$

The observation that the experimental cross sections reach maxima very close to the H_2 (D_2) bond energies illustrates that these processes begin promptly at their thermodynamic threshold.

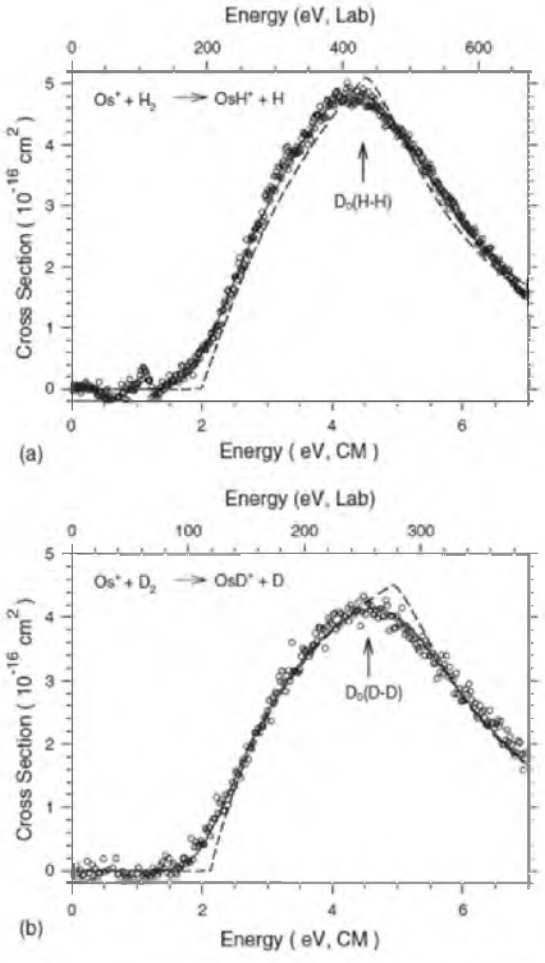

FIG. 1. Cross sections for the reaction of Os^+ (^6D) with H_2 (part a) and D_2 (part b) as a function of kinetic energy in the center-of-mass frame (lower axis) and laboratory frame (upper axis). The best fits to the data using Eq. (2) with parameters of Table II are shown as dashed lines. The solid lines show these models convoluted over the kinetic and internal energy distributions of the reactant neutral and ion. The arrows indicate D_0(H–H) at 4.478 eV and D_0(D–D) at 4.556 eV.

B. Reactions with HD

Os^+ reacts with HD to yield both OsH^+ and OsD^+ in reactions (4) and (5) as shown in Fig. 2,

$$Os^+ + HD \rightarrow OsH^+ + D, \quad (4)$$

$$\rightarrow OsD^+ + H. \quad (5)$$

Because of the close proximity of the product masses, there can easily be some overlap between these signals depending on the mass resolution used in the quadrupole mass filter. In the present system, it was carefully checked that high resolution leading to separation of these products could be used without sacrificing efficient collection of the product ions. The accuracy of the final results is confirmed by rea-

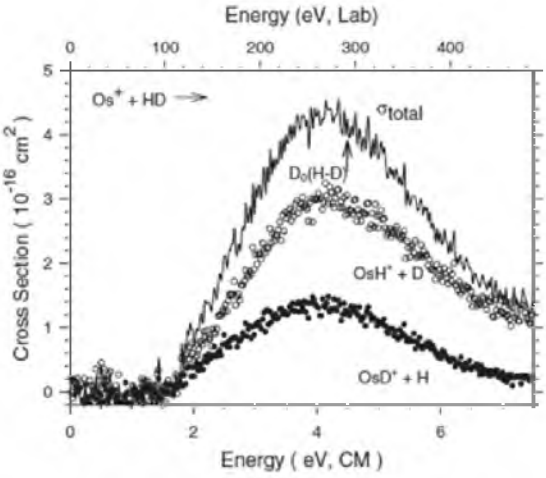

FIG. 2. Cross sections for the reaction of Os^+ (^6D) with HD as a function of kinetic energy in the center-of-mass frame (lower axis) and laboratory frame (upper axis). The arrow indicates D_0(H–D) at 4.514 eV.

sonable agreement (within the 20% absolute uncertainty) between the magnitudes of the total cross sections for the HD system and those of the H_2 and D_2 systems (Fig. 1).

The total cross section in the HD system exhibits endothermic behavior and rises from an apparent threshold that is similar to those of the H_2 and D_2 systems. The total cross section reaches a maximum near the bond dissociation energy of HD, 4.514 eV.[57] The individual OsH^+ and OsD^+ cross sections behave somewhat differently such that the OsD^+ cross section rises from a slightly earlier apparent onset and then peaks at a somewhat lower energy than that of OsH^+. This behavior can be rationalized because the $OsD^+ + H$ product channel has a lower energy threshold by the zero point energy difference of 0.039 eV (see below). The relative high-energy behavior shows that the more massive D atom carries away more energy from OsH^+ than the lighter H atom carries away from OsD^+. This effect is typical of atomic ion reactions with HD[7,12,13] and has been discussed in more detail in Refs. 4 and 58–60.

C. Thermochemical results

The endothermic cross sections in the H_2 and D_2 reaction systems are analyzed in detail using Eq. (2). Typical models are shown in Fig. 1 and can be seen to reproduce the experimental results very well throughout the energy range examined. The optimum values of the parameters in Eq. (2) for these systems are listed in Table II. As can be seen in Fig. 1, the optimum values of E_0 differ appreciably from the apparent thresholds, which is largely a result of the appreciable velocity distribution of the light H_2 (D_2) reactants. Because the convoluted form of Eq. (2) includes all sources of energy (rotational, vibrational, translational, and electronic energy distributions of reactants are explicitly included in the modeling), the E_0 threshold energies determined correspond to 0 K values. From the thresholds measured, the BDEs for the metal-ligand cations observed in reaction (1) can be calculated using Eq. (6),

$$D_0(Os^+\text{–H}) = D_0(H_2) - E_0, \tag{6}$$

and an analogous equation for the deuterated system. This equation assumes that there is no activation barrier in excess of the endothermicity of the reaction, an assumption that is often true for ion-molecule reactions because of the long-range attractive forces[54] and one that is confirmed using theory (see below). A summary of the Os^+–H bond energies derived from the present experiments with both H_2 and D_2 is given in Table II. This includes adjusting the value for $D_0(Os^+\text{–D})$ for the zero point energy difference between OsD^+ and OsH^+. This correction uses a vibrational frequency of 2174 cm^{-1} for OsH^+ (see below) and 1542 cm^{-1} for OsD^+, a value that agrees well with a 2244 cm^{-1} value calculated by Ohanessian *et al.* for OsH^+.[30] Thus the zero point energy differences in the OsH^+ and OsD^+ bond energies are 0.039 ± 0.004 eV, assuming a 10% uncertainty in the frequencies. The Os^+–H bond energies obtained from the H_2 and D_2 systems are in excellent agreement with one another (Table II). Our best value for this bond energy is the weighted average of these two values, 2.45 ± 0.10 eV, where the uncertainty is two standard deviations of the mean.

TABLE II. Parameters of Eq. (2) used in modeling reaction (1) and its deuterated analogue and the resultant bond energies.

Reactants	Products	σ_0	n	E_0 (eV)	$D_0(Os^+\text{–H})$ (eV)
$Os^+ + H_2$	$OsH^+ + H$	7.8 ± 0.4	1.0 ± 0.1	2.01 ± 0.08	2.47 ± 0.08
$Os^+ + D_2$	$OsD^+ + D$	8.5 ± 0.3	1.0 ± 0.1	2.09 ± 0.06	2.43 ± 0.06[a]

[a]Value corrected for the zero-point energy difference of 0.039 ± 0.004 eV. See text.

IV. THEORETICAL CALCULATIONS

A. General

Most quantum chemistry calculations reported here are computed using the B3LYP hybrid density functional method[61,62] and performed with the GAUSSIAN 09 suite of programs.[63] A large basis set is used for hydrogen, triple-ζ with diffuse and polarization functions, 6-311+G(3*p*), or def2-TZVPP, a balanced basis set of triple-ζ quality with polarization functions. Both basis sets give good results for the thermochemistry of dihydrogen, with deviations from experiment of less than 0.03 eV for the bond energy of H–H (4.505 eV and 4.507 eV for calculations with 6-311+G(3*p*) and def2-TZVPP, respectively, versus 4.478 eV experimental).[57] For osmium, three basis sets were considered, all using effective core potentials (ECPs) that are small core (60 electrons) in which the 5*s*, 5*p*, 5*d*, and 6*s* orbitals are retained in the valence space. Both the def2-TZVPP and Stuttgart-Dresden (SDD) approaches use ECPs developed by Andrae *et al.*,[64] whereas the HW+ basis set uses that of Hay-Wadt (HW).[65] The def2-TZVPP basis set, which is used for most calculations here, includes *f* and *g* type polarization functions on Os,[66] with contraction scheme (8*s*7*p*6*d*2*f*1*g*)/[6*s*4*p*3*d*2*f*1*g*], whereas neither the HW+ nor the SDD basis sets do. (The def2-TZVPP basis set was obtained from the basis set exchange of the Environmental and Molecular Sciences Laboratory, EMSL.[67]) The HW+ basis set has been developed by Ohanessian *et al.*[30] and accounts for the differential contraction of the *s* orbitals compared to the *d* orbitals resulting from the positive charge. We also examined results calculated using the SDD basis set of Dolg *et al.*[68] for Os, retaining the 6-311+G(3*p*) basis on hydrogen. In all cases, the thermochemistry calculated and cited here is corrected for zero point energy effects, after scaling the frequencies by 0.9804.[69]

Holthausen *et al.*[70] carefully considered the most appropriate choice for a level of theory for the first and third row transition metal methyl cations, species analogous to the metal hydride cations considered here, because both have single covalent metal-ligand bonds. These authors used B3LYP, Becke-half-and-half-LYP (BHLYP), and QCISD(T), quadratic configuration interaction with single, double, and perturbative triple excitations, methods with a basis set consisting of a polarized double-ζ on C and H and the Hay-Wadt relativistic ECP with valence electrons added. The symmetries of the metal methyl species were constrained to C_{3v}. Upon comparison with experimental results for the first row

MCH_3^+ species (M = Sc–Cu),[25,26] these authors conclude that the B3LYP functional overbinds, whereas the BHLYP functional and the QCISD(T) methods perform more accurately. Mean absolute deviations (MADs) from experiment were 0.41, 0.18, and 0.20 eV, respectively. Likewise, the bond energies calculated using B3LYP were higher than those for BHLYP and QCISD(T) for the third row metal methyl cations. Given these results, we also performed geometry optimizations and single point energy calculations for the OsH^+ species using the BHLYP functional and CCSD(T), coupled-cluster with single, double, and perturbative triple excitations, levels of theory with the HW+, def2-TZVPP, and SDD basis sets for Os^+. Such calculations will be explicitly noted and unless otherwise designated, our results will refer to a B3LYP/def2-TZVPP/6-311+G(3*p*) level of theory. For OsH_2^+ species where multiple bonds to Os^+ are formed, only the B3LYP functional is used, unless otherwise noted. This choice is rationalized on the basis of the results of Holthausen *et al.*[71] for metal-methylene cations and our own studies of MCH_x^+ ($x = 0$–2) species.[72–78]

One means of evaluating the level of theory and basis set used in the calculations is to compare electronic excitation energies of Os^+ with those from experiment, Table III. Experimental values for the excitation energies (average over all spin-orbit states) from the ^6D ($6s^15d^6$) ground state to the ^6S ($6s^25d^5$), ^4D ($6s^15d^6$), and $^4F(5d^7)$ excited states are 0.615, 1.112, and 1.285 eV, respectively. At the B3LYP and BHLYP levels of theory using all three basis sets, all excitation energies are high with the exception of the ^6S excitation using the HW+ basis set. For the excitation energies calculated using CCSD(T), results with the def2-TZVPP basis set give good agreement (within about 0.2 eV) of the experimental values. The results from the SDD basis set are much worse with the ^4D state being predicted as the ground state. For the HW+ basis set, the calculated energies vary considerably, being as much as 0.7 eV high and 0.5 eV low. As noted by a reviewer, the lack of *f*- and *g*-polarization functions means that the HW+ and SDD basis sets are insufficient for a meaningful recovery of electron correlation at the CCSD(T) level. Overall, the CCSD(T)/def2-TZVPP calculations perform the best.

TABLE III. Calculated excitation energies for the atomic osmium ion.

State	Basis set	B3LYP	BHLYP	CCSD(T)	Expt.[a]
$^6D(6s^15d^6)$	def2-TZVPP	0.0	0.0	0.0	0.000
	SDD	0.0	0.0	0.412	
	HW+	0.0	0.0	0.0	
$^6S(6s^25d^5)$	def2-TZVPP	1.008	0.972	0.811	0.615
	SDD	1.049	1.008	0.689	
	HW+	0.699	0.605	0.114	
$^4D(6s^15d^6)$	def2-TZVPP	1.437	1.516	0.920	1.112
	SDD	1.502	1.627	0.0	
	HW+	1.481	1.599	1.868	
$^4F(5d^7)$	def2-TZVPP	1.504	1.584	1.210	1.285
	SDD	1.529	1.596	1.905	
	HW+	1.838	1.951	1.405	
$^2D(6s^15d^6)$	def2-TZVPP	2.716	2.822	2.943	
	SDD	2.739	2.889	2.985	
	HW+	2.684	2.830	2.060	

[a]Statistically weighted mean of spin-orbit levels. Referenced to the ground term, 0.363 eV for Os^+ (^6D). See Table I for references.

The experimental BDEs refer to the ground spin-orbit state at 0.0 eV, $^6D_{9/2}$ for Os^+. In contrast, our calculations are referenced to the statistically weighted mean of all spin-orbit levels in the ground term, 0.363 eV for Os^+ (^6D).[50] Because our calculations do not explicitly include spin-orbit interactions, it is possible that all calculated energetics may need to be corrected by this different asymptotic energy before comparison with experimental values. However, spin-orbit effects also influence the energetics of the intermediates and products in reaction (1). Indeed, previous work done by Balasubramanian and co-workers have found that spin-orbit effects for OsH and OsH_2^+ can be large,[34,79] up to 0.80 eV for the highly excited $^6\Pi$ state of OsH, but are much smaller, 0.06–0.20 eV, for all other OsH states and about 0.1 eV for OsH_2^+ states. As the magnitude of the spin-orbit effects are unknown for OsH^+, we do not apply corrections in the present work, implicitly assuming that the spin-orbit corrections largely cancel. On the basis of the spin-orbit effects observed by Balasubramanian, this assumption could introduce errors of a couple of tenths of an electron volt in the calculated energetics.

B. OsH^+ states

The ground state of OsH^+ has been previously calculated by Ohanessian *et al.* to be a $^5\Pi$ state where the character of the bonding orbital on Os is 43% 6*s* and 56% 5*d*.[30] The resultant bonding can be thought of as originating from a covalent sigma bond (σ_b^2) between the 1*s* orbital on H and a 6*s*5*d* hybrid orbital on Os^+ (^6D, $6s^15d^6$). This type of hybridization is quite efficient in the third-row transition metals because relativistic effects make the 6*s* orbital comparable in size to the 5*d* orbitals.[30,80] This 6*s*5*d* hybrid bonding orbital overlaps better with the 1*s* orbital on H(^2S) than pure 6*s* or 5*d* orbitals. The occupied nonbonding orbitals in the $^5\Pi$ state are $1\pi^3 1\delta^2 2\sigma^1$, where the 2σ orbital is the other 6*s*5*d* hybrid, and the 1π and 1δ orbitals are pure 5*d*. The bond length calculated by Ohanessian *et al.* is 1.605 Å,[30] which is nearly identical to the bond length of 1.601 Å calculated here at the B3LYP/def2-TZVPP/6-311+G(3*p*) level, Table IV.

A low-lying excited state of OsH^+ is the $^5\Delta$ ($1\sigma_b^2 1\pi^2 1\delta^3 2\sigma^1$) state, which Ohanessian calculated to be 0.33 eV higher than the $^5\Pi$ ground. Our calculations find the $^5\Delta$ state lies between 0.16 –and 0.29 eV above the $^5\Pi$ ground state at the various levels of theory (where the range comes from using all three basis sets for Os noted above). We also calculated results for other stable excited states at the B3LYP/def2-TZVPP/6-311+G(3*p*) level with relative energies listed in Table IV. Ohanessian *et al.* examined additional quintet and triplet excited states (but no singlet states) finding the $^5\Sigma^+$, $^3\Pi$, $^3\Phi$, and $^3\Sigma^-$. These all have bond lengths and excitation energies comparable to the present calculations (Table IV), with the exception of the $^3\Pi$ and $^3\Phi$ states in which the excitation energies listed here are 0.8 and 0.5 eV, respectively, lower than those calculated by Ohanessian *et al.*[30] The lower excitation found here for the $^3\Pi$ state can be attributed to spin contamination, whereas there is no obvious

TABLE IV. Theoretical geometries, energies, and vibrational frequencies for OsH^+.

		This work[a]				Literature[b]		
State	Configuration	$\langle S^2 \rangle$	r(Os-H) (Å)	E_{rel} (eV)[c]	frequency (cm^{-1})[d]	r(Os-H) (Å)	E_{rel} (eV)[c]	frequency (cm^{-1})
$^5\Pi$	$1\sigma_b^2 1\pi^3 1\delta^2 2\sigma^1$	6.01	1.601	0.00	2174	1.605	0.00	2244
$^5\Delta$	$1\sigma_b^2 1\pi^2 1\delta^3 2\sigma^1$	6.01	1.627	0.18	2098	1.638	0.33	2182
$^5\Sigma^+$	$1\sigma_b^2 1\pi^2 1\delta^2 2\sigma^2$	6.02	1.645	0.49	2026	1.640	0.45	2111
$^3\Pi$	$1\sigma_b^2 1\pi^3 1\delta^3$	2.86[e]	1.592	0.73	2229	1.602	1.52	2301
$^3\Phi$	$1\sigma_b^2 1\pi^3 1\delta^3$	2.01	1.591	1.17	2241	1.602	1.69	2261
$^3\Sigma^+$	$1\sigma_b^2 1\pi^4 1\delta^2$	2.02	1.573	1.37	2276			
$^3\Sigma^-$	$1\sigma_b^2 1\pi^2 1\delta^4$	2.01	1.610	1.83	2203	1.597	1.75	2211
$^1\Pi$	$1\sigma_b^2 1\pi^3 1\delta^2 2\sigma^1$	(1.00)[f]	1.594	2.14	2209			
$^3\Delta$	$1\sigma_b^2 1\pi^4 1\delta^1 2\sigma^1$	2.00	1.572	2.27	2258			
$^1\Sigma^+$	$1\sigma_b^2 1\pi^4 1\delta^2$	0.00	1.572	2.35	2284			
$^3\Sigma^-$	$1\sigma_b^2 1\pi^2 1\delta^2 2\sigma^2$	2.01	1.644	2.35	2039			
$^1\Delta$	$1\sigma_b^2 1\pi^2 1\delta^3 2\sigma^1$	0.00	1.631	2.51	2096			

[a]Calculations performed using B3LYP/def2-TZVPP/6-311+G(3*p*).
[b]GVB calculations of Ohanessian *et al.* (Ref. 30).
[c]Energies relative to the ground state including zero point energies.
[d]Vibrational frequencies scaled by 0.9804.
[e]State suffers from spin contamination.
[f]A reviewer suggests that this result may correspond to a broken-symmetry wavefunction in which the single determinant approach does not provide meaningful results.

reason for the lower value of the $^3\Phi$ state. We located several additional triplet and singlet states, $^3\Sigma^+$, $^3\Pi$, $^3\Delta$, $^1\Sigma^+$, $^3\Sigma^-$, and $^1\Delta$ with excitation energies between 1.37 and 2.51 eV, Table IV.

Ohanessian *et al.* calculated a BDE for the $^5\Pi$ state of OsH^+ of 2.44 eV using generalized valence bond theory (GVB), a value that is in excellent agreement with our experimental BDE of 2.45 ± 0.10 eV. In another study, Leininger *et al.* calculated the BDE of the $OsH^+(^5\Pi)$ state using restricted Hartree-Fock multireference configuration interaction (RHF-MRCI) and multiconfiguration Hartree-Fock single and double configuration (MCHF-SDCI) levels of theory along with both small and large ECPs from Hay-Wadt, Christiansen and co-workers, and Stoll, Preuss, and co-workers.[57] For these various levels of theory and large core ECPs, their calculated 0 K BDEs had a range of 2.16–3.01 eV, whereas with small core ECPs, the 0 K BDEs had a range of 2.25–2.47 eV. The latter agree reasonably well with our experimental results.

At the B3LYP level, we calculate the BDE to be 2.87–2.92 eV using the various basis sets mentioned above, Table V. These results are ~0.4 eV higher than the experimental BDE. The BDE calculated at the BHLYP level of theory is also high, but only by ~0.20 eV, with values ranging from 2.60 to 2.64 eV. Thus, as found by Holthausen *et al.*,[71] the B3LYP overbinds by several tenths of an electron volt, whereas the BHLYP provides more accurate BDEs compared to experiment for this singly bonded metal-ligand species. The values calculated at the CCSD(T) level provide similar agreement with experiment with values ranging from 2.53–2.76 eV to 0.1–0.3 eV higher than the experimental value. Remembering that the spin-orbit correction for Os^+ is 0.36 eV and those for OsH were about 0.13 ± 0.1 eV,[79] it is not unreasonable that the neglect of spin-orbit effects leads theory to overestimate the experimental bond energy by 0.2 ± 0.1 eV.

TABLE V. Comparison of experimental and theoretical bond energies (in eV) for OsH^+ ($^5\Pi$).

Basis set (Os/H)	B3LYP	BHLYP	CCSD(T)	Experimental
def2-TZVPP/def2-TZVPP	2.91	2.63	2.76	2.45 ± 0.10
def2-TZVPP/6-311+G(3*p*)	2.90	2.63	2.58	
HW+/6-311+G(3*p*)	2.92	2.64	2.60	
SDD/6-311+G(3*p*)	2.87	2.60	2.53	

C. OsH_2^+ states

To explore coarse features of the potential energy surfaces of reaction (1), we also calculated the properties of stable OsH_2^+ complexes, Table VI. Our results can be compared directly with those of Dai and Balasubramanian (DB), who calculated potential energy surfaces for the interaction of several spin states of Os^+ with H_2 at the complete active space multi-configuration self-consistent field (CASMCSCF) level, and then conducted single point calculations on the stationary points at a multireference single and double configuration interaction (MRSDCI) level. Results of the latter calculations are referred to below. As with the present work, these calculations use a relativistic small core (60 electrons) effective core potential on Os. In all of these calculations (ours and those of BD), these calculations were restricted to C_{2v} symmetry.

For OsH_2^+, our B3LYP/def2-TZVPP/6-311+G(3*p*) calculations find an inserted $^4B_2$ ground state with an energy of 1.28 eV below the $Os^+(^6D) + H_2$ asymptote. This state has a valence electron configuration of $(1a_1)^2(1b_2)^2(1b_1)^1(1a_2)^1(2a_1)^2(3a_1)^1$, where the $1a_1$ and $1b_2$ orbitals are Os–H bonding orbitals, the $1b_1$, $1a_2$, and $2a_1$ are pure *5d* nonbonding orbitals on Os, and the $3a_1$ is largely the $5d_{z^2}$ with some 6*s* character (where the symmetry axis is z and the molecule lies in the xz plane). In other states, the $2b_2$ and $4a_1$ orbitals, which are π antibonding and largely 6*s* in charac-

TABLE VI. Theoretical geometries and energies for OsH_2^+ calculated at the B3LYP/def2-TZVPP/6-311+G(3p) level of theory.

		This study[a]					Literature[b]		
State	Configuration	$\langle S^2\rangle$	r(Os–H) (Å)	∠HOsH (deg)	E_{rel}[c] (eV)	Frequency (cm^{-1})[d]	r(Os–H) (Å)	∠HOsH (deg)	E_{rel} (eV)
$^4B_2$	$(1a_1)^2(1b_2)^2(1b_1)^1(1a_2)^1(2a_1)^2(3a_1)^1$	3.77	1.588	88.6	0.00	721, 2182, 2208	1.583	87.4	0.00
$^4A_2$	$(1a_1)^2(1b_2)^2(1b_1)^2(1a_2)^1(2a_1)^1(3a_1)^1$	3.76	1.588	58.2	0.02	543, 2172, 2184	1.577	55.6	0.08
$^4B_1$	$(1a_1)^2(1b_2)^2(1b_1)^1(1a_2)^2(2a_1)^1(3a_1)^1$	3.77	1.603	96.7	0.13	324, 1965, 2164	1.599	101.8	0.28
$^2A_2$	$(1a_1)^2(1b_2)^2(1b_1)^2(1a_2)^1(2a_1)^2$	1.66[e]	1.583	61.0	0.59	589, 2203, 2218			
$^2B_1$	$(1a_1)^2(1b_2)^2(1b_1)^1(1a_2)^2(2a_1)^2$	1.64[e]	1.593	102.7	0.69	540, 2157, 2198	1.583	111.7	1.50
$^2B_2$	$(1a_1)^2(1b_2)^2(1b_1)^1(1a_2)^1(2a_1)^2(3a_1)^1$	1.75[e]	1.590	90.3	0.77	665, 2160, 2208	1.582	86.4	1.72
$^2A_2$	$(1a_1)^2(1b_2)^2(1b_1)^2(1a_2)^1(2a_1)^1(3a_1)^1$	1.75[e]	1.586	57.3	0.89	488, 1991, 2196	1.569	60.7	1.38
		1.75[e]	1.602	95.5	0.95	269, 1879, 2180	1.585	97.1	1.53
$^6B_2$	$(1a_1)^2(1b_2)^2(1b_1)^1(1a_2)^1(2a_1)^1(3a_1)^1(4a_1)^1$	8.75	2.409	18.2	1.06	309, 386, 4046			
$^6A_1$	$(1a_1)^2(1b_2)^1(1b_1)^1(1a_2)^1(2a_1)^2(3a_1)^1(4a_1)^1$	8.75	2.578	16.9	1.09	336, 344, 4140			
$^6A_2$	$(1a_1)^2(1b_2)^1(1b_1)^1(1a_2)^2(2a_1)^1(3a_1)^1(4a_1)^1$	8.75	2.579	16.9	1.09	340, 341, 4140			
$^6B_1$	$(1a_1)^2(1b_2)^1(1b_1)^2(1a_2)^1(2a_1)^1(3a_1)^1(4a_1)^1$	8.75	2.557	17.0	1.10	262, 334, 4153			
$^2A_1$	$(1a_1)^2(1b_2)^2(1b_1)^2(1a_2)^2(2a_1)^1$	0.75	1.578	67.6	1.12	573, 2232, 2248	1.567	65.2	1.26
$^6A_1$	$(1a_1)^2(1b_2)^2(1b_1)^1(1a_2)^1(2a_1)^1(3a_1)^1(2b_2)^1$	8.75	1.696	142.5	1.49	841, 1734, 1935	1.680	142.8	0.77
$^2A_1$	$(1a_1)^2(1b_2)^2(1b_1)^2(2a_1)^2(3a_1)^1$	0.75	1.579	62.9	1.54	690, 2200, 2222			
$^2B_1$	$(1a_1)^2(1b_2)^2(1b_1)^1(2a_1)^2(3a_1)^2$	0.75	1.696	75.7	1.77	716, 2079, 2189	1.580	73.4	1.48
$^2A_2$	$(1a_1)^2(1b_2)^2(1a_2)^1(2a_1)^2(3a_1)^2$	0.75	1.602	96.7	1.83	796, 1932, 2173			
$^4A_1$	$(1a_1)^2(1b_2)^2(1b_1)^1(1a_2)^1(2a_1)^2(2b_2)^1$	4.59[e]	1.692	145.5	2.38	905, 1775, 1941			
$^4A_1$	$(1a_1)^2(1b_2)^2(1a_2)^2(2a_1)^1(3a_1)^1(4a_1)^1$	3.75	2.359	18.7	3.61	840, 1786, 1968			
$^6\Delta_u$	$(1\sigma_g)^2(1\sigma_u)^1(2\sigma_g)^1(1\pi_g)^2(1\delta_g)^2$	8.75	1.776	180.0	2.51	−165 (2), 1679, 1859	1.829	180.0	3.01
$^6\Sigma_g^+$	$(1\sigma_g)^2(1\sigma_u)^2(2\sigma_g)^1(1\pi_g)^2(1\delta_g)^2$	8.76	1.743	180.0	2.93	1955, 2036, 2303 (2)	1.727	180.0	1.31
$^4\Phi_u$	$(1\sigma_g)^2(1\sigma_u)^1(1\pi_g)^3(1\delta_g)^3$	4.63[e]	1.748	180.0	2.99	−2506, 816, 876, 1684			
$^2\Pi_u$	$(1\sigma_g)^2(1\sigma_u)^1(2\sigma_g)^1(1\pi_g)^3(1\delta_g)^2$	1.78[e]	1.768	180.0	4.14	−1202, −1015, 669, 1614	1.759	180.0	3.79
$^4\Delta_u$	$(1\sigma_g)^2(1\sigma_u)^1(2\sigma_g)^1(1\pi_g)^2(1\delta_g)^3$	3.76	1.790	180.0	4.22	−2249, −1271, 803, 1603	1.770	180.0	2.61
$^2\Delta_u$	$(1\sigma_g)^2(1\sigma_u)^1(2\sigma_g)^1(1\pi_g)^2(1\delta_g)^3$	1.78[e]	1.792	180.0	4.55	−1614, −994, 563, 1600	1.797	180.0	4.27
$^2\Sigma_u^+$	$(1\sigma_g)^2(1\sigma_u)^1(1\pi_g)^3(1\delta_g)^4$	1.61[e]	1.785	180.0	4.73	−1703, −1284, 464, 1577	1.810	180.0	3.98
$^2\Sigma_u^+$	$(1\sigma_g)^2(1\sigma_u)^1(2\sigma_g)^2(1\pi_g)^2(1\delta_g)^2$	0.77	1.799	180.0	6.14	−2136, −979, 781, 1615			

[a]Calculations using B3LYP/def2-TZVPP/6-311+G(3p).
[b]MRSDCI values from Dai and Balasubramanian (Ref. 34).
[c]Energies relative to the ground state including zero point energies.
[d]Vibrational frequencies scaled by 0.9804.
[e]State suffers from spin contamination

ter, respectively, are also occupied. DB also find that the $^4B_2$ is the lowest state for OsH_2^+, with an energy below the $Os^+(^6D)$ + H_2 asymptote by 0.74 eV. The excitation energies for various doublet, quartet, and sextet states of OsH_2^+ are given in Table VI. The geometries (bond lengths and angles) in the present B3LYP calculations are comparable to those of DB in all cases, with MADs for bond lengths of 0.038 ± 0.036 Å and for bond angles of 3.8° ± 2.6° for the ground and nine excited states. The MRSDCI excitation energies determined by DB for all nine excited states differ from those calculated here by a MAD of 0.50 ± 0.24 eV.

The covalently bound dihydrides have Os^+–H bond lengths between 1.6 and 1.7 Å and bond angles of 58°–143° (Table VI). We also identified several sextet states corresponding to intact dihydrogen molecules weakly bound to Os^+. These states are identified by long Os^+–H bond lengths, 2.4–2.6 Å, and by small ∠H Os H bond angles, 17°–18°. There is also a $^4A_1$ state with a similar geometry, having an Os^+–H bond length of 2.359 Å and ∠H Os H bond angle of 18.7°. Additionally, several linear structures of OsH_2^+ were located, Table VI, although most are transition states between the more stable bent structures (as indicated by imaginary bending frequencies). These species have bond lengths between 1.7 and 1.8 Å, comparable to those calculated by DB. The excitation energies are also comparable to those of DB, with the exception of two states, $^6\Sigma^+$ and $^4\Delta$, that are higher for unknown reasons.

D. OsH_2^+ reaction surfaces

The complete surfaces for the various OsH_2^+ states as a function of bond angle are shown in Fig. 3. These were obtained from relaxed PES scan calculations starting at the optimized geometry of each state. The character of these surfaces is generally comparable to those found by DB, although as noted above, the energies of the surfaces relative to the $Os^+(^6D)$ + H_2 asymptote are lower here. In Fig. 3, the low-lying quartet states of OsH_2^+ ($^4B_2$, $^4A_2$, and $^4B_1$) lead diabatically to the $Os^+(^4D, 6s^15d^6)$ + H_2 reactant asymptote lying 1.44 eV (1.11 eV experimental) above the ground state. Os^+ (^6D, $6s^15d^6$) interacts with H_2 in C_{2v} symmetry to form four surfaces having $^6A_1$, $^6A_2$, $^6B_1$, and $^6B_2$ symmetries (a second $^6A_1$ surface must also exist but only one was located computationally). Of these, the $^6B_2$ ($1a_1^21b_2^21b_1^11a_2^12a_1^13a_1^14a_1^1$)

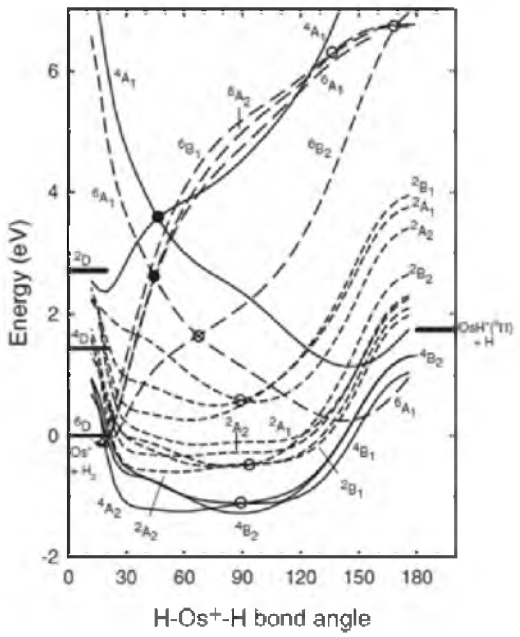

FIG. 3. B3LYP/def2-TZVPP/6-311+G(3*p*) calculations of the potential energy surfaces for the interaction of Os^+ with H_2 in C_{2v} symmetry as a function of the H-Os^+-H bond angle in degrees. Circles indicate avoided crossings in C_{2v} (filled) and C_s (open) symmetry.

is the most attractive surface and leads to a well that is 0.22 eV deep with respect to the $Os^+ + H_2$ reactants (at ∠HOsH = 18.2°). The other three states lead to similar surfaces, with $Os^+(H_2)$ adducts having wells lying between 0.18 and 0.19 eV below the reactant asymptote. There are also a set of doublet surfaces ($^2A_1$, $^2A_2$, $^2B_1$, and $^2B_2$) that form stable intermediates. These states originate from a ^2D ($6s^15d^6$) state of Os^+ that lies 2.716 eV (compared to 2.728 eV calculated by DB) above the ^6D state. These surfaces have potential wells that are 0.33–0.69 eV below the Os^+ (^6D) + H_2 reactant asymptote and 0.59–0.95 eV above the quartet surfaces.

It should be realized that C_{2v} symmetry will not occur in most reactive collisions, such that experimentally relevant surfaces will be reduced to C_s symmetry. Thus crossings between A_1 and B_2 surfaces (both A′) and between B_1 and A_2 (both A″) will be avoided, as indicated by the open circles in Fig. 3. These crossing points are only suggestive because the true crossing points require equal bond lengths as well.

We also considered a collinear interaction between Os^+ and H_2. Qualitatively, this may be reasonable as the single 6*s* electron on Os^+ (^6D) makes it similar to H (^2S), which is known to react most efficiently with H_2 along a collinear $C_{\infty v}$, rather than a perpendicular C_{2v} path. Indeed, we find that the collinear geometry is a viable reaction pathway. On the $^6\Pi$ surface, an Os^+-H-H adduct is formed having an Os–H bond length of 2.256 Å and an H–H bond length of 0.758 Å. On the $^6\Delta$ surface, the Os^+–H–H adduct has bond lengths of 2.328 and 0.756 Å, respectively. Both of the surfaces have H–H bond lengths that are only slightly extended from that calculated for free H_2 (0.743 Å). The $^6\Pi$ and $^6\Delta$ states have minima lying 0.11 and 0.10 eV, respectively, below the reactant asymptote. From the $^6\Pi$ and $^6\Delta$ adducts, lengthening the H–H bond leads cleanly to the $^5\Pi$ and $^5\Delta$ states of OsH^+ along with H(^2S) with no barriers, respectively.

Because of the C_{2v} symmetry restrictions, the PESs in Fig. 3 and those of DB cannot examine the $OsH^+ + H$ dissociation asymptote. It seems likely that these products can be formed from the OsH_2^+ intermediates with no barriers in excess of the endothermicity for the following reasons. The $^5\Pi$ ground state of OsH^+ can react with H(^2S) to form both high-spin sextet and low-spin quartet states of OsH_2^+. Formation of the high-spin states would be largely repulsive as no covalent bond formation is involved, but along the quartet surfaces, covalent coupling of a nonbonding OsH^+($^5\Pi$) electron with H occurs, such that the surface should be strongly attractive. To verify this hypothesis, we performed relaxed potential energy scans at the B3LYP/def2-TZVPP/6-311+G(3*p*) level starting with the bound OsH_2^+ ($^4B_2$) species and systematically lengthening one of the Os–H bonds along a $^4A'$ surface. This surface leads directly to OsH^+ ($^5\Pi$) + H (^2S) with no barriers in excess of the endothermicity.

V. DISCUSSION

A. Thermochemistry

The three group 8 metal ions, Fe^+, Ru^+, and Os^+, have MH^+ BDEs that are 2.12 ± 0.06, 1.62 ± 0.05, and 2.45 ± 0.10 eV, respectively.[7,12] The stronger BDE for osmium, and to a lesser extent iron, can be explained by the fact that the ground state configurations of both Os^+ and Fe^+ are s^1d^6, whereas it is d^7 for Ru^+. The configuration of Os^+ and Fe^+ allows a covalent bond between H(1*s*) and the M^+(*s*) orbitals to form with little promotion energy. When calculated as a 50% mixture of the ^6D and ^4D states (which spin-decouples the bonding *s* electron from the *d* electrons, thereby accounting for the loss of spin-exchange energy when the MH^+ bond is formed), the promotion energies are 0.49 (Ref. 81) and 0.56 (Ref. 30) eV, respectively. For Ru^+, the d^7 ground state requires promotion to the s^1d^6 state to form a covalent M^+(*s*)–H(1*s*) bond. For Ru^+, the promotion energy (again calculated as a 50% mixture of ^6D and ^4D states) is high, 1.72 eV,[9] such that RuH$^+$ is formed by a covalent bond between the dσ orbital of the d^7 ground state configuration of Ru^+ and H (1*s*), where the promotion energy is smaller, 0.66 eV,[9] but the M^+(dσ)–H(1*s*) bond is weaker. Os^+ can form a stronger bond than Fe^+ by utilizing a *sd* hybridized orbital rather than either the pure *s* or pure *d* orbitals. Hybridization is particularly effective for the third-row transition metals because of the similar size of the *s* and *d* orbitals, a result of the lanthanide contraction, which makes the 6*s* orbitals of the third-row metals relatively tighter than the 4*s* and 5*s* orbitals of the first-row and second-row congeners. For Os^+, the 6*s* orbital is 1.61 times the size of the 5*d* orbitals.[81] For Fe^+, the 4*s* orbital is 2.45 times the size of the 3*d* orbitals[81] and for Ru^+, the 5*s* orbital is 1.89 times the size of the 4*d* orbitals.[82] Overall,

these various factors determine that OsH^+ has the strongest bond followed by FeH^+, whereas RuH^+ has the weakest bond.

B. Reaction mechanism

Further comparison of the group 8 metal ions is facilitated by examining the reaction mechanisms as revealed by the reaction with HD. Previous work on the first-row and second-row transition metal cations indicates that the product branching ratio in the reaction of M^+ with HD is sensitive to the reaction mechanism[3,4,12,13,54] and is governed by three "rules." (1) If M^+ has an electron configuration with empty valence s and $d\sigma$ orbitals, such as for a d^n configuration where $n < 5$, the reaction is efficient and may proceed by an insertion mechanism. These processes are characterized by nearly equal amounts of MH^+ and MD^+, consistent with statistical behavior of a long-lived intermediate. Thus, product branching ratios in the HD system yield ($\sigma_{MH^+}/\sigma_{Total}$) values that are near 0.5. (2) If either the valence s or $d\sigma$ orbital is occupied and the M^+ state is low-spin, such as for d^n ($n > 5$) or low-spin coupled s^1d^{n-1} configurations, the reaction occurs efficiently via a direct mechanism. These processes are characterized by a product branching ratio in the HD system that favors MH^+ by a factor of 2–4, giving ($\sigma_{MH^+}/\sigma_{Total}$) ratios between 0.66 and 0.8, consistent with arguments concerning the conservation of angular momentum.[53,58,83–85] (3) If either the valence s or $d\sigma$ orbital is occupied and the M^+ state is high-spin (the highest spin it can possibly have), such as a high-spin coupled s^1d^{n-1} configuration, the reaction is inefficient and tends to react impulsively. These processes are characterized by a product branching ratio in the HD system that favors $MD^+ + H$ by a large factor, small values of the ($\sigma_{MH^+}/\sigma_{Total}$) ratio, and exhibit shifts in the thresholds for the H_2 and D_2 systems versus the HD system. Note that these rules are only appropriate for the diabatic reaction behavior, i.e., cases where the electron configuration of the metal ions remains essentially static throughout the course of the reaction.

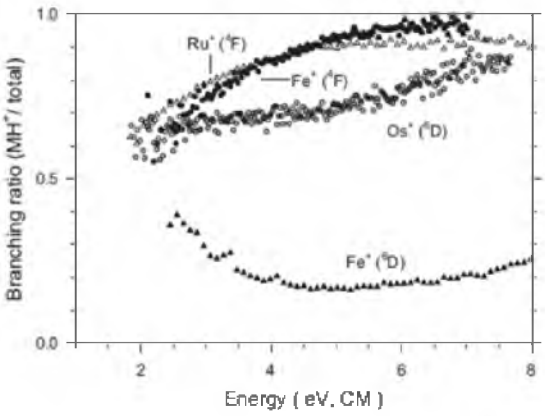

FIG. 4. Product branching fractions ($\sigma_{MH^+}/\sigma_{total}$) for reactions of Fe^+ (^6D), Fe^+ (^4F), Ru^+ (^4F), and Os^+ (^6D) with HD as a function of kinetic energy.

Results for the reactions of Os^+ are compared to those for the lighter congeners in Fig. 4 in terms of the fraction of metal hydride ion product formed ($\sigma_{MH^+}/\sigma_{Total}$). For Fe^+ (^6D, $4s^13d^6$), one would expect it to react according to "rule 3," an impulsive mechanism, which, in fact, it does. Here, production of FeD^+ is greatly favored over the production of FeH^+. For Fe^+ (^4F, $3d^7$), one would expect it to react according to "rule 2," a direct mechanism, which is supported by Fig. 4. In this reaction, the production of FeH^+ is favored over production of FeD^+ by a factor of about 2 near threshold, increasing at higher energies. Similarly, Ru^+ (^4F, $4d^7$) has a $\sigma_{MH^+}/\sigma_{total}$ ratio comparable to that of Fe^+ (^4F) and reacts according to "rule 2," in which the production of RuH^+ is favored over production of RuD^+.

According to the rules of diabatic reactivity above, Os^+(^6D, $6s^15d^6$), such as Fe^+(^6D, $4s^13d^6$), should react diabatically with dihydrogen according to "rule 3," that is, via an impulsive mechanism. Such a prediction is inconsistent with the experimental cross sections. However, in agreement with this prediction, the calculated potential energy surfaces indicate that the Os^+ (^6D) ground state forms only a weakly bound ion-induced dipole complex (small H–Os–H bond angles), Fig. 3. As the bond angle increases in an attempt to

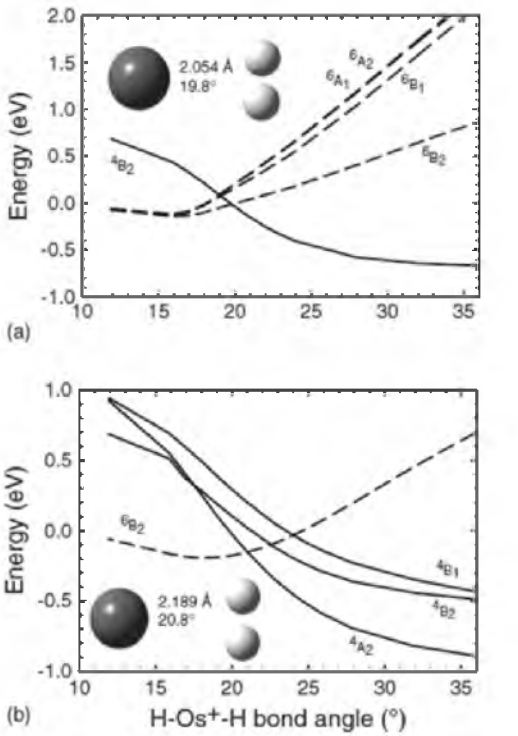

FIG. 5. Relaxed potential energy surface scans at the B3LYP/def2-TZVPP/6-311+G(3p) level of theory for interaction of Os^+ with H_2. Results are shown for optimization along the $^4B_2$ (part a) and $^6B_2$ (part b) surfaces with single point energies at the same geometries for the other spin state. Geometries of the approximate crossing points (CP) between the lowest energy surfaces are also shown in each part with Os–H bond lengths and HOsH bond angles provided.

TABLE VII. Calculated bond lengths, angles, and energies for the crossing points between quartet and sextet surfaces of OsH_2^+.

Optimized surface	Crossing surface	r(Os–H) (Å)	∠HOsH (deg)	E_{rel} (eV)[a]
$^6B_2$	$^4A_2$	2.189	20.8	−0.154
$^6B_2$	$^4B_2$	2.106	22.5	−0.101
$^6B_2$	$^4B_1$	2.042	24.0	−0.034
$^4B_2$	$^6B_2$	2.054	19.8	−0.012
$^4B_2$	$^6B_1$	2.117	19.1	0.076
$^4B_2$	$^6A_{1,2}$	2.126	19.0	0.088

[a]Energy relative to the $Os^+(^6D) + H_2$ asymptote.

insert into the H_2 bond, the energy increases rapidly, as expected for an impulsive type of reaction. Therefore, the experimental behavior observed at threshold is inconsistent with reaction along any of the sextet surfaces. Rather, Os^+, behaves more like category 2, which involves a direct reaction, consistent with a low-spin s^1d^{n-1} configuration such as the ^4D state. As seen from the calculated potential energy surfaces, there are several quartet surfaces evolving from Os^+ (^4D, $6s^15d^6$) configurations that lead to strongly bound OsH_2^+ intermediates, which can dissociate to ground state $OsH^+ + H$ without barriers in excess of the product asymptote. Thus, the experiment demonstrates that the reaction of $Os^+ + H_2$ must occur by coupling the sextet and quartet surfaces. Such "two-state reactivity"[86] has long been known to be influential in the reactions of transition metal systems,[7,10] and has been shown to be particularly important for heavier metal systems.[14,16,75]

To approximate the character of the crossing seam, we take the approach of Yoshizawa *et al.*[87] Thus, a relaxed potential energy surface scan conducted at the B3LYP/def2-TZVPP/6-311+G(3*p*) level along a likely region of coordinate space for each spin state is conducted and then single point energies of the other spin state at the same geometries are also calculated. Figure 3 clearly shows that the surfaces are likely to cross in the entrance channel. Figure 5 shows the results of the relaxed potential energy surface scan calculations, which were restricted to those for the lowest energy surfaces of each spin state, $^6B_2$ and $^4B_2$. Calculations for the other sextet and quartet surfaces are anticipated to be similar. The energies and geometric parameters of the crossing points (CPs) located are listed in Table VII with the geometry of the lowest CPs in each case shown in Figure 5. The CPs, all occur in the same region, namely at long Os–H bond distances, 2.04–2.19 Å, and small ∠HOsH bond angles, 19°–24°, meaning the H_2 bond is still intact. The energies of the CPs are comparable to those of ground state reactants, lying 0.15 eV below to 0.09 eV above this asymptote.

VI. CONCLUSIONS

Analysis of the kinetic energy dependence of the reaction cross sections provides the BDE of Os^+–H, 2.45 ± 0.10 eV. Our experimental results are in reasonable agreement with quantum chemical calculations performed here at the BHLYP and CCSD(T) level and in the literature.[30,37] The bond dissociation energy of the OsH^+ ground state is found to be larger than that for either the first- or second-row transition metal hydride cations FeH^+ and RuH^+. This difference is a consequence of lanthanide contraction and relativistic effects,[80,88] which alter the relative size of the valence *s* and *d* orbitals and make *s*-*d*σ hybridization more effective.

The branching ratios observed in the reactions with HD show that the ground state of Os^+ reacts with dihydrogen largely via a direct mechanism. This contrasts with expectations for the high-spin ground states of the metal ions that are based on diabatic reactivity rules. This behavior can be explained as long as this reaction system does not maintain sextet spin as it progresses along the potential energy surface. Coupling of the sextet surfaces that correlate with the ground state reactants to quartet surfaces provides access to strongly bound dihydride intermediates that can decompose to OsH^+ ($^5\Pi$) + H products with no barriers in excess of the reaction endothermicity (Fig. 3).

ACKNOWLEDGMENTS

This work is supported by the National Science Foundation (NSF), Grant No. 1049580. Laura Parke is thanked for helping to develop the safety precautions needed to handle osmium safely. Professor Michael D. Morse is thanked for the osmium sample used in these experiments. We thank the reviewers for several useful observations.

[1]R. A. Sanchez-Delgado, M. Rosales, M. A. Esteruelas, and L. A. Oro, J. Mol. Catal. A: Chem. **96**, 231 (1995).
[2]A. T. Larson, Ind. Eng. Chem. **16**, 1002 (1924).
[3]P. B. Armentrout, ACS Symp. Ser. **428**, 18 (1990).
[4]P. B. Armentrout, Int. Rev. Phys. Chem. **9**, 115 (1990).
[5]J. L. Elkind and P. B. Armentrout, J. Phys. Chem. **91**, 2037 (1987).
[6]M. L. Mandich, L. F. Halle, and J. L. Beauchamp, J. Am. Chem. Soc. **106**, 4403 (1984).
[7]J. L. Elkind and P. B. Armentrout, J. Phys. Chem. **90**, 5736 (1986).
[8]J. L. Elkind and P. B. Armentrout, J. Chem. Phys. **84**, 4862 (1986).
[9]J. L. Elkind and P. B. Armentrout, Inorg. Chem. **25**, 1078 (1986).
[10]J. L. Elkind and P. B. Armentrout, J. Phys. Chem. **90**, 6576 (1986).
[11]J. L. Elkind, L. S. Sunderlin, and P. B. Armentrout, J. Phys. Chem. **93**, 3151 (1989).
[12]Y.-M. Chen, J. L. Elkind, and P. B. Armentrout, J. Phys. Chem. **99**, 10438 (1995).
[13]M. R. Sievers, Y.-M. Chen, J. L. Elkind, and P. B. Armentrout, J. Phys. Chem. **100**, 54 (1996).
[14]X.-G. Zhang, C. Rue, S.-Y. Shin, and P. B. Armentrout, J. Chem. Phys. **116**, 5574 (2002).
[15]X.-G. Zhang and P. B. Armentrout, J. Chem. Phys. **116**, 5565 (2002).
[16]F.-X. Li and P. B. Armentrout, J. Chem. Phys. **121**, 248 (2004).
[17]F.-X. Li, X.-G. Zhang, and P. B. Armentrout, J. Phys. Chem. B **109**, 8350 (2005).
[18]C. S. Hinton and P. B. Armentrout, J. Chem. Phys. **133**, 124307 (2010).
[19]F.-X. Li, C. S. Hinton, M. Citir, E.-Y. Liu, and P. B. Armentrout, J. Chem. Phys. **134**, 024310 (2011).
[20]P. B. Armentrout, R. V. Hodges, and J. L. Beauchamp, J. Chem. Phys. **66**, 4683 (1977).
[21]P. B. Armentrout, R. V. Hodges, and J. L. Beauchamp, J. Am. Chem. Soc. **99**, 3163 (1977).
[22]P. B. Armentrout and J. L. Beauchamp, Chem. Phys. **48**, 315 (1980).
[23]R. Georgiadis and P. B. Armentrout, J. Phys. Chem. **92**, 7060 (1988).
[24]N. F. Dalleska, K. C. Crellin, and P. B. Armentrout, J. Phys. Chem. **97**, 3123 (1993).
[25]P. B. Armentrout and B. L. Kickel, in *Organometallic Ion Chemistry*, edited by B. S. Freiser (Kluwer, Dordrecht, 1996), p. 1.
[26]P. B. Armentrout, in *Topics in Organometallic Chemistry*, edited by J. M. Brown and P. Hofmann (Springer-Verlag, Berlin, 1999), Vol. 4-1, p. 1.

[27] P. B. Armentrout, Int. J. Mass. Spectrom. **200**, 219 (2000).
[28] R. H. Crabtree, *The Organometallic Chemistry of the Transition Metals*, 2nd ed. (Wiley, New York, 1994).
[29] G. A. Somorjai, *Introduction to Surface Chemistry and Catalysis* (Wiley, New York, 1994).
[30] G. Ohanessian, M. J. Brusich, and W. A. Goddard III, J. Am. Chem. Soc. **112**, 7179 (1990).
[31] K. Balasubramanian and D. Dai, J. Chem. Phys. **93**, 7243 (1990).
[32] K. K. Das and K. Balasubramanian, J. Chem. Phys. **94**, 3722 (1991).
[33] D. Dai and K. Balasubramanian, J. Chem. Phys. **95**, 4284 (1991).
[34] D. Dai and K. Balasubramanian, Chem. Phys. Lett. **185**, 165 (1991).
[35] D. G. Dai, W. Cheng, and K. Balasubramanian, J. Chem. Phys. **95**, 9094 (1991).
[36] K. Balasubramanian and Z. Ma, J. Phys. Chem. **95**, 9794 (1991).
[37] T. Leininger, J.-F. Riehl, G.-H. Jeung, and M. Pelissier, Chem. Phys. Lett. **205**, 301 (1993).
[38] H. Zhang and K. Balasubramanian, J. Phys. Chem. **96**, 6981 (1992).
[39] S. K. Loh, D. A. Hales, L. Lian, and P. B. Armentrout, J. Chem. Phys. **90**, 5466 (1989).
[40] R. H. Schultz and P. B. Armentrout, Int. J. Mass Spectrom. Ion Process. **107**, 29 (1991).
[41] E. Teloy and D. Gerlich, Chem. Phys. **4**, 417 (1974).
[42] D. Gerlich, Adv. Chem. Phys. **82**, 1 (1992).
[43] N. R. Daly, Rev. Sci. Instrum. **31**, 264 (1960).
[44] K. M. Ervin and P. B. Armentrout, J. Chem. Phys. **83**, 166 (1985).
[45] P. J. Chantry, J. Chem. Phys. **55**, 2746 (1971).
[46] B. L. Kickel and P. B. Armentrout, J. Am. Chem. Soc. **117**, 4057 (1995).
[47] D. E. Clemmer, Y.-M. Chen, F. A. Khan, and P. B. Armentrout, J. Phys. Chem. **98**, 6522 (1994).
[48] C. L. Haynes and P. B. Armentrout, Organometallics **13**, 3480 (1994).
[49] B. L. Kickel and P. B. Armentrout, J. Am. Chem. Soc. **117**, 764 (1995).
[50] C. E. Moore, "Atomic energy levels," in National Standard Reference Data Series (U.S., National Bureau Standard 1971), Vol. 3, P. 35.
[51] T. A. M. van Kleef and P. F. A. Klinkenberg, Physica **130**, 83 (1961).
[52] W. J. Chesnavich and M. T. Bowers, J. Phys. Chem. **83**, 900 (1979).
[53] N. Aristov and P. B. Armentrout, J. Am. Chem. Soc. **108**, 1806 (1986).
[54] P. B. Armentrout, in *Advances in Gas Phase Metal Ion Chemistry*, edited by N. G. Adams and L. M. Babcock (JAI, Greenwich, 1992), Vol. 1, p. 83.
[55] E. Muntean and P. B. Armentrout, J. Chem. Phys. **115**, 1213 (2001).
[56] M. E. Weber, J. L. Elkind, and P. B. Armentrout, J. Chem. Phys. **84**, 1521 (1986).
[57] K. P. Huber and G. Herzberg, *Molecular Spectra and Molecular Structure* (Van Nostrand Reinhold, New York, 1974), Vol. IV.
[58] J. L. Elkind and P. B. Armentrout, J. Phys. Chem. **89**, 5626 (1985).
[59] P. B. Armentrout, in *Gas Phase Inorganic Chemistry*, edited by D. H. Russell (Plenum, New York, 1989), p. 1.
[60] P. B. Armentrout, in *Selective Hydrocarbon Activation: Principles and Progress*, edited by J. A. Davies, P. L. Watson, A. Greenberg, and J. F. Liebman (VCH, New York, 1990), p. 467.
[61] A. D. Becke, J. Chem. Phys. **98**, 5648 (1993).
[62] C. Lee, W. Yang, and R. G. Parr, Phys. Rev. B **37**, 785 (1988).
[63] M. J. Frisch, G. W. Trucks, H. B. Schlegel *et al.* GAUSSIAN 09, Revision A.02, Gaussian, Inc., Wallingford, CT, 2009.
[64] D. Andrae, U. Haeussermann, M. Dolg, H. Stoll, and H. Preuss, Theor. Chim. Acta **77**, 123 (1990).
[65] P. J. Hay and W. R. Wadt, J. Chem. Phys. **82**, 299 (1985).
[66] F. Weigend and R. Ahlrichs, Phys. Chem. Chem. Phys. **7**, 3297 (2005).
[67] D. Feller, J. Comput. Chem. **17**, 1571 (1996); K. L. Schuchardt, B. T. Didier, T. Elsenthagen, L. Sun, V. Gurumoorthi, J. Chase, J. Li, and T. L. Windus, J. Chem. Inf. Model. **47**, 1045 (2007).
[68] M. Dolg, H. Stoll, H. Preuss, and R. M. Pitzer, J. Phys. Chem. **97**, 5852 (1993).
[69] J. B. Foresman and Æ. Frisch, *Exploring Chemistry with Electronic Structure Methods*, 2nd ed. (Gaussian, Pittsburgh, PA, 1996).
[70] M. C. Holthausen, C. Heinemann, H. H. Cornehl, W. Koch, and H. Schwarz, J. Chem. Phys. **102**, 4931 (1995).
[71] M. C. Holthausen, M. Mohr, and W. Koch, Chem. Phys. Lett. **240**, 245 (1995).
[72] L. G. Parke, C. S. Hinton, and P. B. Armentrout, Int. J. Mass Spectrom. **254**, 168 (2006).
[73] L. G. Parke, C. S. Hinton, and P. B. Armentrout, J. Phys. Chem. C **111**, 17773 (2007).
[74] P. B. Armentrout, S. Shin, and R. Liyanage, J. Phys. Chem. A **110**, 1242 (2006).
[75] M. M. Armentrout, F.-X. Li, and P. B. Armentrout, J. Phys. Chem. A **108**, 9660 (2004).
[76] F.-X. Li, X.-G. Zhang, and P. B. Armentrout, Int. J. Mass Spectrom. **255**, 279 (2006).
[77] X.-G. Zhang, R. Liyanage, and P. B. Armentrout, J. Am. Chem. Soc. **123**, 5563 (2001).
[78] F.-X. Li and P. B. Armentrout, J. Chem. Phys. **125**, 133114 (2006).
[79] M. Benavides-Garcia and K. Balasubramanian, J. Mol. Spectrosc. **150**, 271 (1991).
[80] H. Schwarz, Angew. Chem. **42**, 4442 (2003).
[81] J. B. Schilling, W. A. Goddard III, and J. L. Beauchamp, J. Phys. Chem. **91**, 5616 (1987).
[82] J. B. Schilling, W. A. Goddard III, and J. L. Beauchamp, J. Am. Chem. Soc. **109**, 5565 (1987).
[83] L. S. Sunderlin, N. Aristov, and P. B. Armentrout, J. Am. Chem. Soc. **109**, 78 (1987).
[84] J. D. Burley, K. M. Ervin, and P. B. Armentrout, Int. J. Mass Spectrom. Ion Process. **80**, 153 (1987).
[85] P. B. Armentrout, ACS Symp. Ser. **502**, 194 (1992).
[86] D. Schröder, S. Shaik, and H. Schwarz, Acc. Chem. Res. **33**, 139 (2000).
[87] K. Yoshizawa, Y. Shiota, and T. Yamabe, J. Chem. Phys. **111**, 538 (1999).
[88] H. Schwarz and D. Schröder, Pure Appl. Chem. **72**, 2319 (2000).

CHAPTER 5

REACTIONS OF Hf^+, Ta^+, AND W^+ WITH O_2 AND CO: METAL CARBIDE AND METAL OXIDE CATION BOND ENERGIES

Christopher S. Hinton, Fengxia Li, P. B. Armentrout

Reprinted from ***International Journal of Mass Spectrometry, Volume 280***, *Issues 1-3*
Christopher S. Hinton, Fengxia Li, P. B. Armentrout, Reactions of Hf^+, Ta^+, and W^+ with O_2 and CO: Metal Carbide and Metal Oxide Cation Bond Energies, Pages 226-234, with permission from Elsevier

Contents lists available at ScienceDirect

International Journal of Mass Spectrometry

journal homepage: www.elsevier.com/locate/ijms

Reactions of Hf^+, Ta^+, and W^+ with O_2 and CO: Metal carbide and metal oxide cation bond energies

Christopher S. Hinton, Fengxia Li, P.B. Armentrout *

Chemistry Department, University of Utah, 315 South, 1400 East, Room 2020, Salt Lake City, UT 84112, United States

ARTICLE INFO

Article history:
Received 5 August 2008
Received in revised form 27 August 2008
Accepted 27 August 2008
Available online 7 September 2008

This article is dedicated to Zdenek Herman on the occasion of his 75th birthday and in recognition of his outstanding contributions to ion chemistry and the mass spectrometry community over many years.

Keywords:
Bond energy
Ionization energy
Transition metal carbide
Transition metal oxide
Thermochemistry

ABSTRACT

The reactions of Hf^+, Ta^+, and W^+ with O_2 and CO are studied as a function of translational energy in a guided ion beam tandem mass spectrometer. All three reactions with O_2 form diatomic metal oxide cations in exothermic reactions that occur at the collision rate. In the CO systems, formation of both diatomic metal oxide and metal carbide cations is observed to be endothermic. The energy-dependent cross sections in the latter systems are interpreted to give 0 K bond energies (in eV) of $D_0(HfC^+) = 3.19 \pm 0.03$, $D_0(TaC^+) = 3.79 \pm 0.04$, $D_0(WC^+) = 4.76 \pm 0.09$, $D_0(HfO^+) = 6.91 \pm 0.11$, $D_0(TaO^+) = 7.10 \pm 0.12$, and $D_0(WO^+) = 6.77 \pm 0.07$. The present experimental values for TaO^+ and WC^+ agree well with literature thermochemistry, those for HfO^+ and WO^+ refine the available literature bond energies, and those for HfC^+ and TaC^+ are the first measurements available. The nature of the bonding in MO^+ and MC^+ is discussed and compared for these three metal ions and analyzed using theoretical calculations at a B3LYP/HW+/6-311+G(3df) level of theory. Bond energies for all MO^+ and MC^+ species are calculated using geometries calculated at this level and single point energies determined at B3LYP, CCSD, CCSD(T), QCISD, and QCISD(T) levels of theory with the same basis set. Reasonable agreement between the theoretical and experimental bond energies for the three metal oxide and three metal carbide cations is found. Potential energy surfaces for reaction of the metal cations with CO are also calculated at the B3LYP level of theory and reveal additional information about the reaction mechanisms.

1. Introduction

Transition metal carbides and oxides play an important role in many processes. Because of their high melting point, conductivity, and hardness, transition metal carbides play important roles in material science and electronics [1–3]. The oxides of transition metals play vital roles in industrial, organometallic, and atmospheric chemistry [4–6]. In understanding the origins of these important properties, it can be useful to understand the binding of the simplest examples of such species. In previous studies in our laboratory, guided ion beam mass spectrometry has been used to systematically study diatomic oxides, MO^+, and carbides, MC^+, of first-row [7,8], second-row [9–11], and third-row [12] transition metal cations. In the present work, these studies are extended to include the group 4–6 third-row transition metal cations, M = Hf, Ta, and W. The comparison of the metal carbides and oxides is interesting because both C and O have two unpaired valence electrons in their ^3P ground states, easily making two covalent bonds to metals. However, the empty p orbital on C versus the doubly occupied p orbital on oxygen can make an appreciable difference in the bonding of these species with metals.

The guided ion beam methods used in our laboratory can be used to investigate the bond dissociation energies (BDEs) for M^+–O and M^+–C species by analyses of the kinetic energy dependence of reactions (1)–(3).

$$M^+ + O_2 \rightarrow MO^+ + O \quad (1)$$

$$M^+ + CO \rightarrow MO^+ + C \quad (2)$$

$$M^+ + CO \rightarrow MC^+ + O \quad (3)$$

In previous work [7–11], it has been shown that the early transition metal cations (groups 3–5) react exothermically with O_2, whereas later transition metal cations (groups 6–11) react endothermically. To obtain metal oxide bond energies for these early metal cations, reactions with CO, which has a much stronger bond, $D_0(CO) = 11.108$ eV versus $D_0(O_2) = 5.115$ eV [13], can be used as now the processes are endothermic. Furthermore, the competing formation of MC^+ in reaction (3) is also observed, such that analyses of the energy-dependent cross section data for reactions (2) and (3) allow 0 K metal oxide and metal carbide BDEs to be obtained. Detailed theoretical calculations are also performed here in order

* Corresponding author. Tel.: +1 801 581 7885; fax: +1 801 581 8433.
E-mail address: armentrout@chem.utah.edu (P.B. Armentrout).

to provide information regarding the electronic states of the MC^+ and MO^+ species and to examine the potential energy surfaces for formation of the products in reactions (2) and (3).

2. Literature data

Literature information on thermodynamics of these transition metal oxide and carbide species is generally sparse, although all three metal oxides have been studied by Knudsen effusion techniques. Panish and Reif used Langmuir vaporization and Knudsen effusion to measure the 0 K dissociation energy of HfO as 7.92 ± 0.26 eV [14], and later Ackermann and Rauh measured a value of 8.19 ± 0.09 eV [15]. Pedley and Marshall critically evaluate these values and select $D_0(HfO) = 8.26 \pm 0.13$ eV [16]. In contrast, an RKR analysis of spectroscopic information suggests that $D_0(HfO) = 9.04 \pm 0.02$ eV [17], but this value is less reliable because of the long range extrapolation involved. Using Eq. (4),

$$D_0(M-X) + IE(M) = D_0(M^+ - X) + IE(MX) \quad (4)$$

the ionization energy of this species, $IE(HfO) = 7.55 \pm 0.1$ eV, measured by Rauh and Ackermann [18], and $IE(Hf) = 6.825$ eV [19] can be combined with the best neutral BDE to yield $D_0(Hf^+–O) = 7.54 \pm 0.16$ eV. The review of transition metal oxide cations by Schroder et al. [20] lists $D(Hf^+–O) = 7.50 \pm 0.22$ eV and cites the GIANT (Gas-phase Ion And Neutral Thermochemistry) compilation [21], which used the same reference data for HfO but an older value for $IE(Hf) = 6.78$ eV. ESR studies [22] identify HfO^+ as having a $^2\Sigma$ ground state and a variety of spectroscopic studies of HfO [23–25] have also been performed.

For tantalum oxide, the JANAF tables [26] discuss the large disparities obtained by several Knudsen cell mass spectrometry studies [27–29]: 2nd and 3rd law values for $\Delta_f H_{298}(TaO)$ values ranging from 2.14 to 4.35 eV. After correlating values with those for the 1st and 2nd row congeners, VO and NbO, Chase chooses a rounded value from a Birge–Sponer extrapolation corrected for iconicity, $\Delta_f H_{298}(TaO) = 1.99_5 \pm 0.65$ eV and $D_0(TaO) = 8.65 \pm 0.65$ eV. Pedley and Marshall [16] primarily utilize results from Smoes et al. [30] and select $D_0(TaO) = 8.24 \pm 0.13$ eV. The situation for the ionization energy of TaO is equally unclear. The most precise and most recent value comes from a photoelectron measurement of Dyke et al., 8.61 ± 0.02 eV [31], which is well above previous electron impact measurements of $7.9_2 \pm 0.1$ eV from Ackermann et al. [32] and 7.5 ± 0.5 eV from Smoes et al. [30]. Combining the best values presently available with $IE(Ta) = 7.5495$ eV [33] yields $D_0(Ta^+–O) = 7.18 \pm 0.14$ eV. The review by Schroder et al. [20] lists $D(Ta^+–O) = 8.15 \pm 0.65$ eV, again citing the GIANT compilation [21], which uses older values for $IE(Ta) = 7.4$ eV and $IE(TaO) = 7.92$ eV, along with $D_0(TaO) = 8.65$ eV. Additional work has examined the spectroscopy of TaO, identifying its ground state as $^2\Delta$ [34–38], and has characterized the photoelectron spectrum of TaO^- [39].

Finally, the JANAF tables [26] reanalyzed the Knudsen cell mass spectrometry data of DeMaria et al. [40] to determine $\Delta_f H_0(WO) = 4.41 \pm 0.43$ eV, which can be combined with the heats of formation of W and O (also taken from JANAF) to give $D_0(WO) = 6.95 \pm 0.44$ eV, somewhat higher than the value quoted directly by DeMaria et al. of 6.68 ± 0.44 eV. (Also, using $H_{298} - H_0$ data taken from the JANAF tables, one finds that $D_{298}(W–O) - D_0(W–O) = 0.043$ eV, yielding $D_{298}(WO) = 7.00 \pm 0.44$ eV.) Pedley and Marshall use the same data to select $D_0(WO) = 6.92 \pm 0.44$ eV. DeMaria et al. also quote a rough ionization energy for WO of 9.1 ± 1 eV, but recent gas-phase bracketing studies by Bohme and co-workers have refined this greatly to 8.1 ± 0.3 eV [41]. When combined with $IE(W) = 7.864$ eV [42] and $D_0(WO) = 6.92 \pm 0.44$ eV, this IE value yields $D_0(W^+–O) = 6.68 \pm 0.53$ eV. This value is well above that quoted in the review by Schroder et al. [20] who list $D(W^+–O) = 5.46 \pm 0.43$ eV as taken from the GIANT compilation [21]. Bohme and co-workers verified the accuracy of their cation bond energy by determining that W^+ reacts at room temperature with COS to form WO^+, albeit with an efficiency of only 0.38. They took this to indicate that $D_{298}(W^+–O) > D_{298}(O–CS) = 6.85 \pm 0.04$ eV (although the inefficiency of this reaction could mean that these bond energies are nearly isoenergetic). They then combined this limit with $D_{298}(W^+–O) = 6.81 \pm 0.82$ eV (which is slightly higher than the value derived above for reasons that are unknown and with an uncertainty determined by addition of the literature uncertainties rather than combining them in quadrature) to yield a refined range of values that is cited as $D_{298}(W^+–O) = 7.20 \pm 0.43$ eV. This value is then combined with the ionization energies of W and WO to determine a value for $D_{298}(W–O)$ as 7.46 ± 0.74 eV, or equivalently $D_0(W–O) = 7.42 \pm 0.74$ eV, consistent with the JANAF and Pedley and Marshall values within the broad uncertainties. Spectroscopic work [43,44] has identified the ground state of WO as $X^3\Sigma^-$.

For the carbide of Hf, we could find no literature reports of gas-phase studies. A number of neutral [45] and cationic [46,47] tantalum carbide clusters formed by laser vaporization have been studied. On the basis of the observation of several reactions involving TaC^+, McElvany and Cassady were able to bracket its bond energy as $3.38 \text{ eV} < D(TaC^+) < 6.11$ eV. Furthermore, Majumdar and Balasubramanian have studied this molecule and its neutral analogue theoretically [48,49]. For tungsten, spectroscopy has identified the ground state of WC as $^3\Delta$ [50]. The photoelectron spectrum of WC^- has been measured [51], and establishes the electron affinity of WC as well as the excitation energies for several excited states of this molecule. In addition, WC^+ has been observed as a product in the reaction of W^+ with CH_4 [52]. Measurement of the endothermic threshold for this double dehydrogenation reaction determined the 0 K bond energy of WC^+ as 4.96 ± 0.22 eV. WC^+ has also been observed in the fragmentation of $W(CO)_6$ ionized by electron impact [53] and by photoionization [54], and in the photoionization of W(CO) [55]. The appearance energies obtained in these studies suggest that $D_0(W^+–C) = 5.26 \pm 0.78$, 3.93 ± 0.36, and 3.86 ± 0.35 eV, respectively. Finally, we note that Musaev et al. have examined the WCO^+ system theoretically, exploring the potential energy surface for activation of the CO molecule by W^+ [56].

3. Experimental

3.1. General procedures

The guided ion beam tandem mass spectrometer on which these experiments were performed has been described in detail previously [57]. Ions are generated in a direct current discharge flow tube (DC/FT) source described below [58]. The ions are extracted from the source, accelerated, and focused into a magnetic sector momentum analyzer for mass selection of primary ions, where either the ^{180}Hf isotope (35.2% natural abundance), the ^{181}Ta isotope (99.99% natural abundance), or ^{186}W isotope (30.67% natural abundance) are selected. The mass selected ions are then slowed to a desired kinetic energy and focused into an octopole ion guide that radially traps the ions [59]. The octopole passes through a static gas cell that contains the neutral reaction partner at a low pressure (ranging from 0.05 to 0.2 mTorr) so that multiple ion–molecule collisions are improbable. All results reported here result from single bimolecular encounters, as verified by the independence of the measured cross sections on the neutral reactant pressure. Product and remaining reactant ions are contained in the guide until

they drift to the end of the octopole, where they are focused and extracted into a quadrupole mass filter for mass analysis and then detected. Reaction cross sections are calculated from product ion intensities relative to reactant ion intensities after correcting for background signals [60]. Uncertainties in the absolute cross sections are estimated to be ±20%.

Laboratory ion energies (lab) are converted to energies in the center-of-mass frame (CM) by using the formula, $E_{CM} = E_{lab}\, m/(m+M)$, where M and m are the ion and neutral masses, respectively. Two effects broaden the cross section data: the kinetic energy distribution of the ion and the thermal motion of the neutral reactant gas (Doppler broadening) [61]. The absolute zero and the full width at half-maximum (fwhm) of the kinetic energy distribution of the reactant ions are determined by using the octopole beam guide as a retarding potential analyzer. The distributions of ion energies are independent of energy, nearly Gaussian, and have typical fwhm of 0.6–1.4 eV (lab). Uncertainties in the absolute energy scale are ±0.05 eV (lab).

3.2. Ion source

M^+ ions are produced in a DC/FT source, consisting of a cathode held at a high negative voltage (1.1–1.5 kV) over which a flow of approximately 90% He and 10% Ar passes at a total pressure of 0.3–0.5 Torr. The dc-discharge is used to ionize Ar and then accelerate these ions into a cathode either made of tantalum or iron with a cavity containing hafnium or tungsten metal. After the ions are swept down a meter-long flow tube, they undergo ~10^5 thermalizing collisions with He and Ar. No evidence for low-lying excited states of the three metal ions (such as cross section features having lower energy thresholds) within about 1% sensitivity is observed under these flow conditions. When compared to a surface ionization source, the DC/FT source has been found to generate Sc^+ [62], Fe^+ [63], Co^+ [64], Ni^+ [65], Ru^+ [66], Rh^+ [66], and Pd^+ [66] ions with an average electronic temperature of 700 ± 400 K, and Y^+, Zr^+, Nb^+, and Mo^+ ions with an average electronic temperature of 300 ± 100 K [67]. Even at the maximum electronic temperature of 1100 K, the three metal ions populate the lowest energy spin–orbit level to a high degree as shown in Table S1, which lists the various low-lying states of Hf^+ [68], Ta^+ [69], and W^+ [70]. Conservatively, the average electronic energy, E_{el}, at a temperature of 700 ± 400 K for Hf^+ is 0.006 + 0.010/−0.006 eV, for Ta^+ is 0.025 + 0.039/−0.023 eV, and for W^+ is 0.018 + 0.040/−0.018 eV.

3.3. Data analysis

The cross sections of the endothermic reactions are modeled using Eq. (5) [71–74],

$$\sigma(E) = \frac{\sigma_0 \sum_i g_i (E + E_i + E_{rot} - E_0)^n}{E} \quad (5)$$

where σ_0 is an energy-independent scaling factor, E is the relative kinetic energy of the reactants, n is an adjustable parameter that characterizes the energy dependence of the process [71], E_{rot} is the rotational energy of the diatomic reactant (=k_BT at 300 K = 0.026 eV), and E_0 is the 0 K threshold for reaction of electronic, vibrational, and rotational state reactants. The model involves an explicit sum of the contributions of individual electronic states of the M^+ reactant, denoted by i, having energies E_i and populations g_i. Before comparison with the experimental data, Eq. (5) is convoluted with the kinetic energy distributions of the reactant ions and neutral reactants at 300 K. The σ_0, n, and E_0 parameters are then optimized using a nonlinear least-squares analysis to give the best reproduction of the data [71,73]. Error limits for E_0 are calculated from the range of threshold values for different data sets over a range of acceptable n values (as specified in the table of fitting parameters given below) combined with the absolute errors in the kinetic energy scale and internal energies of reactant ions.

At higher energies, the cross sections decline because the product ions have sufficient energy to dissociate. In this high-energy region, the data can be modeled by modifying Eq. (5) to include the dissociation probability according to a statistical model discussed elsewhere [75]. This probability is controlled by two parameters: p, which is an adjustable parameter similar to n, and E_d, which is the energy at which product ions start decomposing. In this study, the values of p and E_d are allowed to vary (although p can only hold integral values) and used to fit cross sections of M^+ with CO. Use of this high-energy model does not alter significantly the analysis of the threshold regions.

3.4. Theoretical calculations

Quantum chemistry calculations reported here were computed using the B3LYP hybrid density functional method [76,77] and performed with the GAUSSSIAN 03 suite of programs [78]. The 6-311+G(3df) basis set, triple zeta with diffuse and polarization functions, was used for carbon and oxygen in all calculations. As a point of comparison, the single point bond energies for O–O and C–O are calculated as 5.279 and 11.059 eV (uncorrected for spin–orbit coupling) compared to the experimental values of 5.115 and 11.108 eV [13], respectively.

The core electrons of hafnium, tantalum, and tungsten are described by the relativistic effective core potentials (ECP) of Hay-Wadt (HW) [79], with valence electrons described by the Los Alamos double zeta basis set (LANL2DZ). This basis set is optimized for neutral atoms, whereas the positive charge of the metal ion differentially contracts the s orbitals compared to the d orbitals. Therefore, calculations were performed with an altered HW-ECP basis set for the metal ions as described by Ohanessian et al. (designated as HW^+) [80]. The calculated thermochemistry is then corrected for zero point energy effects, after scaling the frequencies by 0.9804 [81]. Single point energies were also calculated from the B3LYP optimized geometries at QCISD, CCSD, QCISD(T), and CCSD(T) levels using the same basis sets. No corrections for spin–orbit coupling are included in the theoretical values, as discussed further below.

4. Results

4.1. Hf^+, Ta^+, and $W^+ + O_2$

Fig. 1 shows the cross sections of reaction (1) for $M^+ = Hf^+$, Ta^+, and W^+ as a function of kinetic energy. The HfO^+, TaO^+, and WO^+ cross sections decrease with increasing kinetic energy, consistent with the behavior of exothermic ion–molecule reactions. This behavior can be described using the Langevin–Gioumousis–Stevenson (LGS) model [82], Eq. (6),

$$\sigma_{LGS} = \pi e \left(\frac{\alpha}{2\pi\varepsilon_0 E}\right)^{1/2} \quad (6)$$

where e is the charge on the electron, α is the polarizability volume of the neutral reactant molecule (1.57 Å^3 for O_2) [83], and ε_0 is the permittivity of vacuum. As can be seen from Fig. 1, the cross sections for all three metal ions have energy dependences of $E^{-0.5\pm0.1}$ at energies below about 1 eV, as predicted by σ_{LGS}. The magnitudes of the cross sections obtained for the reactions are approximately equivalent to that of σ_{LGS} in this energy range (within the 20% absolute uncertainty), indicating that the reactions occur with 100 ± 20% efficiency. We can also convert this cross section into a room temperature rate constant using methods outlined previously

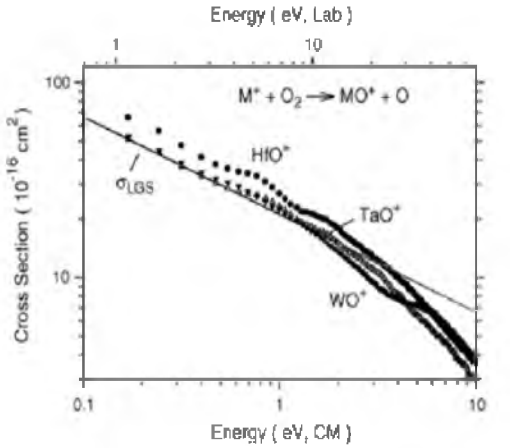

Fig. 1. Cross sections for reactions of Hf^+ (solid circles), Ta^+ (open triangles), and W^+ (solid inverted triangles) with O_2 as a function of kinetic energy in the center-of mass frame (lower *x*-axis) and laboratory frame (upper *x*-axis) for $M^+ = Hf^+$. The line shows the calculated collision cross section, σ_{LGS}.

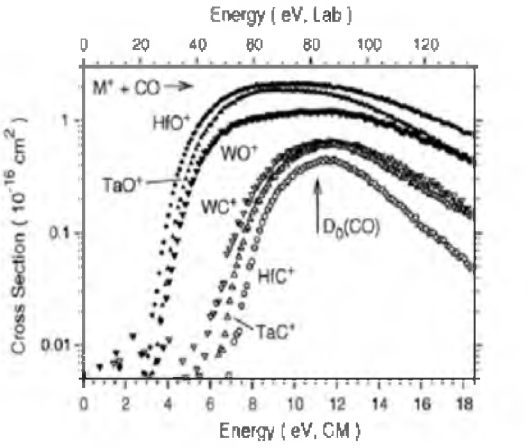

Fig. 2. Cross sections for reactions of Hf^+ (circles), Ta^+ (triangles), and W^+ (inverted triangles) with CO to form metal oxide (solid symbols) and metal carbide (open symbols) cation products as a function of kinetic energy in the center-of mass frame (lower *x*-axis) and laboratory frame (upper *x*-axis) for $M^+ = Hf^+$.

[57]. For Hf^+, Ta^+, and W^+, this yields rate constants of (6.9 ± 1.5), (6.1 ± 1.2), and $(6.0 \pm 1.2) \times 10^{-10}$ cm^3 molecule^{-1} s^{-1}, respectively, compared to $k_{LGS} = 5.6 \times 10^{-10}$ cm^3 molecule^{-1} s^{-1}. These values can be compared favorably with the rate constants measured by Bohme and co-workers in 0.35 Torr of helium at 295 K (4.1 ± 1.2), (4.7 ± 1.4), and $(4.4 \pm 1.3) \times 10^{-10}$ cm^3 molecule^{-1} s^{-1} [84], respectively, corresponding to reaction efficiencies of 67 ± 20, 82 ± 25, and $79 \pm 24\%$. The present values agree with these within experimental uncertainties although the high-pressure rate constants are systematically lower than the present single collision values for reasons that are unclear. However, it is notable that among the 29 transition metal ions examined in this work, the highest reaction efficiency observed was 82% (for Ta^+ and Zr^+), although there is no obvious reason why some of these metal cations could not react on every collision.

Above about 1 eV, the cross sections begin to decrease more rapidly. This effect can be attributed to angular momentum conservation restraints, as previously discussed in detail [85,86]. This argument recognizes that because the reduced mass of the products of reaction (1), μ', is smaller than that of the reactants, μ (μ'/μ is approximately 1/2 in these systems), the centrifugal barrier in the product channel can exceed that in the reactant channel for large angular momenta. This restricts the probability of reaction at higher kinetic energies. We have previously outlined a simple model to predict where these angular momentum constraints can restrict the product formation in exothermic reactions [86]. This begins at an energy given by Eq. (7),

$$E_C = \frac{(E - \Delta H)(\alpha'/\mu'^2)}{(\alpha/\mu^2)} \tag{7}$$

where α and α' are the polarizability volumes of the reactant and product neutrals (1.57 and 0.80 Å^3, respectively) [83,87], E is the relative kinetic energy of the reactants, and ΔH is the enthalpy of reaction. Using thermochemistry obtained below for HfO^+, TaO^+, and WO^+, this model predicts that the HfO^+, TaO^+, and WO^+ cross sections will become constrained beginning at 0.32, 0.35, and 0.29 eV, respectively, in reasonable agreement with the data.

We also observed HfO_2^+, TaO_2^+, and WO_2^+ at the lowest kinetic energies, products that are formed by secondary reactions of the primary MO^+ products, as verified by the dependence of the metal dioxide cation product cross sections on O_2 pressure. The kinetic energy dependences of the cross sections of these products are also consistent with the secondary reactions, $MO^+ + O_2 \rightarrow MO_2^+ + O$, and demonstrate that they are exothermic for all three metals.

4.2. Hf^+, Ta^+, and $W^+ + CO$

Cross sections for reactions (2) and (3) are shown in Fig. 2. The MO^+ cross sections rise from apparent thresholds of 3–4 eV, whereas the MC^+ cross sections require more energy, rising from thresholds of 5–7 eV. It can be seen that the relative ordering of the thresholds is inverted between the oxide and carbide ion products, with Hf^+ having the lowest oxide threshold and the highest carbide threshold, whereas W^+ has the highest oxide and lowest carbide thresholds. This should directly reflect the relative bond dissociation energies of these product ions. Both MC^+ and MO^+ cross sections reach maxima near 11 eV because both product ions can dissociate further in reaction (8),

$$M^+ + CO \rightarrow M^+ + C + O \tag{8}$$

which has a thermodynamic threshold of 11.108 eV = D_0(CO) [13].

5. Thermochemical and theoretical results

5.1. *Thermochemistry*

The exothermic reactions (1) for $M^+ = Hf^+$, Ta^+, and W^+ provide only lower limits to the HfO^+, TaO^+, and WO^+ BDEs, $D_0(M^+–O) \geq D_0(O_2) = 5.115$ eV [13]. Therefore, in order to determine the M^+—O bond strengths, the reactions of Hf^+, Ta^+, and W^+ with CO are used to determine the BDEs more precisely. If there are no reaction barriers in excess of the reaction endothermicities, as is often the case for ion–molecule reactions, then the BDEs of M^+–O and M^+–C can be derived from the E_0 thresholds of reactions (2) and (3) by using Eqs. (9) and (10), respectively. If such barriers did exist, then the bond energies derived would be lower limits to the true thermodynamic values, but the quantum chemical calculations on the potential energy surfaces detailed below verify the veracity of this assumption in the present cases.

$$D_0(M^+–O) = D_0(C–O) - E_0(MO^+) \tag{9}$$

$$D_0(M^+–C) = D_0(C–O) - E_0(MC^+) \tag{10}$$

The endothermic cross sections for reactions (2) and (3) were analyzed with Eq. (5). The optimized fitting parameters are listed in

Table 1
Fitting parameters of Eq. (5) used to model reactions (2) and (3)[a]

Reactant	Product	σ_0	n	E_0 (eV)	$D_0(M^+–A)$
Hf^+	HfO^+	2.39 (0.56)	1.4 (0.1)	4.20 (0.11)	6.91 (0.11)
Ta^+	TaO^+	3.14 (0.62)	1.2 (0.2)	4.01 (0.12)	7.10 (0.12)
W^+	WO^+	1.87 (0.28)	1.3 (0.1)	4.34 (0.07)	6.77 (0.07)
Hf^+	HfC^+	1.70 (0.06)	1.0 (0.1)	7.92 (0.03)	3.19 (0.03)
Ta^+	TaC^+	1.64 (0.13)	1.0 (0.1)	7.32 (0.04)	3.79 (0.04)
W^+	WC^+	0.88 (0.18)	1.4 (0.1)	6.35 (0.09)	4.76 (0.09)

[a] Uncertainties, in parentheses, are one standard deviation.

Table 1 and typical reproduction of the data is shown in Fig. 3. This includes the high-energy analysis that accounts for reaction (8) above 11 eV.

Analysis of reactions (2) yields thresholds (Table 1) leading to metal oxide bond energies of 6.91 ± 0.11, 7.10 ± 0.12, and 6.77 ± 0.07 eV for HfO^+, TaO^+, and WO^+, respectively. The former value is outside of the combined experimental uncertainties from the cationic BDE in the literature, 7.54 ± 0.16 or 7.50 ± 0.22 eV [20] (Table 2). We believe this is because the ionization energy of HfO measured by Ackermann and Rauh, IE(HfO) = 7.55 ± 0.1 eV [15], is probably too low, as found independently for TaO. Ackermann and Rauh determined IE(TaO) = 7.92 ± 0.1 eV, whereas a photoelectron spectrum by Dyke et al. yields 8.61 ± 0.02 eV [31], a discrepancy of 0.7 ± 0.1 eV. In the case of HfO, combining our cationic bond energy with the neutral bond energy of Pedley and Marshall [16], D_0(Hf–O) = 8.26 ± 0.13 eV, we derive IE(HfO) = 8.18 ± 0.17 eV (Table 3), 0.63 ± 0.20 eV higher than the previous value, a comparable discrepancy to that found for TaO. Equivalently, the IEs of HfO and TaO measured by Ackermann and Rauh differ by 0.4 eV, which is the same relationship as our revised IE(HfO) compared to IE(TaO) from Dyke et al..

In the tantalum oxide system, our cationic BDE of 7.10 ± 0.12 eV agrees very well with the best value presently in the literature, $D_0(Ta^+–O)$ = 7.18 ± 0.14 eV (Table 2). If we combine our cationic BDE with IE(TaO) = 8.61 ± 0.02 eV from Dyke et al. [31], we obtain D_0(Ta–O) = 8.16 ± 0.12 eV (Table 3), very similar to the value selected by Pedley and Marshall of 8.24 ± 0.13 eV [16].

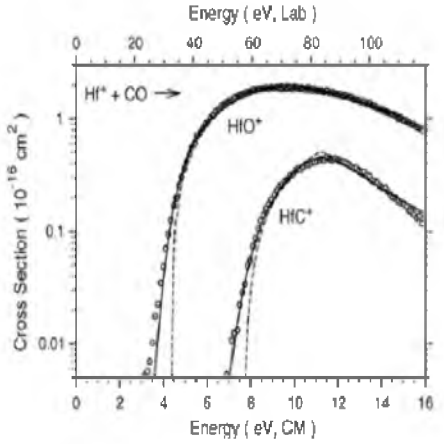

Fig. 3. Cross sections for formation of HfO^+ and HfC^+ in the reaction of Hf^+ with CO as a function of kinetic energy in the center-of-mass frame (lower x-axis) and laboratory frame (upper x-axis). Symbols indicate the experimental results. Dashed lines show the low energy model cross sections given by Eq. (5) and the parameters given in Table 1 along with a model for the dissociation of the product ions in reaction (8) at higher energies. Solid lines show these models convoluted over the experimental energy distributions.

For the tungsten oxide system, our measured BDE of 6.77 ± 0.07 eV is in very good agreement with the literature range determined using D_0(W–O) = 6.92 ± 0.44 eV from Pedley and Marshall [16] and IE(WO) = 8.1 ± 0.3 eV from Bohme and co-workers [41], $D_0(W^+–O)$ = 6.68 ± 0.53 eV (Table 2). Our value is also consistent with the observation of Bohme and co-workers that W^+ reacts at room temperature with COS to form WO^+. Bohme and co-workers interpreted this to mean that $D_{298}(W^+–O) \geq D_{298}$(O–CS) = 6.85 ± 0.04 eV, which is equivalent to $D_0(W^+–O) \geq 6.81 \pm 0.04$ eV, within experimental error of the present value. In this system, by combining our cation BDE with IE(WO) = 8.1 ± 0.3 eV [41], we refine the neutral BDE to D_0(W–O) = 7.01 ± 0.31 eV, consistent with but more precise

Table 2
Bond Dissociation Energies at 0 K[a]

Bond	Experiment		Theory					
	This work	Literature	B3LYP	QCISD(T)	CCSD(T)	QCISD	CCSD	Literature
O—O		5.115 ± 0.002[b]	5.279	4.929	4.914	4.627	4.954	
C—O		11.108 ± 0.005[b]	11.059	10.916	10.897	10.625	10.576	
Hf^+—O	6.91 ± 0.11	7.54 ± 0.16[c], 7.50 ± 0.22[d]	7.21	7.54	7.49	7.13	7.04	
Hf^+—C	3.19 ± 0.03		3.67	3.51	3.48	3.30	3.25	
Ta^+—O	7.10 ± 0.12	7.18 ± 0.14[e], 8.15 ± 0.65[d]	7.28	7.84	7.76	7.36	7.22	
Ta^+—C	3.79 ± 0.04	3.38–6.11[f]	4.48	4.79	4.88	4.72	4.32	4.50[g]
W^+—O	6.77 ± 0.07	6.68 ± 0.53[h], 7.16 ± 0.43[i] >6.81 ± 0.04[j], 5.46 ± 0.43[d]	6.92	7.11	6.96	6.78	6.60	
W^+—C	4.76 ± 0.09	4.96 ± 0.22[k], 3.93 ± 0.36[h] 3.86 ± 0.35[l], 5.26 ± 0.78[m]	4.88	4.34	4.39	4.81	4.57	
MAD			0.32	0.58	0.53	0.26	0.20	

[a] From this work, except as noted.
[b] Huber and Herzberg [13].
[c] Derived from references [16–19] and Eq. (4), see text.
[d] Schroder et al. [20].
[e] Derived from references [16,31,33] and Eq. (4), see text.
[f] Cassady and McElvany [46,47].
[g] Majumdar and Balasubramanian [48].
[h] Derived from references [16], [41], and [42] and Eq. (4), see text.
[i] Blagojevic et al. [41].
[j] Armentrout et al. [52].
[k] Qi et al. [54].
[l] Qi et al. [55].
[m] Winters and Kiser [53].

Table 3
Experimental thermochemical data for third row transition metal oxides

M^0–X	IE(M)	$D_0(M^+$–X)	D_0(M–X)		IE(MX)	
		This work	Literature	This work	Literature	This work
Hf–O	6.825[a]	6.91 ± 0.11	8.26 ± 0.13[b]		7.55 ± 0.1[c]	8.18 ± 0.17[d]
Ta–O	7.5495[e]	7.10 ± 0.12	8.24 ± 0.13[b]	8.16 ± 0.12[d]	8.61 ± 0.02[f], 7.92 ± 0.1[g], 7.5 ± 0.5[h]	8.69 ± 0.18[d]
W–O	7.864[i]	6.77 ± 0.07	6.92 ± 0.44[b], 6.95 ± 0.44[j]	7.01 ± 0.31[d]	8.1 ± 0.3[k], 9.1 ± 1[l]	8.04 ± 0.45[d]

[a] Callender et al. [19].
[b] Pedley and Marshall [16].
[c] Rauh and Ackermann [18].
[d] Derived from $D_0(MX)+IE(M)=D_0(MX^+)+IE(MX)$.
[e] Simard et al. [33].
[f] Dyke et al. [31].
[g] Ackermann et al. [32].
[h] Smoes et al. [30].
[i] Campbell-Miller and Simard [42].
[j] JANAF tables [26].
[k] Blagojevic et al. [41].
[l] DeMaria et al. [40].

than the literature values of 6.92 ± 0.44 [16] or 6.95 ± 0.44 eV [26].

As noted above, there is no literature thermochemistry for HfC^+ and only very broad limits are available for TaC^+, 3.38 eV < $D(TaC^+)$ < 6.11 eV [46,47]. Our much more precise value of $D_0(Ta^+–C)$ = 3.79 ± 0.04 eV lies within these limits. For WC^+, the 0 K BDE derived from analysis of reaction (3) is 4.76 ± 0.09 eV, within experimental uncertainty of the 4.96 ± 0.22 eV value obtained from the $W^+ + CH_4$ reaction system [52]. A weighted average of the two values from our laboratory is $D_0(W^+–C)$ = 4.80 ± 0.08 eV, which we take as our best determination in this system. This value lies in between those derived from the appearance energies of WC^+ and W^+ observed in the photoionization of $W(CO)_6$ and W(CO), 3.93 ± 0.36 and 3.86 ± 0.35 eV, respectively [54,55], and that derived from electron impact of $W(CO)_6$, 5.26 ± 0.78 eV [53]. The latter value agrees with the determinations from this laboratory within the large uncertainty. The low values from photoionization can probably be attributed to the failure to account for kinetic shifts in the tight (for formation of WC^+) versus loose (for formation of W^+) transition states associated with these dissociation processes.

5.2. Theoretical results: Metal oxide cations

Qualitatively, the bonding in transition metal oxides has been discussed at length by Schroder et al. [20]. The valence orbitals are 1σ (largely O 2s), 2σ (metal–oxygen sigma bonding), 1π (metal–oxygen pi bonding), 1δ (metal 5d nonbonding), 3σ (largely metal 6s5d hybrid), 2π (metal–oxygen pi antibonding), and 4σ (metal–oxygen sigma antibonding). Configuration interaction between the 1σ and 2σ orbitals could drive the 2σ above the 1π, and the relative order of the 1δ and 3σ nonbonding orbitals is also unclear. For HfO^+, there are nine valence electrons, suggesting an electron configuration of $1\sigma^2 2\sigma^2 1\pi^4 1\delta^1$ with a predicted $^2\Delta$ ground state or $1\sigma^2 2\sigma^2 1\pi^4 3\sigma^1$ with a $^2\Sigma^+$ ground state. The present calculations find the latter is the ground state with the $^2\Delta$ state lying 0.90 eV higher in energy (Table S2). This is consistent with the ground state determined by ESR spectroscopy [22]. These states have similar bond lengths of 1.701 and 1.714 Å, respectively. Other excited states necessarily remove an electron from one of the bonding orbitals (2σ or 1π) such that they lie 2.9 eV or more above the ground state and have appreciably longer bonds (1.84–1.95 Å) (Table S2).

Addition of another electron in TaO^+ suggests possible ground states of $^3\Delta$ ($1\sigma^2 2\sigma^2 1\pi^4 3\sigma^1 1\delta^1$), $^3\Sigma^-$ ($1\sigma^2 2\sigma^2 1\pi^4 1\delta^2$), or possibly $^1\Sigma^+$ ($1\sigma^2 2\sigma^2 1\pi^4 3\sigma^2$). Indeed, the present calculations find a $^3\Delta$ ground state, with the lowest energy excited state being the singlet-coupled version of this state, $^1\Delta$ having the same electron configuration (Table S2). The $^1\Sigma^+$ state was located 0.82 eV higher in energy. The $^3\Sigma^-$ state lies at 0.86 eV, whereas the singlet-coupled version of this state was found 1.07 eV above the ground state. All other excited states involve excitations out of the bonding orbitals and therefore lie over 3.4 eV higher in energy than the ground state. All low-lying states have bond lengths near 1.67 Å, whereas the higher lying excited states have longer bonds (1.86–1.88 Å), consistent with a lower bond order.

For WO^+, the obvious ground state is now $^4\Sigma^-$ ($1\sigma^2 2\sigma^2 1\pi^4 3\sigma^1 1\delta^2$) and indeed this is found to be the ground state computationally. Low-lying excited states include the low-spin coupled version of this state, $^2\Sigma^-$ having the same electronic configuration, and $^2\Delta$ ($1\sigma^2 2\sigma^2 1\pi^4 3\sigma^2 1\delta^1$). These states lie 0.84 and 1.47 eV above the ground state and all three states have bond lengths of 1.64–1.65 Å. Somewhat higher in energy are two $^4\Pi$ states having $1\sigma^2 2\sigma^2 1\pi^4 1\delta^2 2\pi^1$ and $1\sigma^2 2\sigma^2 1\pi^3 3\sigma^2 1\delta^2$ configurations. These have longer bonds (1.70 and 1.84 Å, respectively) and lie 1.97 and 4.92 eV above the ground state. At a somewhat lower level of theory, B3LYP/HW/6-31G(d), Bohme and co-workers [41] found the $^4\Sigma^-$, $^2\Sigma^-$, and $^4\Pi$ states with excitation energies, 0.0, 0.8, and 2.0 eV, respectively, that agree nicely with those calculated here.

The calculated metal oxide cation bond energies (Table 2) are in good agreement with the experimental values. For HfO^+, these range from 7.04 (CCSD) to 7.54 (QCISD(T)) eV versus 6.91 ± 0.11 eV; for TaO^+, 7.22 (CCSD) to 7.84 (QCISD(T)) eV versus 7.10 ± 0.12 eV; and for WO^+, 6.60 (CCSD) to 7.11 (QCISD(T)) eV versus 6.77 ± 0.07 eV. Except for the CCSD result for WO^+, the computed bond energies are systematically higher than our experimental values, with mean absolute deviations (MADs) of only 0.14, 0.16, and 0.21 eV for CCSD, QCISD, and B3LYP values, respectively, somewhat larger than the experimental uncertainties. Addition of perturbative triple excitations, CCSD(T) and QCISD(T), increases the MADs for the three oxides somewhat to 0.48 and 0.57 eV, respectively. It should be realized that spin–orbit effects are not included in these theoretical values. Specifically, the 0 K experimental numbers should correspond to dissociation to the lowest spin–orbit state of the metal ion, whereas the theoretical numbers correlate with the average of all spin–orbit levels of the ground state of the metal ion (differences of 0.227, 0.466, and 0.514 eV for Hf^+, Ta^+, and W^+, respectively). However, correcting the theoretical BDEs by subtracting these excitation energies ignores spin–orbit coupling in the metal oxide ions, which

has been calculated to be as much as 0.56 eV for the TaC^+ molecule [48].

No matter the exact values, the experimental and theoretical BDEs clearly follow the same trends, i.e., $D(TaO^+) > D(HfO^+) > D(WO^+)$, with only small variations in the three values. This is consistent with the ground state electronic configurations of the three species, $^2\Sigma^+$ ($1\sigma^2 2\sigma^2 1\pi^4 3\sigma^1$), $^3\Delta$ ($1\sigma^2 2\sigma^2 1\pi^4 3\sigma^1 1\delta^1$), and $^4\Sigma^-$ ($1\sigma^2 2\sigma^2 1\pi^4 3\sigma^1 1\delta^2$), respectively, which all have a bond order of three and differ only in the occupation of the nonbonding 3σ and 1δ orbitals. Furthermore, coupling atomic O (^3P, $2s^2 2p^4$) with the ground state electronic configurations of the atomic metal ions, Ta^+ (^5F, $6s^1 5d^3$) and W^+ (^6D, $6s^1 5d^4$), leads directly to the ground states of TaO^+ and WO^+. However, Hf^+ (^2D, $6s^2 5d^1$) must promote to the ^4F ($6s^1 5d^2$) state lying 0.56 eV (average of all spin–orbit levels) above the ^2D state [68], which probably explains why the bond energy for HfO^+ is slightly weaker than that for TaO^+.

5.3. *Theoretical results: Metal carbide cations*

Qualitatively, the bonding in transition metal carbides should parallel that for the oxides fairly closely. The same valence orbitals are available, with two less valence electrons. For HfC^+, there are seven valence electrons, suggesting a ground state electron configuration of $1\sigma^2 2\sigma^2 1\pi^3$ ($^2\Pi$) or $1\sigma^2 2\sigma^1 1\pi^4$ ($^2\Sigma^+$). The present calculation finds the latter is the ground state ($r = 1.784$ Å), indicating that configuration interaction has moved the 2σ orbital above the 1π orbitals. Indeed, no state corresponding to the predicted $^2\Pi$ was ever located theoretically, although there are a multitude of low-lying excited states (Table S2). In most cases, an electron is removed from the 1π bonding orbital of the ground state leading to a longer bond length, $r > 1.90$ Å. Formation of the $^2\Sigma^+$ ($1\sigma^2 2\sigma^1 1\pi^4$) ground state cannot be achieved by diabatic coupling of atomic C (^3P, $2s^2 2p^2$) with the ground state of Hf^+ (^2D, $6s^2 5d^1$), but instead requires the Hf^+ (^4F, $6s^1 5d^2$) state lying 0.56 eV higher in energy (average of all spin–orbit levels) [68].

The TaC^+ molecule has been theoretically studied before by Majumdar and Balasubramanian (MB) [48] using the CASMCSCF level of theory followed by spin–orbit configuration interaction calculations. They find four low-lying states, $^1\Sigma^+$ ($1\sigma^2 2\sigma^2 1\pi^4$), $^3\Sigma^+$ ($1\sigma^2 2\sigma^1 1\pi^4 3\sigma^1$), $^3\Delta$ ($1\sigma^2 2\sigma^1 1\pi^4 1\delta^1$), and $^1\Delta$ ($1\sigma^2 2\sigma^1 1\pi^4 1\delta^1$), corresponding to adding a 2σ, 3σ, 1δ, and 1δ electron, respectively, to the ground state configuration of HfC^+. These states have relative energies of 0.0, 0.03, 0.43, and 0.51 eV, respectively, and are not greatly influenced by spin–orbit corrections. Bond lengths are 1.731, 1.739, 1.760, and 1.816 Å, respectively. Our B3LYP results are roughly similar with excitation energies for these states of 0.0, 0.08, 0.37, and 0.41 eV, respectively, and bond lengths of 1.718, 1.751, 1.747, and 1.758 Å. The 0 K adiabatic bond energy calculated by MB for their $^1\Sigma^+$ ground state was 4.50 eV (adjusted for the excited state asymptote used in the diabatic bond energy cited by MB), whereas our 0 K BDEs range from 4.32 to 4.88 eV (Table 2). It should be noted that there were some difficulties in the present single configuration calculations of the $^1\Sigma^+$ state, which can be attributed to mixing between $1\sigma^2 2\sigma^2 1\pi^4$ and $1\sigma^2 2\sigma^1 1\pi^4 3\sigma^1$ configurations and some spin contamination as a result of mixing with the low-lying $^3\Sigma^+$ state. At first glance, it seems odd that the $^1\Sigma^+$ state, which has a bond order of three, is not much lower in energy than the $^3\Sigma^+$, $^3\Delta$, and $^1\Delta$ states, which all have one less sigma bonding electron (bond order of 2.5). This is because the latter three states diabatically correlate with the Ta^+ (^5F, $6s^1 5d^3$) + C (^3P, $2s^2 2p^2$) ground state asymptote, whereas the $^1\Sigma^+$ state diabatically correlates with the Ta^+ (^3F, $6s^2 5d^2$) + C (^3P, $2s^2 2p^2$) asymptote, lying 0.43 eV higher in energy (average of all spin–orbit levels) [68].

For WC^+, the ground state is $^2\Delta$ ($1\sigma^2 2\sigma^2 1\pi^4 1\delta^1$), consistent with the qualitative bonding picture developed above. This has a short bond length of 1.687 Å, whereas most excited states have bond lengths in excess of 1.72 Å (Table S2). This can be attributed to the fact that these states involve moving an electron from the 2σ bonding orbital into a nonbonding orbital. Nevertheless, the excitation energies are modest, ranging from 0.32 to 1.16 eV (Table S2). The ground state configuration cannot be achieved by coupling atomic C (^3P, $2s^2 2p^2$) with the ground state of W^+ (^6D, $6s^1 5d^4$), a combination that leads to the $^4\Delta$ ($1\sigma^2 2\sigma^1 1\pi^4 3\sigma^1 1\delta^1$) and $^4\Sigma^-$ ($1\sigma^2 2\sigma^1 1\pi^4 1\delta^2$) excited states, among others. Instead, the $^2\Delta$ state correlates diabatically with W^+ (^4F, $6s^1 5d^4$), lying 1.074 eV higher in energy (average of all spin–orbit levels) [68].

For the carbides, the calculated and experimental BDEs do not agree as well as for the oxides (Table 2). The calculated BDEs for HfC^+, TaC^+, and WC^+ range from 3.25 (CCSD) to 3.67 (B3LYP), 4.32 (CCSD) to 4.88 (CCSD(T)), and 4.34 (QCISD(T)) to 4.88 (B3LYP) eV, respectively, compared to the experimental values of 3.19 ± 0.03, 3.79 ± 0.04, and 4.76 ± 0.09 eV, respectively. Again the theoretical values tend to lie above the experimental BDEs, with discrepancies generally a little larger than the oxides. Nevertheless the trends in the BDEs are similar in both the experimental and theoretical values. The calculated ground state electronic configurations of the three species, $^2\Sigma^+$ ($1\sigma^2 2\sigma^1 1\pi^4$), $^1\Sigma^+$ ($1\sigma^2 2\sigma^2 1\pi^4$), and $^2\Delta$ ($1\sigma^2 2\sigma^2 1\pi^4 1\delta^1$), respectively, have bond orders of 2.5, 3, and 3, which would suggest that the bond energies should be more comparable to those of the oxides. Instead, we note that the ratio of the WC^+ and WO^+ BDEs is approximately 2/3, suggesting that the carbide has only a double bond, which in turn indicates that the 2σ orbital is not strongly bonding. The earlier metal carbide cations of hafnium and tantalum have even weaker BDEs, which is at least partially attributable to the promotion energy arguments noted above.

5.4. *Potential energy surfaces for CO activation*

For the activation of CO ($^1\Sigma^+$) by all three metal cations, the first step is to form a MCO^+ intermediate having a linear, end-on structure. The observation of both MC^+ and MO^+ products suggests that activation of the CO bond has occurred to form a C–M^+–O intermediate at elevated energies. Calculated potential energy surfaces for these systems are shown in Fig. 4. Table S3 lists the geometries and energies of various stable states of the MCO^+ and CMO^+ species for all three metals calculated at the B3LYP/HW+/6-311+G(3df) level of theory.

Interaction of CO ($^1\Sigma^+$) with Hf^+(^2D) forms a $HfCO^+$ ($^4\Sigma^-$) intermediate having a linear, end-on structure at 1.12 eV below the reactants. Although formation of this complex is spin-forbidden, several excited states of this complex (including doublet spin states) are found to lie from 0.14 ($^2\Sigma^-$) to 5.21 ($^4\Pi$) eV higher in energy (Table S3). There are also several stable geometries in which the CO ligand is bound side-on, such that the C–Hf–O bond angle is near 30° (Table S3). The lowest of these is a $^4A''$ state lying 0.87 eV above $HfCO^+$ ($^4\Sigma^-$). Calculations indicate that the inserted $CHfO^+$ species has a $^4A''$ ground state that lies in a shallow well 1.32 eV above the ground state reactants (Fig. 4a). Thus, the calculations indicate that the HfC^+ and HfO^+ bonds are much stronger than the analogues in $CHfO^+$, a result that is not surprising as electron density must be shared in the two ligand complex. Excited $^2A''$, $^2A'$, and $^4A'$ states of the $CHfO^+$ species were also found lying 0.29, 1.08, and 2.68 eV higher in energy, respectively. Note that the $^4A'$ state has the longest Hf—O bond but the shortest Hf—C bond, whereas the $^2A'$ state has the reverse (Table S3). HfC^+ + O and HfO^+ + C products can be formed from the C–Hf^+–O intermediates and have experimental

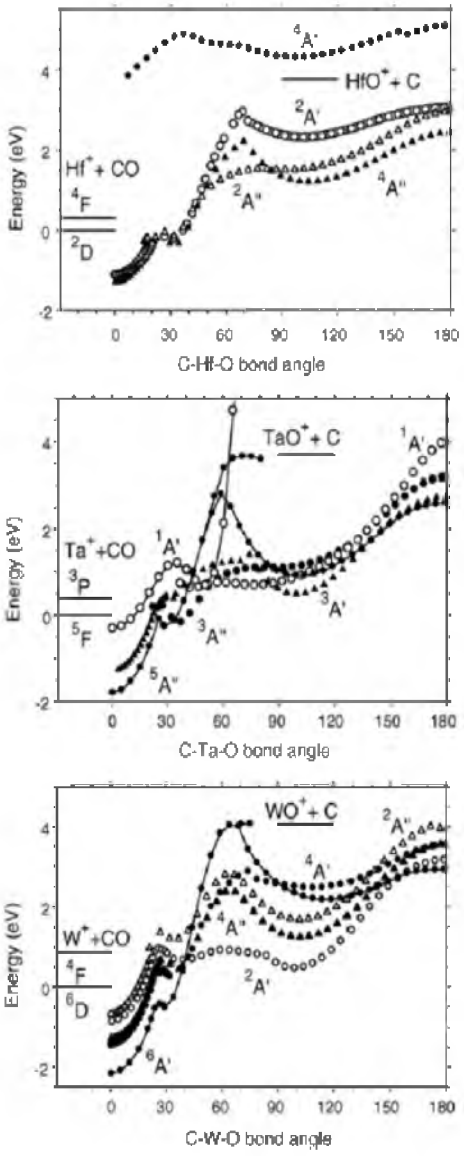

Fig. 4. Representative relaxed potential energy surface scans of the bond angle in the MCO^+ systems calculated at the B3LYP/HW+/6-311+G(3df) level without zero point energy corrections. Circles and triangles represent surfaces of A′ and A″ symmetry, respectively. Calculated energies of reactant (M^+ + CO) and product (MO^+ + C) asymptotes are indicated by horizontal bars to the left and middle, respectively.

endothermicities of 7.92 ± 0.03 eV and 4.20 ± 0.11 eV, respectively, relative to the entrance channel of $Hf^+ + CO$. The calculated potential energy surfaces (Fig. 4a) indicate that there are no barriers along the reaction paths in excess of the endothermicities of the reactions, which suggests that the thresholds measured experimentally should correspond to the thermodynamics of the product asymptotes, yielding accurate HfC^+ and HfO^+ bond energies.

Interaction of CO ($^1\Sigma^+$) with Ta^+(^{5}F) initially forms a $TaCO^+$($^5\Delta$) intermediate having a linear, end-on structure at 1.74 eV below the reactants. This species has several excited states ranging from 0.50 ($^1\Sigma^+$) to 2.14 ($^1\Sigma$) eV higher in energy (Table S3). The lowest energy side-on complex is a ^{5}A″ that lies 0.24 eV below reactants (Table S3). Calculations indicate that the inserted $CTaO^+$ species has a ^{3}A′ ground state that lies in a shallow well 0.49 eV above the reactants (Fig. 4b). Again because electron density must be shared in the two ligand complex, the bonds in $CTaO^+$ are weaker than in isolated TaC^+ and TaO^+ molecules. Excited ^{1}A′, ^{3}A″, ^{5}A′, and ^{5}A″ states of $CTaO^+$ were also found lying 0.19, 0.50, 3.14, and 4.02 eV higher in energy, respectively (Table S3). $TaC^+ + O$ and $TaO^+ + C$ products can be formed from the C–Ta^+–O intermediates and have experimental endothermicities of 7.32 ± 0.04 and 4.01 ± 0.12 eV, respectively, relative to the ground state entrance channel of Ta^+ (^{5}F) + CO. As for the hafnium system, no barriers along the reaction paths in excess of the endothermicities of the reactions (Fig. 4b) indicate that accurate thermodynamic information about the TaC^+ and TaO^+ products can be obtained from the present threshold measurements.

W^+(^{6}D) interacts with CO ($^1\Sigma^+$) to form a WCO^+($^6\Sigma^+$) intermediate having a linear, end-on structure at 2.09 eV below the reactants. Excited states of this species were also found ranging from 0.71 ($^4\Phi$) to 3.91 ($^6\Pi$) eV higher in energy (Table S3). Side-on complexes were also located and lie 0.49 eV below the reactants (^{6}A′) to 1.00 eV above (^{2}A″) (Table S3). Calculations indicate that the inserted CWO^+ species has a ^{2}A′ ground state that lies in a shallow well 0.47 eV above the reactants (Fig. 4c). Thus, the calculations indicate that the WC^+ and WO^+ bonds are much stronger than the analogues in CWO^+, again a result of sharing the bonding electrons on tungsten with both ligands. Excited ^{4}A′, ^{4}A″, ^{2}A″, ^{6}A′, and ^{6}A″ states of the CWO^+ intermediate were also found lying 0.28, 0.76, 1.20, 1.69, and 3.75 eV higher in energy, respectively (Table S3). It is found that the W—O bond length is roughly the same in all four states, whereas the W—C bond length tracks with increasing energy above the reactants (Table S3). $WC^+ + O$ and $WO^+ + C$ products can be formed from the C–W^+–O intermediates and have endothermicities of 6.35 ± 0.09 and 4.34 ± 0.07 eV, respectively, relative to the ground state entrance channel of $W^+ + CO$. No barriers along the reaction paths in excess of the endothermicities of the reactions are found (Fig. 4c), which means that the thresholds should correspond to the asymptotic energies of the products for both reactions.

The results for the potential energy surface in the tungsten system are in qualitatively good agreement with previous theoretical results on WCO^+ obtained by Musaev et al. [56], who calculated the lowest energy linear, side-on, and inserted species of sextet, quartet, and doublet spin. We find that the CWO^+ (^{2}A′) insertion species lies 2.57 eV above the linear WCO^+($^6\Sigma^+$) ground state species compared to 3.00 calculated by Musaev et al. These authors also calculated that the lowest lying quartet and doublet states (symmetries unspecified) lie above the sextet state of WCO^+ by 1.32 and 2.65 eV, respectively, compared to 0.71 and 1.30 eV, respectively, found here.

We did not explore the potential energy surface corresponding to approach of the metal cations with the oxygen end of the carbon monoxide molecule. The MOC^+ intermediates are anticipated to be much less stable than the corresponding MCO^+ species and could easily collapse to the side-on species identified above.

6. Summary

In this study, we are able to generate Hf^+, Ta^+, and W^+ ions in their ground states by using a direct current discharge/flow tube (DC/FT) ion source. Corresponding state-specific cross sections for these ions with D_2 and CO are obtained. The former reactions are all exothermic, whereas analyses of the endothermic reaction cross sections for the latter systems yield BDEs for the metal oxide and carbide cations listed in Table 2. These values include the first thermodynamic values for HfC^+ and TaC^+ and improved thermochemistry for WC^+ and the three metal oxide cations. In Table 3, the cationic BDEs for the oxides are combined with heats of formation of the neutral species taken from the literature to derive improved ionization energies of the neutral metal oxides, or in the case of TaO

and WO where the IE values are well determined, alternate values for the neutral heats of formation.

Detailed quantum calculations were also performed for the metal carbide and oxide diatoms examined experimentally. The nature of the bonding in MO^+ and MC^+ is analyzed using theoretical calculations at a B3LYP/HW+/6-311+G(3df) level of theory. Bond energies for all MO^+ and MC^+ species are calculated using geometries calculated at this level and single point energies determined at B3LYP, CCSD, CCSD(T), QCISD, and QCISD(T) levels of theory with the same basis set. Reasonable agreement between the theoretical and experimental bond energies for the three metal oxide and three metal carbide cations is found. Potential energy surfaces for reaction of the metal cations with CO are also calculated at the B3LYP/HW+/6-311+G(3df) level of theory and demonstrate that the reactions occur by insertion of the metal cation into the CO bond followed by loss of either the C or O neutral atom product, with no barriers in excess of the endothermicity.

Acknowledgement

This work is supported by the National Science Foundation, grant no. CHE-0748790.

Appendix A. Supplementary data

Supplementary data associated with this article can be found, in the online version, at doi:10.1016/j.ijms.2008.08.025.

References

[1] E.K. Stroms, in: J.L. Margrave (Ed.), Refractory Materials, vol. 2, Academic Press, New York, 1967.
[2] H. Silberbach, H.Z. Merz, Physica B 59 (1985) 143.
[3] K. Gesheva, E. Vlakhov, Mater. Lett. 5 (1987) 276.
[4] D. Smith, N.G. Adams, Plasma Chemistry I, Vol. 89 of Topics in Current Chemistry, Springer-Verlag, Berlin, 1980, p. 1.
[5] E. Murad, J. Geophys. Res. 83 (1978) 5525;
Tech. Rep. AFGL-TR-77-0235, Air Force Geophysics Laboratory, Hanscom Air Force Base, MA, 1977.
[6] R.A. Sheldon, in: D.H. Barton, A.E. Martell, D.T. Sawyer (Eds.), The Activation of Dioxygen and Homogeneous Catalytic Oxidation, Plenum, New York, 1993, p. 9;
R.A. Sheldon, J.K. Kochi, Metal-Catalyzed Oxidations of Organic Compounds, Academic, New York, 1981.
[7] S.K. Loh, E.R. Fisher, L. Lian, R.H. Schultz, P.B. Armentrout, J. Phys. Chem. 93 (1989) 3159.
[8] E.R. Fisher, J.L. Elkind, D.E. Clemmer, R. Georgiadis, S.K. Loh, N. Aristov, L.S. Sunderlin, P.B. Armentrout, J. Chem. Phys. 93 (1990) 2676.
[9] S.K. Loh, L. Lian, P.B. Armentrout, J. Chem. Phys. 91 (1989) 6148.
[10] Y.-M. Chen, P.B. Armentrout, J. Chem. Phys. 103 (1995) 618.
[11] M.R. Sievers, Y.-M. Chen, P.B. Armentrout, J. Chem. Phys. 105 (1996) 6322.
[12] X.-G. Zhang, P.B. Armentrout, J. Phys. Chem. A 107 (2003) 8904.
[13] K.P. Huber, G. Herzberg, Molecular Spectra and Molecular Structure. IV. Constants of Diatomic Molecules, Van Nostrand Reinhold, New York, 1979.
[14] M.B. Panish, L.J. Reif, Chem. Phys. 38 (1963) 253.
[15] R.J. Ackermann, E.G. Rauh, J. Chem. Phys. 60 (1974) 2266.
[16] J.B. Pedley, E.M. Marshall, J. Phys. Chem. Ref. Data 12 (1983) 967.
[17] J.B. Bhartiya, S.H. Bebere, Curr. Sci. 55 (1986) 383.
[18] E.G. Rauh, R.J. Ackermann, J. Chem. Phys. 60 (1974) 1396.
[19] C.L. Callender, P.A. Hackett, D.M. Rayner, J. Opt. Soc. Am. B 5 (1988) 1341.
[20] D. Schroder, H. Schwarz, S. Shaik, Struct. Bond. 97 (2000) 91.
[21] S.G. Lias, J.E. Bartmess, J.F. Liebman, J.L. Holmes, R.D. Levin, W.G. Mallard, J. Phys. Chem. Ref. Data 17 (Suppl. 1) (1988) 1.
[22] R.J. Vanzee, S. Li, W. Weltner, Chem. Phys. Lett. 217 (1994) 381.
[23] A. Hansson, A. Pettersson, P. Royen, U. Sassenberg, J. Mol. Spectrosc. 224 (2004) 157.
[24] R.S. Ram, P.F. Bernath, J. Mol. Spectrosc. 169 (1995) 268.
[25] L.A. Kaledin, J.E. McCord, M.C. Heaven, J. Mol. Spectrosc. 173 (1995) 37.
[26] M.W. Chase, Jr., J. Phys. Chem. Ref. Data, Monograph No. 9 (1963) 1.
[27] M.G. Inghram, W.A. Chupka, J. Berkowitz, J. Chem. Phys. 27 (1957) 569.
[28] O.H. Krikorian, J.H. Carpenter, J. Phys. Chem. 69 (1965) 4399.
[29] J. Drowart, A. Pattoret, S. Smoes, F. Degreve, D. Detry, in: W.L. Mead (Ed.), Advances in Mass Spectrometry, vol. 3, Inst. Petroleum, London, 1966, p. 931.
[30] S. Smoes, J. Drowart, C.E. Myers, J. Chem. Thermodyn. 8 (1976) 225.
[31] J.M. Dyke, A.M. Ellis, M. Feher, A. Morris, A.J. Paul, J.C.H. Stevens, J. Chem. Soc. Faraday Trans. 2 83 (1987) 1555.
[32] R.J. Ackermann, E.G. Rauh, R.J. Thorn, J. Chem. Phys. 65 (1976) 1027.
[33] B. Simard, P. Kowalczyk, A.M. James, Phys. Rev. 50 (1994) 846.
[34] W. Weltner, D. McLeod, J. Chem. Phys. 42 (1965) 882.
[35] C.J. Cheetham, R.F. Barrow, Trans. Faraday Soc. 63 (1967) 1835.
[36] R.S. Ram, P.F. Bernath, J. Mol. Spectrosc. 191 (1998) 125.
[37] A. Al-Khalili, U. Hallsten, O. Launila, J. Mol. Spectrosc. 198 (1999) 230.
[38] K.J. Manke, T.R. Vervoort, K.T. Kuwata, T.D. Varberg, J. Chem. Phys. 128 (2008) 104302.
[39] W.J. Zheng, X. Li, S. Eustis, K. Bowen, Chem. Phys. Lett. 460 (2008) 68.
[40] G. DeMaria, R.P. Burns, J. Drowart, M.G. Inghram, J. Chem. Phys. 32 (1960) 1373.
[41] V. Blagojevic, G.K. Koyanagi, V.V. Lavrov, G. Orlova, D.K. Bohme, Chem. Phys. Lett. 389 (2004) 303.
[42] M.D. Campbell-Miller, B. Simard, J. Opt. Soc. Am. B 13 (1996) 2115.
[43] R.S. Ram, J. Lievin, G. Li, T. Hirao, P.F. Bernath, Chem. Phys. Lett. 343 (2001) 437.
[44] M. Lorenz, V.E. Bondybey, Chem. Phys. 241 (1999) 127.
[45] M.W. Heaven, G.M. Stewart, M.A. Buntine, G.F. Metha, J. Phys. Chem. A 104 (2000) 3308.
[46] C.J. Cassady, S.W. McElvany, J. Phys. Chem. 94 (1990) 2057.
[47] C.J. Cassady, S.W. McElvany, J. Am. Chem. Soc. 112 (1990) 4188.
[48] D. Majumdar, K. Balasubramanian, Chem. Phys. Lett. 294 (1998) 273.
[49] K. Balasubramanian, J. Chem. Phys. 112 (2000) 7425.
[50] S.M. Sickafoose, A.W. Smith, M.D. Morse, J. Chem. Phys. 116 (2002) 993.
[51] X. Li, S.S. Liu, W. Chen, L.-S. Wang, J. Chem. Phys. 111 (1999) 2464.
[52] P.B. Armentrout, S. Shin, R. Liyanage, J. Phys. Chem. A 110 (2006) 1242.
[53] R.E. Winters, R.W. Kiser, Inorg. Chem. 4 (1965) 157.
[54] F. Qi, L. Sheng, H. Gao, Y. Zhang, X. Yang, S. Yang, S. Yu, Huaxue Wuli Xuebao 12 (1999) 525.
[55] F. Qi, S. Yang, L. Sheng, H. Gao, Y. Zhang, S. Yu, J. Chem. Phys. 107 (1997) 10391.
[56] D.G. Musaev, S. Irle, M.C. Lin, J. Phys. Chem. A 111 (2007) 6665.
[57] S.K. Loh, D.A. Hales, L. Lian, P.B. Armentrout, J. Chem. Phys. 90 (1989) 5466.
[58] R.H. Schultz, P.B. Armentrout, Int. J. Mass Spectrom. Ion Process. 107 (1991) 29.
[59] E. Teloy, D. Gerlich, Chem. Phys. 4 (1974) 417;
D. Gerlich, in: C.-Y. Ng, M. Baer (Eds.), State-Selected and State-to-State Ion-Molecule Reaction Dynamics. Part I. Experiment, vol. 82, Wiley, New York, 1992, p. 1 (Adv. Chem. Phys.).
[60] K.M. Ervin, P.B. Armentrout, J. Chem. Phys. 83 (1985) 166.
[61] P.J. Chantry, J. Chem. Phys. 55 (1971) 2746.
[62] B.L. Kickel, P.B. Armentrout, J. Am. Chem. Soc. 117 (1995) 4057.
[63] D.E. Clemmer, Y.-M. Chen, F.A. Khan, P.B. Armentrout, J. Phys. Chem. 98 (1994) 6522.
[64] C.L. Haynes, P.B. Armentrout, Organometallics 13 (1994) 3480.
[65] B.L. Kickel, P.B. Armentrout, J. Am. Chem. Soc. 117 (1995) 764.
[66] Y.-M. Chen, J.L. Elkind, P.B. Armentrout, J. Phys. Chem. 99 (1995) 10438.
[67] M.R. Sievers, Y.-M. Chen, P.B. Armentrout, J. Phys. Chem. 100 (1996) 54.
[68] C.E. Moore, Atomic Energy Levels, Natl. Bur. Stand. (U.S.) Circ. 467, Vol. III (1958), reprinted as Natl. Stand. Ref. Data Ser., Natl. Bur. Stand. (U.S.) 35 (1971).
[69] C.C. Kiess, J. Res. Natl. Bur. Stand. (U.S.) 66A (1962) 111.
[70] J.O. Ekberg, R. Kling, W. Mende, Phys. Scr. 61 (2000) 146.
[71] P.B. Armentrout, Int. J. Mass Spectrom. 200 (2000) 219.
[72] W.J. Chesnavich, M.T. Bowers, J. Phys. Chem. 83 (1979) 900.
[73] P.B. Armentrout, in: N.G. Adams, L.M. Babcock (Eds.), Advances in Gas Phase Ion Chemistry, 1, JAI, Greenwich, 1992, p. 83.
[74] F. Muntean, P.B. Armentrout, J. Chem. Phys. 115 (2001) 1213.
[75] M.E. Weber, J.L. Elkind, P.B. Armentrout, J. Chem. Phys. 84 (1986) 1521.
[76] A.D. Becke, J. Chem. Phys. 98 (1993) 5648.
[77] C. Lee, W. Yang, R.G. Parr, Phys. Rev. B 37 (1988) 785.
[78] Gaussian 03, Revision B.02, M.J. Frisch, G.W. Trucks, H.B. Schlegel, G.E. Scuseria, M.A. Robb, J.R. Cheeseman, J.A. Montgomery, Jr., T. Vreven, K.N. Kudin, J.C. Burant, J.M. Millam, S.S. Iyengar, J. Tomasi, V. Barone, B. Mennucci, M. Cossi, G. Scalmani, N. Rega, G.A. Petersson, H. Nakatsuji, M. Hada, M. Ehara, K. Toyota, R. Fukuda, J. Hasegawa, M. Ishida, T. Nakajima, Y. Honda, O. Kitao, H. Nakai, M. Klene, X. Li, J.E. Knox, H.P. Hratchian, J.B. Cross, V. Bakken, C. Adamo, J. Jaramillo, R. Gomperts, R.E. Stratmann, O. Yazyev, A.J. Austin, R. Cammi, C. Pomelli, J.W. Ochterski, P.Y. Ayala, K. Morokuma, G.A. Voth, P. Salvador, J.J. Dannenberg, V.G. Zakrzewski, S. Dapprich, A.D. Daniels, M.C. Strain, O. Farkas, D.K. Malick, A.D. Rabuck, K. Raghavachari, J.B. Foresman, J.V. Ortiz, Q. Cui, A.G. Baboul, S. Clifford, J. Cioslowski, B.B. Stefanov, G. Liu, A. Liashenko, P. Piskorz, I. Komaromi, R. L. Martin, D.J. Fox, T. Keith, M.A. Al-Laham, C.Y. Peng, A. Nanayakkara, M. Challacombe, P.M.W. Gill, B. Johnson, W. Chen, M.W. Wong, C. Gonzalez, J.A. Pople, Gaussian, Inc., Wallingford CT, 2004.
[79] P.J. Hay, W.R. Wadt, J. Chem. Phys. 82 (1985) 299.
[80] G. Ohanessian, M.J. Brusich, W.A. Goddard III, J. Am. Chem. Soc. 112 (1990) 7179.
[81] J.B. Foresman, A.E. Frisch, Exploring Chemistry with Electronic Structure Methods, Gaussian, Inc., Pittsburgh, PA, 1996.
[82] G. Gioumousis, D.P. Stevenson, J. Chem. Phys. 29 (1958) 294.
[83] E.W. Rothe, R.B. Bernstein, J. Chem. Phys. 31 (1959) 1619.
[84] G.K. Koyanagi, D. Caraiman, V. Blagojevic, D.K. Bohme, J. Phys. Chem. A 106 (2002) 4581.
[85] N. Aristov, P.B. Armentrout, J. Phys. Chem. 91 (1987) 6178.
[86] J.D. Burley, K.M. Ervin, P.B. Armentrout, Int. J. Mass Spectrom. Ion Process. 80 (1987) 153.
[87] T.M. Miller, B. Bederson, Adv. Atom. Mol. Phys. 13 (1977) 1.

CHAPTER 6

COLLISION-INDUCED DISSOCIATION OF MO^+ AND MO_2^+ (M = Ta, W): METAL OXIDE AND DIOXIDE CATION BOND ENERGIES

Christopher S. Hinton, Murat Citir, Manuel Manard, P. B. Armentrout

Reprinted from ***International Journal of Mass Spectrometry, Volume 308***, *Issues 2-3*
Christopher S. Hinton, Murat Citir, Manuel Manard, P. B. Armentrout, Collision-Induced Dissociation of MO^+ and MO_2^+ (M = Ta, W): Metal Oxide and Dioxide Cation Bond Energies, with permission from Elsevier

Contents lists available at ScienceDirect

International Journal of Mass Spectrometry

journal homepage: www.elsevier.com/locate/ijms

Collision-induced dissociation of MO^+ and MO_2^+ (M = Ta and W): Metal oxide and dioxide cation bond energies☆

Christopher S. Hinton[a], Murat Citir[a], Manuel Manard[b], P.B. Armentrout[a,*]

[a] Chemistry Department, University of Utah, 315 S. 1400 E. Rm 2020, Salt Lake City, UT 84112, United States
[b] National Security Technologies, LLC, Special Technologies Laboratory, 5520 Ekwill St., Santa Barbara, CA 93111, United States

ARTICLE INFO

Article history:
Received 17 May 2011
Received in revised form 14 June 2011
Accepted 16 June 2011
Available online 23 June 2011

Keywords:
Bond energies
Guided ion beam
Metal dioxides
Metal oxides
Tantalum
Tungsten

ABSTRACT

The collision-induced dissociation (CID) of TaO^+, WO^+, TaO_2^+, and WO_2^+ with Xe along with reactions of TaO^+ and WO^+ with O_2 are studied as a function of kinetic energy using guided ion beam tandem mass spectrometry in order to elucidate the thermochemistry of the MO_2^+ species. The kinetic energy dependences for the CID reactions show endothermic behavior, whereas the $MO^+ + O_2 \rightarrow MO_2^+ + O$ reactions proceed near the collision limit indicating exothermic processes. Analyses of the endothermic CID reaction cross sections yield 0 K threshold energies in eV of $E_0(Ta^+–O) = 7.01 \pm 0.12$, $E_0(W^+–O) = 6.72 \pm 0.10$, $E_0(OTa^+–O) = 6.08 \pm 0.12$, and $E_0(OW^+–O) = 5.49 \pm 0.09$. The nature of the bonding in MO^+ and MO_2^+ is discussed and compared for Ta and W and analyzed using theoretical calculations at the B3LYP/HW+/6-311+G(3df) level of theory. Bond energies for all MO^+ and MO_2^+ species are calculated using geometries calculated at this level as well as BHLYP and CCSD(T) levels and the Stuttgart–Dresden (SDD) and the Def2TZVPP basis sets. Reasonable agreement between the theoretical bond energies and experimental CID threshold energies for TaO^+, WO^+, TaO_2^+, and WO_2^+ is found. Potential energy surfaces for the reaction of the metal cations with O_2 are also calculated at the B3LYP level of theory and reveal additional information about the reaction mechanisms.

1. Introduction

The oxides of transition metals have properties that enable them to play vital roles in industrial, organometallic, and atmospheric chemistry [1–3]. In understanding the origins of these important properties, it can be useful to study the binding of the simplest examples of each species. Insight into the interaction of the metals and their oxides with O_2 can be obtained by examining reactions in the gas phase using a guided ion beam tandem mass spectrometer. The gas phase is an ideal arena for detailed study of the energetics of bond-making and bond-breaking processes at a molecular level. Because metal supports and interactions are absent, quantitative thermodynamic and intrinsic mechanistic information for various bond activation processes can be obtained.

Our group has previously used guided ion beam tandem mass spectrometry to study diatomic metal monoxide cations, MO^+, of the first-row [4–12], second-row [6,10,13–18], transition metals and other metals [10,19–21], but as yet have examined only a few third-row transition metals [22–24]. Likewise, our work has encompassed fewer studies of metal dioxide cations, MO_2^+, which include first-row [10,11], second-row [10,15–18], third-row [25] transition metals, and other metal cations [10]. In the present study, we extend these studies to the third-row transition metal ions, tantalum and tungsten. Using guided ion beam tandem mass spectrometry, we obtain the kinetic energy dependences of both exothermic and endothermic processes involving these species. Analyses of such data provide experimental thermochemistry that can be used as benchmarks for comparison with theoretical models of the structure of the metal oxides and dioxides.

Previous thermodynamic information on the monoxide and dioxide cations of tantalum and tungsten originates from several sources and is summarized in Table 1. In our laboratory, we have examined the endothermic reaction of Ta^+ with CO, yielding the bond dissociation energy (BDE) of $Ta^+–O$ as 7.10 ± 0.12 eV [23]. This value agrees nicely with 7.18 ± 0.14 as derived using Eq. (1)

$$D(M–O) + IE(M) = D(M^+–O) + IE(MO) \quad (1)$$

and the values IE(Ta) = 7.5495 eV [26], $D_0(TaO) = 8.24 \pm 0.13$ eV from Pedley and Marshall [27], and IE(TaO) = 8.61 ± 0.02 eV from a photoelectron experiment of Dyke et al. [28] (see [23] for further details). These values contrast with that listed in a review by Schröder et al. [29], $D(Ta^+–O) = 8.15 \pm 0.65$ eV, taken from information in the GIANT compilation [30], which uses older values for IE(Ta) = 7.40 eV [31] and IE(TaO) = 7.92 ± 0.1 eV [32], along with $\Delta_f H_0(TaO) = 2.08 \pm 0.65$ eV [33], and also

☆ In honor of John R. Eyler's many contributions to ion chemistry and spectroscopy.

* Corresponding author. Tel.: +1 801 581 7885; fax: +1 801 581 8433.
E-mail address: armentrout@chem.utah.edu (P.B. Armentrout).

Table 1
Experimental thermochemical data for tantalum and tungsten oxides and dioxides.

M^+–O	IE(M)	D_0(M–O)	IE(MO)	$D_0(M^+–O)$	
				Literature	This work
Ta^+–O	7.5495[a]	8.16 ± 0.12[b] 8.24 ± 0.13[c] 8.4 ± 0.5[d] 8.65 ± 0.65[e]	8.69 ± 0.18,[b] 8.61 ± 0.02[f] 7.92 ± 0.1,[g] 7.5 ± 0.5[h] 6 ± 0.5,[d] 8.70 ± 0.17[i]	7.10 ± 0.12[b] 7.18 ± 0.14[a,c,f] 8.15 ± 0.65[j]	7.01 ± 0.12
W^+–O	7.864[k]	7.01 ± 0.31[b] 6.92 ± 0.44[l] 6.95 ± 0.44[l]	8.04 ± 0.45,[b] 8.1 ± 0.3,[m] 9.1 ± 1,[n] 7.19 ± 0.32[i]	6.77 ± 0.07[b] 6.68 ± 0.53[e,k,m] 7.16 ± 0.43[m] 5.46 ± 0.43[l]	6.72 ± 0.10
OTa$^+$–O		6.87 ± 0.23[h] 6.61 ± 0.92[d,l]	8.5 ± 0.5,[h] 9 ± 0.5[d] 9.54 ± 0.32[o]	6.07 ± 1.05[l] 6.73 ± 0.80[d,l]	6.08 ± 0.12
OW^+–O		6.15 ± 0.53[l]	9.6 ± 0.3,[p] 9.5 ± 0.5,[q] 9.9 ± 1.0,[g] 9.8,[r] 9.9 ± 0.6[n] 8.76 ± 0.69[s]	5.72 ± 1.17[l] 4.6$_5$ ± 0.7[l,m,o]	5.49 ± 0.09

[a] Simard et al. [26].
[b] Armentrout et al. [23].
[c] Pedley and Marshall [27].
[d] Ingram et al. [37].
[e] Lias et al. (GIANT Tables) [30].
[f] Dyke et al. [28].
[g] Ackermann et al. [32].
[h] Smoes et al. [38].
[i] This work.
[j] Schröder et al. [29].
[k] Campbell-Miller and Simard [35].
[l] JANAF tables [33].
[m] Blagojevic et al. [34], corrected to 0 K.
[n] DeMaria et al. [36].
[o] Gusarov et al. [39].
[p] Balducci et al. [40].
[q] Yamdagni et al. [41].
[r] Drowart et al. [42].

leads to D_0(TaO) = 8.65 ± 0.65 eV. Likewise, we have previously measured the W^+–O BDE as 6.77 ± 0.07 eV from the endothermic reaction of W^+ with CO [23]. Again this agrees well with $D_0(W^+–O)$ = 6.68 ± 0.53 eV calculated using Eq. (1) and D_0(WO) = 6.92 ± 0.44 eV from Pedley and Marshall [27]. IE(WO) = 8.1 ± 0.3 eV measured by Böhme and co-workers [34], along with IE(W) = 7.864 eV [35]. As for TaO^+, this value disagrees with that quoted by Schröder et al. [29] of $D(W^+–O)$ = 5.46 ± 0.43 eV derived from information in the GIANT compilation [30], which uses IE(W) = 7.60 eV [31], IE(WO) = 9.1 ± 1 eV [36], and $\Delta_f H_0$(WO) = 4.41 ± 0.43 eV [33], and also leads to D_0(WO) = 6.95 ± 0.44 eV. Böhme and co-workers [34] also determined that W^+ reacts with COS to form WO^+ at room temperature with an efficiency of 0.38. They took this to indicate that $D_{298}(W^+–O) > D_{298}$(O–CS) = 6.85 ± 0.04 eV, which they combined with $D_{298}(W^+–O)$ = 6.81 ± 0.82 eV to yield a refined range of values that they cited as $D_{298}(W^+–O)$ = 7.20 ± 0.43 eV. This value can be adjusted to $D_0(W^+–O)$ = 7.16 ± 0.43 eV, Table 1.

Literature information on the dioxides of Ta^+ and W^+ is less plentiful. Bond energies and ionization energies of the metal monoxides and dioxides can be related according to the thermochemical cycle of Eq. (2) and can be used to provide some information from the literature.

$$D(OM - O) + IE(MO) = D(OM^+ - O) + IE(MO_2) \quad (2)$$

The review by Schröder et al. lists $D_0(OTa^+–O)$ = 6.07 eV and $D_0(OW^+–O)$ = 5.72 eV and cites the GIANT compilation. (Actually [30] contains no information about TaO_2^+, and the information in the GIANT compilation used to derive the WO_2^+ BDE indicates this value has an uncertainty of at least 1.17 eV, Table 1.) Heats of formation taken from the JANAF tables [33], which are based on Knudsen cell studies of Ingram et al. [37] provide D_0(OTa–O) as 6.61 ± 0.92 eV and this has also been measured as 6.87 ± 0.23 eV using the mass spectrometric Knudsen cell method [38]. The bond energy of 6.07 eV for $OTaO^+$ may have been obtained by combining the former neutral bond energy with IE(TaO) = 7.92 ± 0.1 eV [32] and IE(TaO_2) = 8.5 ± 0.5 [38], indicating it should have an uncertainty of 1.05 eV, Table 1. Alternatively, we can combine IE(TaO) = 8.61 ± 0.02 eV [28] and IE(TaO_2) values of 8.5 ± 0.5 [38] and 9 ± 0.5 eV [37] with the more precise D_0(OTa–O) = 6.87 ± 0.23 eV to obtain $D(OTa^+–O)$ values of 6.98 ± 0.55 and 6.48 ± 0.55 eV, which we cite in Table 1 as 6.73 ± 0.80 eV given that neither IE(TaO_2) value is precise. (Note that many of the literature IEs were determined solely to ascertain whether the species being probed were fragments or molecular species, hence their accuracy is questionable.) For WO_2, heats of formation given in the JANAF tables indicate the neutral OW–O bond energy is 6.15 ± 0.53 eV [33]. IE(WO_2) has been reported as 9.6 ± 0.3 [39], 9.5 ± 0.5 [40], 9.9 ± 1.0 [41], 9.8 [42], and 9.9 ± 0.6 eV [36]. Along with IE(WO) = 8.1 ± 0.3 eV [34] and D(OW–O), these IEs can be combined to indicate that $D(OW^+–O)$ is anywhere between 3.4 and 5.4 eV, with the most precise IE(WO_2) value suggesting $D(OW^+–O)$ = 4.6$_5$ ± 0.7 eV. Finally, there have been a few spectroscopic studies in which the ground state of TaO_2^+ has been identified as $^1A_1$ [43–45].

2. Experimental and computational section

2.1. General procedures

The guided ion beam tandem mass spectrometer on which these experiments were performed has been described in detail previously [46]. Briefly, MO^+ and MO_2^+ ions are generated in a direct current discharge flow tube (DC/FT) source described below [47], extracted from the source, accelerated, and focused into a magnetic sector momentum analyzer for mass selection of primary

ions. The mass-selected ions are decelerated to a desired kinetic energy and focused into an octopole ion beam guide that uses radio-frequency electric fields to trap the ions in the radial direction and ensure complete collection of reactant and product ions [48,49]. The octopole passes through a static gas cell with an effective length of 8.26 cm that contains the reaction partner at a low pressure (usually less than ~0.3 mTorr) so that multiple ion–molecule collisions are improbable. All results reported here result from single bimolecular encounters, as verified by pressure dependence studies. The unreacted parent and product ions are confined radially in the guide until they drift to the end of the octopole where they are extracted, focused, and passed through a quadrupole mass filter for mass analysis of products. Ions are subsequently detected with a secondary electron scintillation ion detector [50] using standard pulse counting techniques. Reaction cross sections are calculated from product ion intensities relative to reactant ion intensities after correcting for background signals [51]. Uncertainties in absolute cross sections are estimated to be ±20%.

The kinetic energy of the ions is varied in the laboratory frame by scanning the dc bias on the octopole rods with respect to the potential of the ion source region. Laboratory (lab) ion energies are converted to energies in the center-of-mass frame (CM) by using the formula $E_{CM} = E_{lab}\, m/(m+M)$, where m and M are the neutral and ionic reactant masses, respectively. Two effects broaden the cross section data: the kinetic energy distribution of the reactant ion and the thermal motion of the neutral reactant gas (Doppler broadening) [52]. The absolute zero and the full width at half maximum (FWHM) of the kinetic energy distribution of the reactant ions are determined using the octopole beam guide as a retarding potential analyzer, as described previously [51]. The distributions of ion energies, which are independent of energy, are nearly Gaussian and have a typical FWHM of 0.45–0.64 eV (lab) in these studies. Uncertainties in the absolute zero of the energy scale are ±0.05 eV (lab).

2.2. Ion source

M^+ (M = Ta and W) ions are produced in a DC/FT source, consisting of a cathode held at a high negative voltage (1.3–2.0 kV) over which a flow of approximately 90% He and 10% Ar passes at a total pressure of 0.3–0.5 Torr. The dc-discharge ionizes Ar and then accelerates these ions into the cathode made of either tantalum or tungsten metal, thereby sputtering atomic metal cations. MO^+ and MO_2^+ ions are produced through the reaction of M^+ with N_2O by introducing the reactant gas 15 cm downstream of the discharge zone in the flow tube at a pressure of ~2 mTorr. These ions undergo ~10^5 thermalizing collisions with He and ~10^4 collisions with Ar along the flow tube before entering the guided ion beam apparatus. These collisions with the He/Ar flow gas stabilize and thermalize the ions both rotationally and vibrationally. In general, we assume that these ions are in their ground electronic state and that the internal energy of these molecular ions is well described by a Maxwell–Boltzmann distribution of rotational and vibrational states corresponding to 300 K, the temperature of the flow tube. Previous studies from this laboratory have shown that these assumptions are consistent with the production of thermalized molecular ions under similar conditions [53–57].

2.3. Data analysis

The cross sections of endothermic reactions are modeled using Eq. (3) [58–63]

$$\sigma(E) = \frac{\sigma_0 \Sigma g_i (E + E_i - E_0)^n}{E} \qquad (3)$$

where σ_0 is an energy-independent scaling factor, E is the relative kinetic energy of the reactants, n is an adjustable parameter that characterizes the energy dependence of the process [61], and E_0 is the 0 K threshold for reaction of electronic, vibrational, and rotational state reactants. The model involves an explicit sum of the contributions of individual rovibrational states of the MO^+ and MO_2^+ reactant, denoted by i, having energies E_i and populations g_i. Before comparison with the experimental data, Eq. (3) is convoluted with the kinetic energy distributions of the reactant ions and neutral reactants at 300 K. The σ_0, n, and E_0 parameters are then optimized using a nonlinear least-squares analysis to give the best reproduction of the data [51]. Error limits for E_0 are calculated from the range of threshold values for different data sets over a range of acceptable n values combined with the absolute errors in the kinetic energy scale and internal energies of reactant ions.

2.4. Theoretical calculations

To establish the character of the molecular orbitals of the metal oxides and dioxides, quantum chemistry calculations were carried out with the B3LYP hybrid density functional method [64,65] and performed with the GAUSSIAN 09 suite of programs [66]. Ta and W are described using a basis set for Ta and W from Ohanessian et al. [67], which is based on the relativistic effective core potentials (ECP) of Hay–Wadt (HW) [68], equivalent to the Los Alamos ECP (LANL2DZ) basis set. Whereas the HW–ECP is optimized for neutral atoms, the altered basis set of Ohanessian et al. (HW+) accounts for differential contraction of the s orbitals compared to d orbitals induced by the positive charge. Calculations of thermochemistry and potential energy surfaces (relaxed potential energy surface scans) were conducted using a 6-311+G(3df) basis set for oxygen. We also examined results calculated using Def2TZVPP, a balanced basis set of triple zeta quality plus polarization for both elements [69], as well as the Stuttgart–Dresden (SDD) basis set [70] on the metal (retaining the 6-311+G(3df) basis on oxygen). The Def2TZVPP basis set includes f and g type polarization functions on Ta and W, whereas neither the HW+ nor SDD basis sets do. Both the Def2TZVPP and SDD basis set use ECPs developed by Andrae et al. for Ta and W [70]. In all cases, the thermochemistry calculated here is corrected for zero-point energies after scaling the vibrational frequencies by 0.9804 [71].

As a point of comparison, the calculated BDEs of O–O are 5.279 and 5.265 eV as calculated using the 6-311+G(3df) and Def2TZVPP basis sets compared to the experimental value of 5.115 eV [72]. In addition, the experimental ^3F excitation energy of Ta^+ (averaged over all spin–orbit levels) is 0.43 eV higher than the ^5F ground state (where the spin–orbit average is 0.47 eV above the ground level of $J = 1$) [73]. This experimental value can be compared to the excitation energies calculated at the B3LYP level using the HW+, SDD, and Def2TZVPP basis set of 0.40, 0.81, and 0.47 eV, respectively. For W^+, the experimental excitation energies of the ^6S and ^4F states are 0.41 and 1.07 eV, respectively, relative to the ^6D state (where the spin–orbit average lies 0.51 eV above the ground $J = 1/2$ level) [74]. The calculated B3LYP excitation energies with the HW+, SDD, and Def2TZVPP basis sets are 0.54, 0.44, and 0.51 eV for the ^6S excitation and 0.86, 0.88, and 0.82 eV for the ^4F excitation.

3. Experimental and theoretical results

3.1. CID of MO^+ with Xe

Cross sections for the interaction of TaO^+ and WO^+ with Xe were measured and are shown in Fig. 1. The products observed

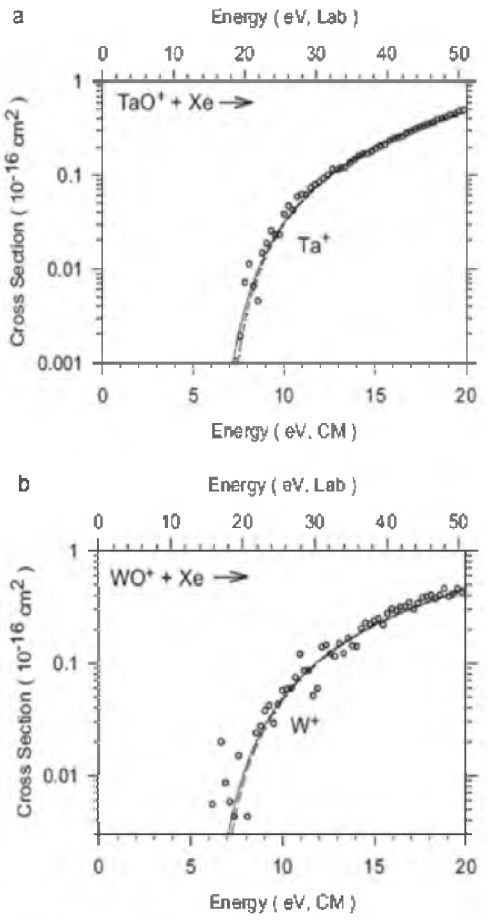

Fig. 1. Cross sections for collision-induced dissociation of TaO^+ (part a) and WO^+ (part b) with Xe as a function of kinetic energy in the center-of-mass frame (lower axis) and laboratory frame (upper axis). The best fits to the data (open circles) using Eq. (3) with parameters in Table 2 are shown as dashed lines. The solid lines show these models convoluted over the kinetic and internal energy distributions of the neutral reactant and ion.

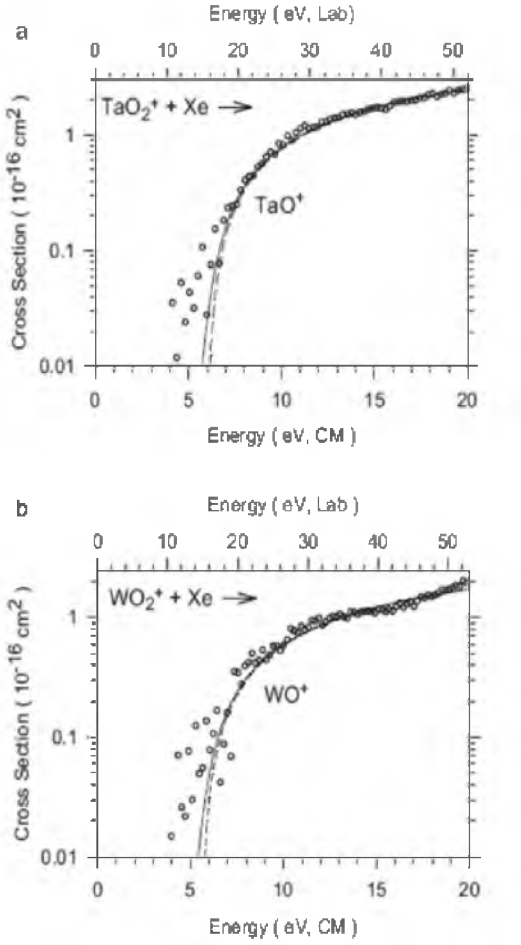

Fig. 2. Cross sections for collision-induced dissociation of $OTaO^+$ (part a) and OWO^+ (part b) with Xe as a function of kinetic energy in the center-of-mass frame (lower axis) and laboratory frame (upper axis). The best fits to the data (open circles) using Eq. (3) with parameters in Table 2 are shown as dashed lines. The solid lines show these models convoluted over the kinetic and internal energy distributions of the neutral reactant and ion.

correspond to reaction (4), a simple collision-induced dissociation process.

$$MO^+ + Xe \rightarrow M^+ + O + Xe \quad (4)$$

The cross section data for reaction (4) are analyzed using Eq. (3), and the fitting parameters obtained are listed in Table 2. The model reproduces the experimental data up to ~20 eV with thresholds of 7.01 ± 0.12 and 6.72 ± 0.10 eV for TaO^+ and WO^+, respectively. The threshold for CID can equal the M^+–O BDE as long as the interaction of M^+ with O is attractive everywhere, i.e., there are no barriers in excess of the asymptotic dissociation energy, and the dissociation produces ground state products. The former condition is almost certainly true here because the interaction of M^+ with O should be attractive at both long-range and short-range

Table 2
Fitting parameters of Eq. (3) used to model reactions (4) and (5).

Reactant	Product	σ_0	n	E_0 (eV)
TaO^+	Ta^+	0.03 ± 0.01	2.3 ± 0.2	7.01 ± 0.12
WO^+	W^+	0.03 ± 0.01	2.4 ± 0.2	6.72 ± 0.10
TaO_2^+	TaO^+	0.91 ± 0.05	1.4 ± 0.1	6.08 ± 0.12
WO_2^+	WO^+	0.63 ± 0.13	1.5 ± 0.1	5.49 ± 0.09

[58,60,75,76]. The latter condition is generally true when the dissociation pathway conserves spin, as it does here for the reactions $TaO^+(^3\Delta) \rightarrow Ta^+(^5F) + O(^3P)$ and $WO^+(^4\Sigma^-) \rightarrow W^+(^6D) + O(^3P)$. The CID thresholds of 7.01 ± 0.12 and 6.72 ± 0.10 eV for TaO^+ and WO^+ are in good agreement with the previously measured thermochemistry, Table 1. This may be somewhat serendipitous because CID experiments on strongly bound species with few internal degrees of freedom are sometimes found to measure only an upper limit to the thermodynamic BDE because of inefficiencies in the transfer of kinetic to internal energy in the collision process [14,57].

3.2. CID of MO_2^+ with Xe

Cross sections for the interaction of Xe with TaO_2^+ and WO_2^+ are shown in Fig. 2. The products observed correspond to reaction (5).

$$MO_2^+ + Xe \rightarrow MO^+ + O + Xe \quad (5)$$

The cross section data for reaction (5) are analyzed using Eq. (3), and the fitting parameters obtained are listed in Table 2. For both processes, the model of Eq. (3) reproduces these cross sections well up to 20 eV. As for the monoxides, the threshold for CID can

equal the OM^+–O BDE as long as there are no barriers in excess of the asymptotic dissociation energy and the dissociation produces ground state products, here $TaO^+(^3\Delta)$, $WO^+(^4\Sigma^-)$, and $O(^3P)$, in spin allowed reactions. In both cases, the CID thresholds of 6.08 ± 0.12 and 5.49 ± 0.09 eV are in good agreement with the previous thermochemistry in Table 1, but are much more precise.

We also looked for but did not observe formation of M^+ for either TaO_2^+ or WO_2^+. This behavior contrasts with previous results for the CID of PtO_2^+ with Xe [25], which produces both PtO^+ and the bare Pt^+ ion. An explanation for this was offered by Bohme and co workers [34] and relies on distinguishing between two cases according to whether the $MO^+ + O$ dissociation limit lies above or below the $M^+ + O_2$ dissociation limit. When $D_0(MO^+) > D_0(O_2)$, the $MO^+ + O$ dissociation limit lies below the $M^+ + O_2$ dissociation limit and exclusive loss of O is observed. When $D_0(MO^+) < D_0(O_2)$, the $MO^+ + O$ dissociation limit lies above the $M^+ + O_2$ dissociation limit and loss of O_2 is observed, in competition with the entropically favored loss of O at higher energies. Ta and W fall into the former category, and Pt falls into the latter.

3.3. Reaction of MO^+ with O_2

Cross sections for the reaction of MO^+ with O_2 are shown in Fig. 3. The products observed correspond to the exothermic reaction (6),

$$MO^+ + O_2 \rightarrow MO_2^+ + O \tag{6}$$

The TaO_2^+ and WO_2^+ cross sections decrease with increasing kinetic energy, consistent with the behavior expected for barrierless exothermic ion-molecule reactions. This behavior can be described using the Langevin–Gioumousis–Stevenson (LGS) model [77], Eq. (7),

$$\sigma_{LGS} = \pi e \left(\frac{\alpha}{2\pi\varepsilon_0 E} \right)^{1/2} \tag{7}$$

where e is the charge on the electron, α is the polarizability volume of the neutral reactant molecule (1.57 Å^3 for O_2 [78]), and ε_0 is the permittivity of vacuum. As can be seen from Figure 3, the cross sections for both M = Ta and W have energy dependences of $E^{-0.5\pm0.1}$ at the lowest energies, as predicted by σ_{LGS}, with magnitudes approximately equivalent to σ_{LGS} in this energy range (within the 20% absolute uncertainty), indicating that the reactions occur with near unit efficiency. The reaction cross sections can also be converted into a room temperature rate constant using methods outlined previously [46,51]. For TaO^+ and WO^+, this yields rate constants of (6.1 ± 1.2) and $(5.7 \pm 1.1) \times 10^{-10}$ cm^3 molecule^{-1} s^{-1}, respectively, compared to $k_{LGS} = 5.6 \times 10^{-10}$ cm^3 molecule^{-1} s^{-1}. These values compare favorably with the rate constants measured by Bohme and co-workers [34] in 0.35 Torr of helium at 295 K, (4.0 ± 1.2) and $(4.6 \pm 1.4) \times 10^{-10}$ cm^3 molecule^{-1} s^{-1}, respectively, corresponding to reaction efficiencies of 71 ± 21 and $82 \pm 25\%$.

Above about 0.3 eV, the cross sections begin to decrease more rapidly, approximately as $E^{-1.0\pm0.1}$. This effect can be attributed to angular momentum conservation constraints, as previously discussed in detail [56,79]. This argument recognizes that because the reduced mass of the products of reaction (6), μ', is smaller than that of the reactants, μ (μ'/μ is approximately 0.5 in these systems), the centrifugal barrier in the product channel can exceed that in the reactant channel for large angular momenta. This restricts the probability of reaction at higher kinetic energies, in essence by making it more favorable for the MO_3^+ intermediate to dissociate back to reactants compared to going on to products. We have previously outlined a simple model to predict where these angular momentum constraints can restrict the product formation in exothermic reactions [56]. This begins at an energy given by Eq. (8),

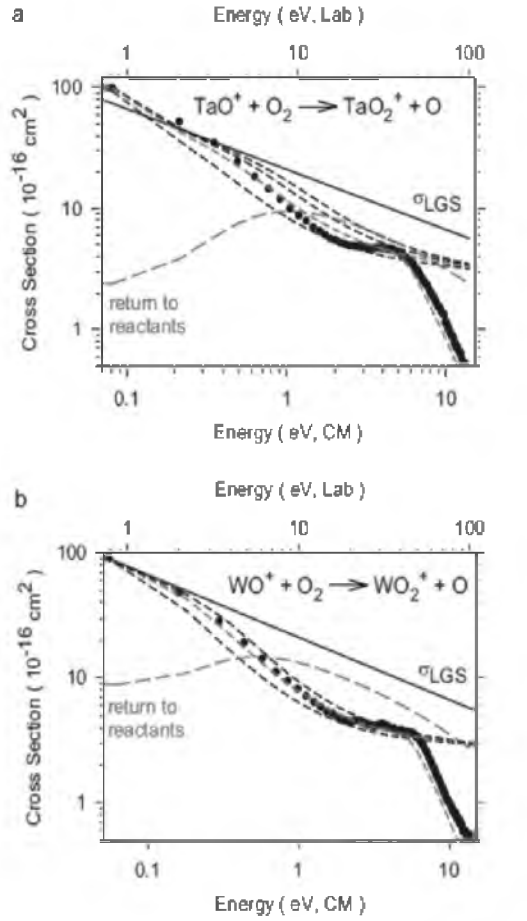

Fig. 3. Cross sections for reactions of TaO^+ (part a) and WO^+ (part b) with O_2 as a function of kinetic energy in the center-of-mass frame (lower x-axis) and laboratory frame (upper x-axis). The full line shows the theoretical collision cross section, σ_{LGS}. Dashed lines show the predictions of phase space theory for exothermicities of 0.4, 0.6 (in red), 0.8, and 1.0 eV (bottom to top) in part a and 0.3, 0.4 (in red), and 0.5 eV (bottom to top) in part b. (For interpretation of the references to color in this figure legend, the reader is referred to the web version of this article.) The cross section for the "return to reactants" is also shown for exothermicities of 0.6 and 0.4 in parts a and b, respectively.

$$E_c = \frac{(E - \Delta H)(\alpha'\mu'^2)}{(\alpha\mu^2)} \tag{8}$$

where α and α' are the polarizability volumes of the reactant and product neutrals (1.57 and 0.80 Å^3, respectively [78,80]), E is the relative kinetic energy of the reactants, and ΔH is the enthalpy of reaction. Using thermochemistry obtained above for TaO_2^+ and WO_2^+, this model predicts that the TaO_2^+ and WO_2^+ cross sections will become constrained beginning at 0.17 ± 0.02 and 0.07 ± 0.02 eV, respectively, in reasonable agreement with the data.

A more precise way of examining this same phenomenon is to calculate the expected cross section using phase space theory (PST), performed using modified versions of programs originally developed by Chesnavich and Bowers [81]. These calculations assume that the potential interaction for the bimolecular reactants and products are ion-induced dipole attractions, i.e., the LGS cross section of Eq. (7) for the reactants, and then explicitly conserves both energy and angular momentum. The results for several assumed

Table 3
Theoretical results for MO$^+$ calculated at the B3LYP/HW+/6-311+G(3df) level.

Species	State	$s(s+1)$[a]	Configuration	Energy (E_h)	Zero point energy (E_h)	E_{rel} (eV)	r(M–O) (Å)
O	^3P			−75.090915			
Ta$^+$	^5F	6.00	$6s^15d^3$	−57.362276		0.000	
	^3P	2.83[a]	$6s^25d^2$	−57.347516		0.402	
TaO$^+$	$^3\Delta$	2.01	$1\sigma^22\sigma^21\pi^43\sigma^11\delta^1$	−132.722996	0.002419	0.000	1.672
	$^1\Delta$	1.00[a]	$1\sigma^22\sigma^21\pi^43\sigma^11\delta^1$	−132.701893	0.002441	0.575	1.668
	$^1\Sigma^+$	0.00	$1\sigma^22\sigma^21\pi^43\sigma^2$	−132.693091	0.002493	0.816	1.665
	$^3\Sigma^-$	2.01	$1\sigma^22\sigma^21\pi^41\delta^2$	−132.691392	0.002342	0.858	1.679
	$^1\Sigma^-$	1.00[a]	$1\sigma^22\sigma^21\pi^41\delta^2$	−132.683503	0.002359	1.073	1.677
	$^5\Pi$	6.00	$1\sigma^22\sigma^21\pi^33\sigma^11\delta^2$	−132.595267	0.001723	3.457	1.881
	$^3\Pi$	2.78[a]	$1\sigma^22\sigma^21\pi^33\sigma^11\delta^2$	−132.583770	0.001748	3.770	1.873
	$^3\Phi$	2.01	$1\sigma^22\sigma^21\pi^33\sigma^21\delta^1$	−132.573944	0.001782	4.039	1.865
W$^+$	^6D	8.75	$6s^15d^4$	−67.345887		0.000	
	^6S	8.75	$6s^05d^5$	−67.326103		0.538	
	^4F	3.75	$6s^15d^4$	−67.314176		0.863	
WO$^+$	$^4\Sigma^-$	3.78	$1\sigma^22\sigma^21\pi^43\sigma^11\delta^2$	−142.693739	0.002479	0.000	1.648
	$^2\Gamma$	1.75[a]	$1\sigma^22\sigma^21\pi^43\sigma^11\delta^2$	−142.662911	0.002533	0.840	1.642
	$^2\Sigma^-$	1.75[a]	$1\sigma^22\sigma^21\pi^43\sigma^11\delta^2$	−142.651493	0.002537	1.151	1.642
	$^2\Delta$	0.76	$1\sigma^22\sigma^21\pi^43\sigma^21\delta^1$	−142.639796	0.002543	1.470	1.644
	$^4\Pi$	3.77	$1\sigma^22\sigma^21\pi^41\delta^22\pi^1$	−142.620987	0.002267	1.974	1.703

[a] State suffers from spin contamination.

exothermicities are shown in Fig. 3. In the case of Ta, the PST predicted cross sections capture the general energy behavior of the experimental cross section, with $\Delta H = -0.6$ eV yielding the best overall reproduction of the data. This is somewhat lower than the exothermicity of 0.96 ± 0.12 eV obtained from the CID measurements, however, an exothermicity this large does not agree with these data as well, as shown by the upper dashed curve in Fig. 3a. In the case of W, excellent agreement is observed between the experimental and the PST predicted cross sections, with $\Delta H = -0.4$ eV providing the best match. This is in agreement with the exothermicity of 0.38 ± 0.09 eV determined from the CID measurements. The additional curves shown in each part of the figure provide a rough estimate of the uncertainty in the ΔH value that could be obtained from the PST model, i.e., about ±0.2 eV for Ta and ±0.1 eV for W. These comparisons provide substantial confidence in the accuracy of the thermochemistry derived here for the MO_2^+ species.

At still higher energies, the MO_2^+ cross sections decline even more rapidly and now deviate strongly from the PST predictions. This is because dissociation of the MO_2^+ products to form $MO^+ + O$ can begin starting at $D_0(O_2) = 5.115$ eV. A simple model for such dissociations has previously been developed [82] and depends only on the energy onset for dissociation (set to 5.115 eV here) and a parameter p describing the energy dependence analogous to n in Eq. (3). This model for the subsequent dissociation probability ($p = 2$ for both metals) is multiplied by the best PST cross sections and shown in Fig. 3. It can be seen that the energy dependence of the data at high energy is reproduced nicely in both cases, although dissociation appears to be delayed somewhat. (Indeed, if the onsets are shifted to ~6 eV, the data are reproduced very well.) Such delays can occur if the initial reaction preferentially places energy in translation of the products instead of being distributed statistically.

3.4. Theoretical results: metal oxide cations

The bonding in diatomic transition metal oxides has been discussed by Schröder et al. [29]. The valence orbitals are 1σ (largely O 2s), 2σ (metal–oxygen sigma bonding), 1π (metal–oxygen pi bonding), 1δ (metal 5d nonbonding), 3σ (largely a metal 6s5d hybrid), 2π (metal–oxygen pi antibonding), and 4σ (metal–oxygen sigma antibonding). Configuration interaction between the 1σ and 2σ orbitals could drive the 2σ above the 1π, and the relative order of the 1δ and 3σ nonbonding orbitals is also unclear. For TaO$^+$, we calculate a $^3\Delta$ ($1\sigma^22\sigma^21\pi^43\sigma^11\delta^1$) ground state, Table 3, with the lowest lying excited state being the singlet-coupled version of this state, $^1\Delta$ having the same electron configuration and lying 0.58 eV above the ground state. Additional excited states, $^1\Sigma^+$, $^3\Sigma^-$, and $^1\Sigma^-$, have energies 0.82, 0.86, and 1.07 eV above the ground state, respectively. All five of these states have TaO triple bonds (occupied 2σ and 1π orbitals) with the remaining two electrons occupying the nonbonding 3σ and 1δ orbitals in different ways. Higher-lying excited states, Table 3, involve exciting an electron from the 1π bonding orbital and thus have excitation energies >3.4 eV above the ground state. All low-lying states have bond lengths of 1.66–1.68 Å, whereas the higher lying excited states have longer bonds (1.86–1.88 Å), indicative of a lower bond order. At a similar level of theory, B3LYP/LANL2DZ, Wu et al. [83] also found the TaO$^+$ ground state to be $^3\Delta$ and the $^1\Sigma^+$ excited state to be 0.87 eV higher in energy. It can also be noted that previous calculations have suggested a $^3\Sigma^-$ ground state at the BP86/LANL2DZ [45] level and a $^1\Sigma^+$ ground state at the B3LYP/LANL2DZ level [43].

The ground state of WO$^+$ is calculated to be $^4\Sigma^-$ ($1\sigma^22\sigma^21\pi^43\sigma^11\delta^2$), Table 3. Low-lying excited states include the low-spin coupled $^2\Gamma$, $^2\Sigma^-$, and $^2\Delta$ lying 0.84, 1.15, and 1.47 eV above the ground state, respectively. Both the ground state and low-lying excited states have bond lengths of 1.64–1.65 Å. We also located a $^4\Pi$ state having an excitation energy of 1.97 eV and a bond length of 1.70 Å, consistent with occupation of the antibonding 2π orbital. At a lower level of theory, B3LYP/HW/6-31G(d), Bohme and co-workers [34] found the $^4\Sigma^-$, $^2\Sigma^-$, and $^4\Pi$ states with excitation energies of 0.0, 0.8, and 2.0 eV, respectively, values that agree nicely with those calculated here.

The theoretical BDEs are compared with various experimental values, including the present CID thresholds, in Table 4. B3LYP calculations using the HW+ and SDD basis sets with calculated BDEs of 7.28 and 6.99 eV, respectively, give the best agreement compared to the experimental BDEs of 7.10 ± 0.12 eV [23] and our CID threshold of 7.01 ± 0.12 eV. Values calculated at the CCSD(T) level using any basis set were all higher, >7.48 eV, and values calculated at the BHLYP level are much too low, <6.54 eV. For WO$^+$, our previous WO$^+$ BDE of 6.77 ± 0.07 eV and our CID threshold of 6.72 ± 0.10 eV again agree well with values calculated at the B3LYP level with the HW+ and SDD basis sets. The CCSD(T) values using the Def2 and SDD basis sets also give reasonable agreement, whereas the BHLYP values are again too low.

In all of these comparisons, it should be realized that spin–orbit effects are not included in these theoretical values, i.e., the 0 K experimental BDEs correspond to dissociation to the lowest spin–orbit state of the metal cation, whereas the theoretical num-

Table 4
Theoretical and experimental bond dissociation energies in eV at 0 K.

Bond	Theory					Experiment	
	State	Basis set	B3LYP	BHLYP	CCSD(T)	CID threshold	Literature BDE[a]
TaO^+	$^3\Delta$	HW+	7.28	6.14	7.67	7.01 ± 0.12	7.10 ± 0.12
		Def2	7.61	6.54	7.56		7.18 ± 0.14
		SDD	6.99	5.84	7.48		8.15 ± 0.65
WO^+	$^4\Sigma^-$	HW+	6.92	5.68	6.07	6.72 ± 0.10	6.77 ± 0.07
		Def2	7.11	5.93	6.54		6.68 ± 0.53
		SDD	6.80	5.56	6.51		7.16 ± 0.43
							5.46 ± 0.43
TaO_2^+	$^1A_1$	HW+	5.79	4.77	6.24	6.08 ± 0.12	6.07 ± 1.05
		Def2	5.93	4.97	6.09		6.73 ± 0.80
		SDD	5.70	4.68	6.05		
WO_2^+	$^2A_1$	HW+	5.61	4.39	5.53	5.49 ± 0.09	5.72 ± 1.17
		Def2	5.80	4.66	5.35		4.6[x] ± 0.7
		SDD	5.56	4.34	5.26		

[a] Values from Table 1.

bers correlate with the average of all spin–orbit levels of the ground state of the metal ion, differences of 0.466 and 0.514 eV for Ta^+ and W^+, respectively. Corrections of the theoretical BDEs by subtracting these excitation energies ignores spin–orbit coupling in the metal oxide cations. For TaO, the spin–orbit splitting in the $^2\Delta$ ground state is 0.435 eV [33] and has been calculated to be as much as 0.56 eV for the related TaC^+ molecule [84]. Because the magnitudes of the spin–orbit coupling in the atomic ions and the molecular species are nearly the same (and the latter unknown for the specific product species considered here), no corrections for spin–orbit effects have been made.

3.5. Theoretical results: metal dioxide cations

A description of the bonding in transition metal dioxides has been detailed previously by Kretzschmar et al. [85] and can be qualitatively thought of in the following way, given that the molecule has C_{2v} symmetry along the z axis with the molecule lying in the xz plane. The $1a_1$ orbital is in-plane π-like bonding and is formed from the $5d_{x^2-z^2}$ orbital of the metal and the $2p_z$ of each oxygen atom. There are two sets of doubly occupied, σ-bonding orbitals ($1b_2$ and $2a_1$) resulting from interaction of the $5d_{xz}$ orbital with two $2p_x$ orbitals and the $5d_{y^2-z^2}$ orbital with the $2p_x$ orbitals of each oxygen atom along with some contributions of the metal 6s orbital. The $1a_2$ and $1b_1$ orbitals form a set of doubly occupied out-of-plane π-like orbitals, which involve the $2p_y$ orbitals on oxygen and the $5d_{xy}$ and $5d_{yz}$ orbitals on the metal. The $2b_2$ orbital, which is mostly nonbonding in character, is formed from the $2p_z$ orbitals of oxygen. The $3a_1$ orbital is a σ-like antibonding orbital, which is derived from the $5d_{y^2}$ along with 6s character and the two $2p_x$ orbitals on oxygen. Higher-lying orbitals include $3b_2$, $4a_1$, $2b_1$, and $2a_2$, which are the antibonding versions of the $1b_2$, $1a_1$, $1b_1$, and $1a_2$ bonding orbitals, and $5a_1$, mainly metal 6s.

For TaO_2^+, our B3LYP calculations find a $^1A_1$ ground state, in agreement with previous calculations [43,45,83] with a bond angle of 103.7°, Table 5. The $^1A_1$ ground state has an electron configuration of $(1a_1)^2(1b_2)^2(1b_1)^2(1a_2)^2(2a_1)^2(2b_2)^2$. The bonding in TaO_2^+ for each Ta–O bond involves 5 electrons in a bonding orbital and one electron in a nonbonding orbital to give a bond order of 2.5, which is reasonable given the strong BDE in this system. Excited states of TaO_2^+ include a $^3B_2$ state lying 1.49 eV above the ground state with additional excited states 2.77–6.91 eV above the ground state, Table 5. These states all involve excitations to antibonding orbitals such that their bond lengths are greater than that of the ground state. Several low-lying singlet excited states were located computationally but in all cases they were spin contaminated with an $s(s+1)$ value around 1.00, meaning these states contain extensive triplet character. In all cases, these singlet states had bond lengths, angles, and energies comparable to their triplet counterparts, and their energies varied with bond angle in an identical fashion to the corresponding triplet states.

For WO_2^+, the ground state is $^2A_1$ with a $(1a_1)^2(1b_2)^2(1b_1)^2(1a_2)^2(2a_1)^2(2b_2)^2(3a_1)^1$ configuration and a bond angle of 103.1°, Table 5. The bond order of WO_2^+ is similar to that of TaO_2^+, with the exception that the unpaired electron occupies an orbital with antibonding character making the bond

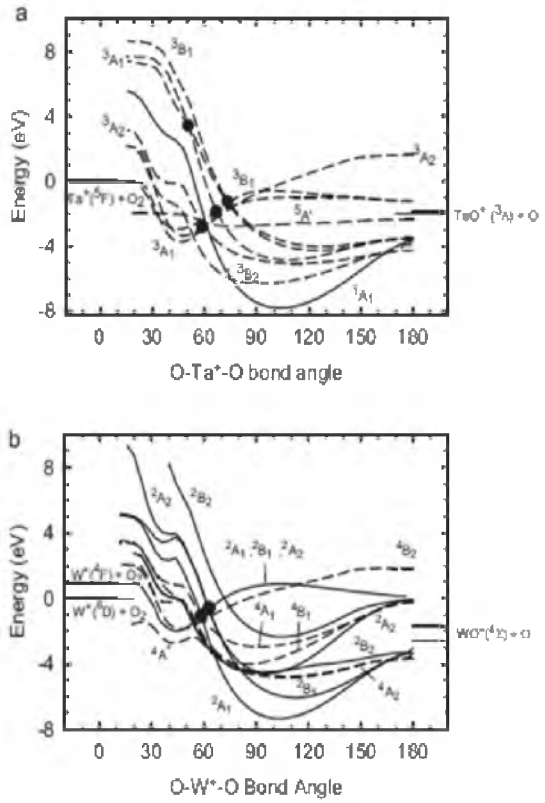

Fig. 4. Relaxed potential energy surface scans of the bond angle for the TaO_2^+ (part a) and WO_2^+ (part b) systems calculated at the B3LYP/HW+/6-311+G(3df) level. Solid and dashed lines represent singlet and triplet/quintet surfaces in part a and doublet and quartet surfaces in part b, respectively. Calculated energies of reactant and product asymptotes are indicated by horizontal bars to the left and right, respectively. Thicker horizontal bars indicate experimental energies of reactants and products. Large circles indicate avoided crossings.

Table 5
Bond lengths (Å), bond angles, and relative energies for MO_2^+ calculated at the B3LYP/HW+/6-311+G(3df) level.

Species	State	Configuration	s(s+1)	r(M–O) (Å)	Angle (°)	E_{rel} (eV)
TaO_2^+	$^1A_1$	$(1a_1)^2(1b_2)^2(1b_1)^2(1a_2)^2(2a_1)^2(2b_2)^2$	0.00	1.700	103.7	0.00
	$^3B_2$	$(1a_1)^2(1b_2)^2(1b_1)^2(1a_2)^2(2a_1)^2(2b_2)^1(3a_1)^1$	2.03	1.753	92.7	1.49
	$^3A_2$	$(1a_1)^2(1b_2)^2(1b_1)^2(1a_2)^2(2a_1)^2(2b_2)^1(2b_1)^1$	2.03	1.775	113.5	2.77
	$^3A_1$	$(1a_1)^2(1b_2)^2(1b_1)^2(1a_2)^2(2a_1)^1(2b_2)^2(3a_1)^1$	2.02	1.743	109.2	2.91
	$^3A_1$	$(1a_1)^2(1b_2)^2(1b_1)^1(1a_2)^2(2a_1)^2(2b_2)^2(2b_1)^1$	2.05	1.811	124.9	3.55
	$^2B_1$	$(1a_1)^2(1b_2)^2(1b_1)^2(1a_2)^2(2a_1)^1(2b_2)^2(2b_1)^1$	2.03	1.790	127.6	3.72
	$^2A_1$	$(1a_1)^2(1b_2)^2(1b_1)^2(1a_2)^2(2a_1)^2(3a_1)^1(4a_1)^1$	2.03	1.866	46.1	4.04
	$^1A_2$	$(1a_1)^2(1b_2)^2(1b_1)^2(1a_2)^2(2a_1)^2(2a_2)^1(3a_1)^1$	2.00	1.867	48.1	4.46
	$^1B_1$	$(1a_1)^2(1b_2)^2(1b_1)^2(1a_2)^2(2a_1)^2(2b_1)^1(3a_1)^1$	2.02	1.877	45.9	4.87
	$^5A'$	$(1a')^2(1a'')^2(2a')^2(3a')^2(4a')^1(2a'')^1(5a')^1(3a'')^1$	6.01	1.715 2.157	75.3	5.06
	$^5A_2$	$(1a_1)^2(1b_2)^2(1b_1)^2(1a_2)^2(2a_1)^1(2b_2)^1(2b_1)^1(3a_1)^1$	6.01	1.894	138.4	5.26
	$^1A_2$	$(1a_1)^2(1b_2)^2(1b_1)^2(1a_2)^2(2a_1)^1(2b_2)^2(2a_2)^1$	2.03	1.779	97.5	5.48
	$^3B_2$	$(1a_1)^2(1b_2)^2(1b_1)^2(1a_2)^2(2a_1)^1(2b_2)^2(3b_2)^1$	2.01	1.831	119.8	6.91
WO_2^+	$^2A_1$	$(1a_1)^2(1b_2)^2(1b_1)^2(1a_2)^2(2a_1)^2(2b_2)^2(3a_1)^1$	0.76	1.676	103.1	0.00
	$^2B_1$	$(1a_1)^2(1b_2)^2(1b_1)^2(1a_2)^2(2a_1)^2(2b_2)^2(2b_1)^1$	0.75	1.692	112.4	1.27
	$^4A_2$	$(1a_1)^2(1b_2)^2(1b_1)^2(1a_2)^2(2a_1)^2(2b_2)^1(3a_1)^1(2b_1)^1$	3.79	1.745	108.7	2.51
	$^2A_2$	$(1a_1)^2(1b_2)^2(1b_1)^2(1a_2)^2(2a_1)^2(2b_2)^2(2a_2)^1$	0.77	1.714	96.7	2.77
	$^2B_2$	$(1a_1)^2(1b_2)^2(1b_1)^2(1a_2)^2(2a_1)^2(2b_2)^1(3a_1)^2$	0.82	1.723	92.8	2.82
	$^4B_1$	$(1a_1)^2(1b_2)^2(1b_1)^2(1a_2)^2(2a_1)^2(2b_2)^1(2a_2)^1(3a_1)^1$	3.80	1.761	84.2	3.31
	$^4A_1$	$(1a_1)^2(1b_2)^2(1b_1)^2(1a_2)^2(2a_1)^2(2b_2)^1(2b_1)^1(2a_2)^1$	3.80	1.789	91.9	4.32
	$^4A''$	$(1a')^2(1a'')^2(2a')^2(2a'')^2(3a')^2(3a'')^1(4a')^1(5a')^1$	4.03	1.907	42.3	4.62
	$(^4B_1)$	$(1a_1)^2(1b_2)^2(1b_1)^2(1a_2)^2(2a_1)^2(3a_1)^1(2b_1)^1(4a_1)^1$				
	$^2B_2$	$(1a_1)^2(1b_2)^2(1b_1)^2(1a_2)^2(2a_1)^2(2b_2)^2(3b_2)^1$	0.76	1.730	104.4	4.97
	$^2B_1$	$(1a_1)^2(1b_2)^2(1b_1)^2(1a_2)^2(2a_1)^2(2b_1)^1(3a_1)^2$	1.75[a]	1.876	44.2	5.13
	$^2A_1$	$(1a_1)^2(1b_2)^2(1b_1)^2(1a_2)^2(2a_1)^2(3a_1)^2(4a_1)^1$	0.76	1.834	46.7	5.23
	$^2A_2$	$(1a_1)^2(1b_2)^2(1b_1)^2(1a_2)^2(2a_1)^2(2a_2)^1(3a_1)^2$	1.69[a]	1.859	47.2	5.37
	$^4B_2$	$(1a_1)^2(1b_2)^2(1b_1)^2(1a_2)^2(2a_1)^2(2b_1)^1(2a_2)^1(3a_1)^1$	3.76	1.876	46.7	5.42
	$^2A_1$	$(1a_1)^2(1b_2)^2(1b_1)^2(1a_2)^2(2a_1)^2(2b_2)^2(3a_1)^1$	1.62[a]	2.132	38.3	9.66
	$^2B_1$	$(1a_1)^2(1b_2)^2(1b_1)^2(1a_2)^2(2a_1)^2(2b_2)^2(2b_1)^1$	1.59[a]	2.199	36.1	10.56
	$^2A_2$	$(1a_1)^2(1b_2)^2(1b_1)^2(1a_2)^2(2a_1)^2(2b_2)^2(2a_2)^1$	0.78	2.104	39.9	11.28

[a] State suffers from spin contamination.

order between 2 and 2.5. This clearly explains the lower observed BDE of WO_2^+ versus TaO_2^+, Table 4. A $^2B_1$ state lying 1.27 eV above the $^2A_1$ ground state was found with other states lying 2.51–11.28 eV higher in energy, Table 5. The lowest excitations involve moving the electron in the $3a_1$ antibonding orbital into other, more antibonding orbitals.

The calculated BDEs of TaO_2^+ compare favorably with the CID threshold of 6.08 ± 0.12 eV, Table 4. Particularly good agreement is found for the CCSD(T) values of 6.05–6.24 eV. The B3LYP values are also in fair agreement although somewhat lower, 5.70–5.93 eV. The BHLYP values are again much too low (by >1 eV). For WO_2^+, the CID threshold value of 5.49 ± 0.09 eV compares well with the B3LYP values, which range from 5.56–5.80 eV, and the CCSD(T) values of 5.26–5.53 eV. At the BHLYP level, the values again are consistently lower than the experimental value (by >0.8 eV). Overall, the agreement between experiment and theory is comparable to that observed for the metal monoxides, lending credence to the accuracy of the thermochemistry obtained here experimentally.

3.6. *Potential energy surfaces for MO_2^+*

Calculated potential energy surfaces for interaction of Ta^+ and W^+ with O_2 ($^3\Sigma^-$) are shown in Fig. 4. In most cases, species have C_{2v} symmetry throughout. Table 5 lists the geometries and energies of various stable states of the MO_2^+ species calculated at the B3LYP/HW+/6-311+G(3df) level of theory.

In the interaction of O_2 ($^3\Sigma_g^-$) with $Ta^+(^5F)$, Fig. 4a, the first step is formation of an association complex intermediate, the lowest of which is $Ta^+(O_2)(^3A_1)$, which has an energy 3.75 eV below the $Ta^+ + O_2$ asymptote. This intermediate has a bond angle of 46.1° and a configuration of $1a_1^2 1b_2^2 1b_1^2 1a_2^2 2a_1^2 3a_1^1 4a_1^1$. There are also $^3A_2$ and $^3B_1$ states of $Ta^+(O_2)$ that lie 0.4 and 0.8 eV higher in energy, respectively, and have similar bond lengths and angles. They differ in their electron configuration by the occupation of the $4a_1$, $2a_2$, or $2b_1$ antibonding orbitals, such that they are nearly degenerate. As the OTaO bond angle gets larger, the potential energy surfaces evolve into the more strongly bound tantalum dioxide cationic species. Here, the ground state of TaO_2^+ is $^1A_1$, which cannot be formed in a spin-allowed process from ground state $Ta^+(^5F) + O_2$ ($^3\Sigma_g^-$) and therefore can only be accessed by a curve crossing with triplet surfaces. The minimum on the $^1A_1$ surface lies 7.83 eV below the $Ta^+ + O_2$ asymptote. Above the $^1A_1$ surface lie the $^3B_2$, $^3A_2$, $^3A_1$, $^3A_1$, and $^3B_1$ surfaces (corresponding to the excited states discussed above) with minima lying 1.49, 2.77, 2.91, 3.55, and 3.72 eV above the $^1A_1$ minimum, respectively. There is also a $^5A'$ state that lies 2.77 eV below the $Ta^+(^5F) + O_2$ ($^3\Sigma_g^-$) asymptote (5.06 eV above the $^1A_1$ GS of TaO_2^+). This state has a minimum around 75°, is relatively flat from 60 to 180°, and correlates to the $TaO^+ + O$ asymptote at small angles because of the C_s symmetry. Importantly, all of the surfaces have minima that lie below the $TaO^+(^3\Delta) + O(^3P)$ product asymptote, 1.96 eV below the $Ta^+ + O_2$ asymptote (1.98 ± 0.12 eV experimentally).

For the activation of O_2 ($^3\Sigma_g^-$) by $W^+(^6D)$, the first step is the formation of an association complex intermediate, $W^+(O_2)$ ($^4A''$, nearly $^4B_1$), which lies 2.69 eV below the $W^+ + O_2$ asymptote. Seven other states of $W^+(O_2)$ were also located and lie 0.51–6.66 eV higher in energy, Table 5. As the bond angle of the $W^+(O_2)$ ($^4A''$) state increases, it crosses a surface having $^4A_2$ symmetry (which is avoided in C_s symmetry) that leads to a minimum 4.54 eV below the $W^+ + O_2$ asymptote. This species is the lowest quartet state of the WO_2^+ dioxide cation. A $^4B_1$ and $^4A_1$ state lie 0.80 and 1.81 eV higher in energy, whereas the $^2A_1$ ground state has an energy of −7.31 eV relative to the $W^+ + O_2$ asymptote. The $^2B_1$, $^2A_2$, and $^2B_2$ excited states discussed above lie 1.27, 2.77, and 2.82 eV above the $^2A_1$ state. The doublet states cannot be formed in spin-allowed processes from ground state $W^+(^6D)$ and O_2 ($^3\Sigma_g^-$) and therefore can only be accessed by a curve crossing with the quartet surfaces. All of the WO_2^+ states lie lower than the $WO^+(^4\Sigma^-) + O(^3P)$ product

asymptote, 1.61 eV below the $W^+ + O_2$ asymptote (1.66 ± 0.07 eV experimentally).

In both metal systems, formation of ground state $MO^+ + O$ products can evolve in spin-allowed pathways from any of the MO_2^+ species, including the ground state. Clearly, these dissociation pathways require breaking C_{2v} symmetry. The observation that the thresholds for formation of MO^+ in the CID of MO_2^+ are consistent with the thermochemistry determined in the literature indicates that there are no barriers in excess of the endothermicity of the reaction, consistent with the qualitative character of the PESs shown in Fig. 4. These surfaces also are consistent with the observation that formation of MO^+ in the reaction of M^+ with O_2 is exothermic and barrierless (as observed experimentally [23]) and can proceed in a spin-allowed fashion by remaining on one of the triplet surfaces evolving from $Ta^+(^5F) + O_2\ (^3\Sigma_g^-)$ or quartet surfaces evolving from $W^+(^6D) + O_2\ (^3\Sigma_g^-)$.

Explicit calculations of MO_3^+ species were not pursued here, but one imagines that the reactions of TaO^+ and WO^+ with O_2 can proceed initially by formation of an associative complex $OTa^+(O_2)$ and $OW^+(O_2)$, with peroxide-like structures. Cleavage of the O_2 bond from such intermediates could lead to formation of $TaO_2^+(^1A_1) + O(^3P)$ and $WO_2^+(^2A_1) + O(^3P)$ products or covalently bound MO_3^+ species could be formed as well. These latter species cannot form double bonds to all oxygens as this formally places the metals in 7+ oxidation states, whereas the maximum oxidation state is 5+ for Ta and 6+ for W. Overall, the reactions $TaO^+(^3\Delta) + O_2(^3\Sigma_g^-) \rightarrow TaO_2(^1A_1) + O(^3P)$ and $WO^+(^4\Sigma^-) + O_2(^3\Sigma_g^-) \rightarrow WO_2(^2A_1) + O(^3P)$ are spin-allowed, consistent with their high efficiency, Fig. 3.

4. Summary

In this study, guided ion beam tandem mass spectrometry is used to generate TaO^+, WO^+, TaO_2^+, and WO_2^+ in a direct current discharge/flow tube (DC/FT) ion source. CID experiments of all four species with Xe are obtained with threshold energies reported in Tables 2 and 4. Reasonable agreement between these CID thresholds and literature thermochemistry is obtained for all systems. The thermochemistry for the metal dioxide cations also agrees that with obtained from the observations that reactions of both metal monoxide cations with O_2 are exothermic. Phase space theory calculations of the energetic behavior for these reactions are also in reasonable agreement with the exothermicities obtained from the CID reactions. Thus, the present results provide thermochemistry for TaO_2^+ and WO_2^+ that is considerably more precise than previous values, Table 1

Detailed quantum mechanical calculations are also performed for the metal monoxide and metal dioxide species. The nature of the bonding in the MO^+ and MO_2^+ species is analyzed at the B3LYP, BHLYP, and CCSD(T) levels of theory. Basis sets used for the metals include HW+, SDD, and Def2TZVPP, and for oxygen 6-311G(3df). Reasonable agreement between theory and the experimental results for the metal oxide and dioxide systems is found for most levels of theory, with BHLYP performing rather poorly. Potential energy surfaces for the interaction of the atomic metal cations with O_2 are also calculated at the B3LYP/HW+/6-311G(3df) level of theory. These surfaces demonstrate that dissociation of the MO_2^+ species can occur from the ground state by loss of an O atom, with no barriers in excess of endothermicity, consistent with the experimental results.

Acknowledgements

This work is supported by the National Science Foundation, CHE-1049580, the Chemical Sciences, Geosciences, and Biosciences Division, Office of Basic Energy Sciences, U.S. Department of Energy, and in part by the National Nuclear Security Administration, Office of Nonproliferation Research and Development (NA-22).

References

[1] D. Smith, N.G. Adams, Plasma Chemistry I, Vol. 89 of Topics in Current Chemistry, Springer-Verlag, Berlin, 1980, p. 1.
[2] E. Murad, J. Geophys. Res 83 (1978) 5525, Tech. Rep. AFGL-TR-77-0235, Air Force Geophysics Laboratory, Hanscom Air Force Base, MA, 1977.
[3] R.A. Sheldon, in: D.H. Barton, A.E. Martell, D.T. Sawyer (Eds.), The Activation of Dioxygen and Homogeneous Catalytic Oxidation, Plenum, New York, 1993, p. 9;
R.A. Sheldon, J.K. Kochi, Metal-Catalyzed Oxidations of Organic Compounds, Academic, New York, 1981.
[4] N. Aristov, P.B. Armentrout, J. Phys. Chem. 90 (1986) 5135.
[5] S.K. Loh, F.R. Fisher, L. Lian, R.H. Schultz, P.B. Armentrout, J. Phys. Chem. 93 (1989) 3159.
[6] S.K. Loh, L. Lian, P.B. Armentrout, J. Chem. Phys. 91 (1989) 6148.
[7] E.R. Fisher, J.L. Elkind, D.E. Clemmer, R. Georgiadis, S.K. Loh, N. Aristov, L.S. Sunderlin, P.B. Armentrout, J. Chem. Phys. 93 (1990) 2676.
[8] D.E. Clemmer, J.L. Elkind, N. Aristov, P.B. Armentrout, J. Chem. Phys. 95 (1991) 3387.
[9] D.E. Clemmer, N.F. Dalleska, P.B. Armentrout, J. Chem. Phys. 95 (1992) 7263.
[10] D.E. Clemmer, N.F. Dalleska, P.B. Armentrout, Chem. Phys. Lett. 190 (1992) 259.
[11] M.R. Sievers, P.B. Armentrout, J. Chem. Phys. 102 (1995) 754.
[12] M.T. Rodgers, B. Walker, P.B. Armentrout, Int. J. Mass Spectrom. 182–183 (1999) 99.
[13] Y.-M. Chen, P.B. Armentrout, J. Chem. Phys. 103 (1995) 618.
[14] M.R. Sievers, Y.-M. Chen, P.B. Armentrout, J. Chem. Phys. 105 (1996) 6322.
[15] M.R. Sievers, P.B. Armentrout, Int. J. Mass. Spectrom. 103 (1998) 179.
[16] M.R. Sievers, P.B. Armentrout, J. Phys. Chem. A 102 (1998) 10754.
[17] M.R. Sievers, P.B. Armentrout, Inorg. Chem. 38 (1999) 397.
[18] M.R. Sievers, P.B. Armentrout, Int. J. Mass Spectrom. 185–187 (1999) 117.
[19] M.E. Weber, J.L. Elkind, P.B. Armentrout, J. Chem. Phys. 84 (1986) 1521.
[20] D.E. Clemmer, M.E. Weber, P.B. Armentrout, J. Chem. Phys. 96 (1992) 10888.
[21] N.F. Dalleska, P.B. Armentrout, Int. J. Mass Spectrom. Ion Process. 134 (1994) 203.
[22] X.-G. Zhang, P.B. Armentrout, J. Phys. Chem. A 107 (2003) 8904.
[23] C.S. Hinton, F.-X. Li, P.B. Armentrout, Int. J. Mass Spectrom. 280 (2009) 226.
[24] F.-X. Li, K. Gorham, P.B. Armentrout, J. Phys. Chem. A 114 (2010) 11043.
[25] X.-G. Zhang, P.B. Armentrout, J. Phys. Chem. A 107 (2003) 8915.
[26] B. Simard, P. Kowalczyk, A.M. James, Phys. Rev. 50 (1994) 846.
[27] J.B. Pedley, E.M. Marshall, J. Phys. Chem. Ref. Data 12 (1983) 967.
[28] J.M. Dyke, A.M. Ellis, M. Feher, A. Morris, A.J. Paul, J.C.H. Stevens, J. Chem. Soc., Faraday Trans. 2 (83) (1987) 1555.
[29] D. Schroder, H. Schwarz, S. Shaik, Struct. Bond 97 (2000) 91.
[30] S.G. Lias, J.E. Bartmess, J.F. Liebman, J.L. Holmes, R.D. Levin, W.G. Mallard, J. Phys. Chem. Ref. Data 17 (Suppl. 1) (1988) 1.
[31] E.G. Rauh, R.J. Ackermann, J. Chem. Phys. 70 (1979) 1004.
[32] R.J. Ackermann, E.G. Rauh, R.J. Thorn, J. Chem. Phys. 65 (1976) 1027.
[33] M.W. Chase, C.A. Davies, J.R. Downey, D.J. Frurip, R.A. McDonald, A.N. Syverud, JANAF thermodynamic tables, J. Phys. Chem. Ref. Data 14 (Suppl. 1) (1985) 1.
[34] V. Blagojevic, G.K. Koyanagi, V.V. Lavrov, G. Orlova, D.K. Bohme, Chem. Phys. Lett. 389 (2004) 303.
[35] M.D. Campbell-Miller, B. Simard, J. Opt. Soc. Am. B 13 (1996) 2115.
[36] G. Demaria, R.P. Burns, J. Drowart, M.G. Inghram, J. Chem. Phys. 32 (1960) 1373.
[37] M.G. Inghram, W.A. Chupka, J. Berkowitz, J. Chem. Phys. 27 (1957) 569.
[38] S. Smoes, J. Drowart, C.E. Myers, J. Chem. Thermodyn. 8 (1976) 225.
[39] A.V. Gusarov, I.S. Gotkis, L.N. Gorokhov, High Temp. 13 (1975) 324.
[40] G. Balducci, G. Gigli, M. Guido, J. Chem. Soc., Faraday Trans. 2 (77) (1981) 1107.
[41] R. Yamdagni, C. Pupp, R.F. Porter, J. Inorg. Nucl. Chem. 32 (1970) 3509.
[42] J. Drowart, G. Exsteen, G. Verhaegen, J. Chem. Soc., Faraday Trans. 60 (1964) 1920.
[43] M. Chen, X. Wang, L. Zhang, M. Yu, Q. Qin, Chem. Phys. 242 (1999) 81.
[44] X. Wang, Z. Gu, Q. Qin, Int. J. Mass Spectrom. 188 (1999) 205.
[45] M. Zhou, L. Andrews, J. Phys. Chem. A 102 (1998) 8251.
[46] S.K. Loh, D.A. Hales, L. Lian, P.B. Armentrout, J. Chem. Phys. 90 (1989) 5466.
[47] R.H. Schultz, P.B. Armentrout, Int. J. Mass Spectrom. Ion Process. 107 (1991) 29.
[48] E. Teloy, D. Gerlich, Chem. Phys. 4 (1974) 417.
[49] D. Gerlich, Adv. Chem. Phys. 82 (1992) 1.
[50] N.R. Daly, Rev. Sci. Instrum. 31 (1960) 264.
[51] K.M. Ervin, P.B. Armentrout, J. Chem. Phys. 83 (1985) 166.
[52] P.J. Chantry, J. Chem. Phys. 55 (1971) 2746.
[53] P.B. Armentrout, in: J.M. Brown, P. Hoffman (Eds.), Topics in Organometallic Chemistry, vol. 4-I, Springer-Verlag, Berlin, 1999, p. 1.
[54] I. Kretzschmar, D. Schröder, H. Schwarz, P.B. Armentrout, Adv. Metal Semicond. Clusters 5 (2001) 347.
[55] X.-G. Zhang, P.B. Armentrout, Organometallics 20 (2001) 4266.
[56] J.D. Burley, K.M. Ervin, P.B. Armentrout, Int. J. Mass Spectrom. Ion Process. 80 (1987) 153.
[57] X.-G. Zhang, R. Liyanage, P.B. Armentrout, J. Am. Chem. Soc. 123 (2001) 5563.
[58] P.B. Armentrout, Int. J. Mass Spectrom. 200 (2000) 219.
[59] W.J. Chesnavich, M.T. Bowers, J. Phys. Chem. 83 (1979) 900.

[60] P.B. Armentrout, Adv. Gas-Phase Ion Chem. 1 (1992) 83.
[61] F. Muntean, P.B. Armentrout, J. Chem. Phys. 115 (2001) 1213.
[62] N. Aristov, P.B. Armentrout, J. Am. Chem. Soc. 108 (1986) 1806.
[63] P.B. Armentrout, in: N.G. Adams, L.M. Babcock (Eds.), Advances in Gas Phase Metal Ion Chemistry, 1, JAI, Greenwich, 1992, p. 83.
[64] A.D. Becke, J. Chem. Phys. 98 (1993) 5648.
[65] C. Lee, W. Yang, R.G. Parr, Phys. Rev. B 37 (1988) 785.
[66] M.J. Frisch, G.W. Trucks, H.B. Schlegel, G.E. Scuseria, M.A. Robb, J.R. Cheeseman, G. Scalmani, V. Barone, B. Mennucci, G.A. Petersson, H. Nakatsuji, M. Caricato, X. Li, H.P. Hratchian, A.F. Izmaylov, J. Bloino, G. Zheng, J.L. Sonnenberg, M. Hada, M. Ehara, K. Toyota, R. Fukuda, J. Hasegawa, M. Ishida, T. Nakajima, Y. Honda, O. Kitao, H. Nakai, T. Vreven, J.A. Montgomery Jr., J.E. Peralta, F. Ogliaro, M. Bearpark, J.J. Heyd, E. Brothers, K.N. Kudin, V.N. Staroverov, R. Kobayashi, J. Normand, K. Raghavachari, A. Rendell, J.C. Burant, S.S. Iyengar, J. Tomasi, M. Cossi, N. Rega, J.M. Millam, M. Klene, J.E. Knox, J.B. Cross, V. Bakken, C. Adamo, J. Jaramillo, R. Gomperts, R.E. Stratmann, O. Yazyev, A.J. Austin, R. Cammi, C. Pomelli, J.W. Ochterski, R.L. Martin, K. Morokuma, V.G. Zakrzewski, G.A. Voth, P. Salvador, J.J. Dannenberg, S. Dapprich, A.D. Daniels, Ö. Farkas, J.B. Foresman, J.V. Ortiz, J. Cioslowski, D.J. Fox, Gaussian 09, Revision A.1, Gaussian, Inc., Wallingford, CT, 2009.
[67] G. Ohanessian, M.J. Brusich, W.A. Goddard III, J. Am. Chem. Soc. 112 (1990) 7179.
[68] P.J. Hay, W.R. Wadt, J. Chem. Phys. 82 (1985) 299.
[69] F. Weigend, R. Ahlrichs, Phys. Chem. Chem. Phys. 7 (2005) 3297.
[70] D. Andrae, U. Haeussermann, M. Dolg, H. Stoll, H. Preuss, Theor. Chem. Acta 77 (1990) 123.
[71] J.B. Foresman, A.E. Frisch, Exploring Chemistry with Electronic Structure Methods, Gaussian, Inc., Pittsburgh, PA, 1996.
[72] K.P. Huber, G. Herzberg, Molecular Spectra and Molecular Structure. IV. Constants of Diatomic Molecules, Van Nostrand Reinhold, New York, 1979.
[73] C.C. Kiess, J. Res. Natl. Bur. Stand. (U.S.) 66A (1962) 111.
[74] J.O. Ekberg, R. Kling, W. Mende, Phys. Scr. 61 (2000) 146.
[75] P.B. Armentrout, B.L. Kickel, in: B.S. Freiser (Ed.), Organometallic Ion Chemistry, Kluwer, Dordrecht, 1996, p. 1.
[76] P.B. Armentrout, J. Simons, J. Am. Chem. Soc. 114 (1992) 8627.
[77] G. Gioumousis, D.P. Stevenson, J. Phys. Chem. 29 (1958) 294.
[78] E.W. Rothe, R.B. Bernstein, J. Chem. Phys. 31 (1959) 1619.
[79] N. Aristov, P.B. Armentrout, J. Phys. Chem. 91 (1987) 6178.
[80] T.M. Miller, B. Bederson, Adv. Atom. Mol. Phys. 13 (1977) 1.
[81] W.J. Chesnavich, M.T. Bowers, J. Chem. Phys. 68 (1978) 901.
[82] M.E. Weber, J.L. Elkind, P.B. Armentrout, J. Chem. Phys. 84 (1986) 1521.
[83] Z.J. Wu, Y. Kawazoe, J. Meng, J. Mol. Struct. Theochem. 764 (2006) 123.
[84] D. Majumdar, K. Balasubramanian, Chem. Phys. Lett. 294 (1998) 273.
[85] J. Kretzschmar, A. Fiedler, J.N. Harvey, D. Schröder, H. Schwarz, J. Phys. Chem. A 101 (1997) 6252.

Supporting Information for "Guided Ion Beam and Theoretical Study of the Reactions of Hf^+ with H_2, D_2, and HD"

by Christopher S. Hinton and P.B. Armentrout*

Table SI. Theoretical energies (in E_h) of various states of Hf^+ calculated at the level shown.

Theory	$^2D(6s^25d^1)$	$^4F(6s^15d^2)$	$^2F(6s^15d^2)$	$^4F(5d^3)$	$^2G(5d^3)$	$\Delta E(eV)^d$	$\Delta E(eV)^e$
B3LYP/HW+[a]	-48.497337	-48.486389	-48.458190	-48.420000	-48.371379	0.298	2.104
B3LYP/SDD[b]	-47.621061	-47.410722	-47.582595	-47.546703	-47.497847	0.281	2.023
B3LYP/Def2TZVPP[c]	-47.630860	-47.618949	-47.591536	-47.552507	-47.504771	0.324	2.132
BHLYP/HW+[a]	-48.413524	-48.403140	-48.374831	-48.336750	-48.286275	0.283	2.089
BHLYP/SDD[b]	-47.514757	-47.505839	-47.477495	-47.442931	-47.391947	0.243	1.954
BHLYP/Def2TZVPP[c]	-47.525128	-47.515184	-47.487555	-47.449808	-47.399840	0.271	2.050
QCISD(T)/HW+[a]	-48.154063	-48.125630	-48.185610	-48.043175	-48.014226	0.774	3.017
QCISD(T)/SDD[b]	-47.278324	-47.246096	-47.272674	-47.162499	-47.118328	0.877	3.152
QCISD(T)/Def2TZVPP[c]	-47.392133	-47.373462	-47.356675	-47.300635	-47.328427	0.508	2.490
CCSD(T)/HW+[a]	-48.153929	-48.125615	-48.209020	-48.043114	-48.013310	0.770	3.015
CCSD(T)/SDD[b]	-47.278279	-47.246038	-47.278969	-47.162402	-47.118283	0.877	3.153
CCSD(T)/Def2TZVPP[c]	-47.392053	-47.373389	-47.356965	-47.30055	-47.329275	0.508	2.490
experiment[f]						0.563	2.434

[a] Calculated using HW+/6-311+G(3p) basis set. [b] Calculated using Def2TZVPP basis set for all atoms. Ground state in bold.

[c] Calculated using SDD/6-311+G(3p) basis set. [d] Excitation energy from the ^2D state to the $^4F(6s^15d^2)$ state in eV.

[e] Excitation energy from the ^2D state to the $^4F(5d^3)$ state in eV. [f] Values from Table I.

Table S2

Electronic states and populations of Hf, Ta, and W cations

Ion	term	configuration	J	energy (eV)	population (1100 K)
Hf^{+a}	^2D	$6s^25d^1$	3/2	0.00	0.963
			5/2	0.378	0.026
	^4F	$6s^15d^2$	3/2	0.452	0.008
			5/2	0.608	0.002
			7/2	0.787	<0.001
			9/2	1.037	<0.001
Ta^{+b}	^5F	$6s^15d^3$	1	0.00	0.648
			2	0.128	0.280
			3	0.328	0.048
			4	0.547	0.006
			5	0.767	<0.001
	^3F	$6s^25d^2$	2	0.394	0.017
			3	0.847	<0.001
			4	1.208	<0.001
	^3P	$6s^25d^2$	0	0.511	0.001
			1	0.661	<0.001
			2	0.701	<0.001
W^{+c}	^6D	$6s^15d^4$	1/2	0.00	0.750
			3/2	0.188	0.206
			5/2	0.393	0.036
			7/2	0.585	0.006
			9/2	0.762	0.001
	^6S	$5d^5$	5/2	0.920	<0.001
	^4F	$6s^15d^4$	3/2	1.080	<0.001
			5/2	1.401	<0.001
			7/2	1.663	<0.001

[a]C. E. Moore, Atomic Energy Levels, Natl. Bur. Stand. (U.S.) Circ. 467. Vol. III (1958); reprinted as Natl. Stand. Ref. Data Ser., Natl. Bur. Stand. (U.S.) 35 (1971). [b]C. C. Kiess, J. Res. Natl. Bur. Stand. (U.S.) 66A (1962) 111. [c]J. O. Ekberg, R. Kling, W. Mende, Phys.Scr.61(2000)146.